

**Acousto-optic modulation of optical reflection properties in
fiber Bragg gratings and the application in fiber lasers**

DISSERTATION

zur Erlangung des akademischen Grades

Doktor-Ingenieur (Dr.-Ing.)

FRIEDRICH-SCHILLER-UNIVERSITÄT JENA



seit 1558

**vorgelegt dem Rat der Physikalisch-Astronomischen Fakultät
der Friedrich-Schiller-Universität Jena**

von M.Sc. Ricardo Ezequiel da Silva

geboren am 30.05.1981 in Francisco Beltrão (Brasil)

Gutachter

1. Prof. Dr. Hartmut Bartelt, Friedrich-Schiller-Universität - Jena
2. Prof. Dr. Alexandre A.P. Pohl, Federal University of Technology – Parana, Brazil
3. Prof. Dr. Stefan Nolte, Friedrich-Schiller-Universität - Jena
4. Prof. Dr. David Webb, Aston University – Aston, United Kingdom

Tag der Disputation: 10.12.2015

Die vorliegende Arbeit wurde im Rahmen eines bi-nationalen Cotutelle Abkommens
zwischen der Friedrich Schiller Universität Jena und Federal University of
Technology – Parana erstellt.

This thesis is prepared in the framework of a bi-national Cotutelle agreement
between the Friedrich Schiller Universität Jena and the Federal University of
Technology - Parana

ZUSAMMENFASSUNG

Ziel dieser Arbeit ist es, die Wechselwirkung von Schallwellen und Faser-Bragg-Gittern (FBG) in Standard- und mikrostrukturierten Fasern (sog. „suspended core fiber“ (SCF)) zu untersuchen, um dadurch die Reflexionseigenschaften der Faser-Bragg-Gitter zu modulieren und den Modulationswirkungsgrad zu erhöhen. Zunächst werden dazu die akustischen Resonanzmoden und das Frequenzverhalten eines niederfrequenten akustooptischen Modulators ($f < 1.2$ MHz) numerisch unter Verwendung der Finite-Elemente-Methode untersucht. Daraus wird die Wechselwirkung von akustischen Längswellen und Faser-Bragg-Gittern in mikrostrukturierten optischen Fasern abgeleitet. Unter Verwendung der Finite-Elemente-Methode und der Transfermatrixmethode werden in Abhängigkeit von verschiedenen Fasergeometrieparametern die Reflexionseigenschaften simuliert. Die Untersuchungen zeigen, dass zunehmende Luftanteile in mikrostrukturierten optischen Fasern wegen des damit verringerten Siliciumdioxid-Anteils im Faserquerschnitt eine wesentlich verstärkte akustooptische Wechselwirkung im Kern ermöglichen. Die erheblich vergrößerte Modulation der Reflektivität von Faser-Bragg-Gittern kann experimentell in zwei unterschiedlichen mikrostrukturierten optischen Fasern nachgewiesen werden. Außerdem wird ein Verfahren vorgestellt, um eine dynamische Phasenverschiebung in einem gechirpten Faser-Bragg-Gitter unter Verwendung einer optimierten Gestaltung des akustischen Modulators zu induzieren. Anschließend wird als Anwendungsbeispiel die Nutzung der akustooptischen Modulation der Reflexion eines Faser-Bragg-Gitters in einer 3-Loch-Faser zur Modenkopplung in einem Ytterbium-Faserlaser zur Pulsgeneration gezeigt. Abgeleitet aus den Erfahrungen des Anwendungsbeispiels werden anschließend zwei weitere verbesserte Anordnungen des Modulator designs vorgestellt, mit denen die akustooptische Wechselwirkung verbessert und die Frequenz auf bis zu 10 MHz erhöht werden kann. Eine besonders hohe Modulation der Reflektivität konnte mit einer sich im Durchmesser verjüngenden Faser erreicht werden. Darüber hinaus wurde eine erhöhte Modulations-Bandbreite (320 pm) für einen Modulator basierend auf der Interaktion eines akustisch induzierten radialen Gitters mit langer Periode und einem Faser-Bragg-Gitter in einer Standardfaser erzielt. Zusammenfassend zeigen die Ergebnisse, dass durch eine geeignete Faserstrukturierung und eine angepasste Gestaltung von piezoelektrischen Wandlern die akustooptische Wechselwirkung mit Faser-Bragg-Gittern wesentlich verbessert werden kann. Dies kann auch mit kürzeren Fasergittern und mit kleineren Modulatorelementen erreicht werden, was zu kompakteren Anordnungen und schnelleren Wechselwirkungen führt. Eine erhöhte Frequenz und Bandbreite kann beispielsweise die Pulsdauer bei modengekoppelten Faserlasern reduzieren und ist auch für andere Konzepte der faseroptischen Signalverarbeitung von Vorteil.

ABSTRACT

This thesis aims to investigate the interaction of acoustic waves and fiber Bragg gratings (FBGs) in standard and suspended-core fibers (SCFs), to evaluate the influence of the fiber, grating and modulator design on the increase of the modulation efficiency, bandwidth and frequency. Initially, the frequency response and the resonant acoustic modes of a low frequency acousto-optic modulator ($f < 1.2$ MHz) are numerically investigated by using the finite element method. Later, the interaction of longitudinal acoustic waves and FBGs in SCFs is also numerically investigated. The fiber geometric parameters are varied and the strain and grating properties are simulated by means of the finite element method and the transfer matrix method. The study indicates that the air holes composing the SCF cause a significant reduction of the amount of silica in the fiber cross section increasing acousto-optic interaction in the core. Experimental modulation of the reflectivity of FBGs inscribed in two distinct SCFs indicates evidences of this increased interaction. Besides, a method to acoustically induce a dynamic phase-shift in a chirped FBG employing an optimized design of modulator is shown. Afterwards, a combination of this modulator and a FBG inscribed in a three air holes SCF is applied to mode-lock an ytterbium doped fiber laser. To improve the modulator design for future applications, two other distinct devices are investigated to increase the acousto-optic interaction, bandwidth and frequency ($f > 10$ MHz). A high reflectivity modulation has been achieved for a modulator based on a tapered fiber. Moreover, an increased modulated bandwidth (320 pm) has been obtained for a modulator based on interaction of a radial long period grating (RLPG) and a FBG inscribed in a standard fiber. In summary, the results show a considerable reduction of the grating/fiber length and the modulator size, indicating possibilities for compact and faster acousto-optic fiber devices. Additionally, the increased interaction efficiency, modulated bandwidth and frequency can be useful to shorten the pulse width of future all-fiber mode-locked fiber lasers, as well, to other photonic devices which require the control of the light in optical fibers by electrically tunable acoustic waves.

Contents

1. Introduction	5
2. Fiber Bragg gratings.....	8
2.1 Light guiding in standard optical fibers.....	8
2.2 Modal simulation using the finite element method	12
2.3 Refractive index modulation of the grating.....	14
2.4 Coupled mode theory.....	17
2.5 Transfer matrix method	19
3. Interaction of longitudinal acoustic waves and fiber Bragg gratings	22
3.1 Acousto-optic modulation of distinguished side lobes.....	22
3.2 Acousto-optic modulation of overlapped side lobes	23
4. Low frequency acousto-optic modulators.....	25
4.1 Piezoelectric transducers	26
4.1.1 Numerical modeling	26
4.1.2 PZT resonance response and vibration modes	29
4.2 Characterization of longitudinal acousto-optic resonances	32
4.2.1 Numerical modeling	32
4.2.2 Experiment and discussion	34
5. Acousto-optic modulation of fiber Bragg gratings in suspended-core fibers (SCFs)	37
5.1 Numerical modeling	38
5.1.1 Effect of the core size	39
5.1.2 Effect of the air hole size.....	41
5.2 Reflectivity modulation of a FBG in a four holes SCF	46
5.2.1 Experiment and discussion	46
5.3 Acousto-optic modulation of the FBG group delay in a four holes SCF	48
5.3.1 Experiment and discussion	48
5.4 Reflectivity modulation of a FBG in a high birefringence SCF.....	51
5.4.1 Experiment and discussion	52
6. Notch filter acoustically induced in a chirped fiber Bragg grating.....	56
6.1 Physical principle	57

6.2	Experiment and discussion	58
7.	Acousto-optic modulation of fiber lasers.....	61
7.1	Modulation of a FBG in three holes suspended-core fiber	63
7.2	Acousto-optic mode-locked fiber laser	65
8.	High frequency acousto-optic modulators for future fiber lasers	68
8.1	Interaction of longitudinal acoustic waves and a FBG in a tapered optical fiber	69
8.1.1	Experiment and discussion	69
8.2	Modulation of a FBG by an acoustically induced radial long period grating.....	74
8.2.1	Physical principle	75
8.2.2	Experiment and discussion	76
9.	Conclusion - outlook.....	81

1. Introduction

The first approach of an all-fiber acousto-optic modulator (AOM) is based on the interaction of flexural acoustic waves and optical modes in an optical fiber. The AOM is composed of a piezoelectric transducer (PZT), an acoustic horn and an optical fiber segment [1]. The PZT generates the acoustic waves which are amplified by the horn and propagate along the fiber. The acoustic wave induces a periodic refractive-index perturbation coupling power of the fundamental optical mode to higher-order modes. Such devices work as dynamic long period gratings (LPGs) being usually employed as notch filters, frequency shifters and couplers with high rejection efficiencies and relative fast switching times ($\sim 40 \mu\text{s}$) [1–3]. However, the AOMs in general require long fiber lengths or high powers to achieve the acousto-optic modulation of an optical signal.

In contrast, the acousto-optic modulation of fiber Bragg gratings (FBGs) is suitable to reduce the size, the switching time ($\sim 17 \mu\text{s}$) and power consumed by the acousto-optic devices [4–10]. In particular, the interaction of flexural acoustic waves and FBGs enables the switching of the Bragg wavelength by coupling power of the fundamental mode to higher-order modes at shorter wavelengths [4,5]. However, this modulation in standard fibers is limited to frequencies $f < 10 \text{ MHz}$ because the acoustic wave tends to propagate by the fiber surface with the increasing frequency [11,12]. On the other hand, longitudinal acoustic waves interacting with FBGs compress and extend the grating period inducing lobes on both sides of the Bragg wavelength [6,7]. In general, modulators based on longitudinal waves operate with higher frequencies and velocities compared to the devices employing flexural waves, which is suitable to shorten the pulse width and mode-lock all-fiber lasers at twice the acoustic frequency [13–15].

Fiber lasers provide various advantages over other types of lasers, such as high efficiencies due to long interaction lengths, excellent beam quality in single mode operation and all-fiber configurations. These features find applications in telecommunications, material processing, sensing and medicine [16–19]. In particular, active mode-locking and Q-switching techniques have been commonly employed in fiber lasers to generate very short pulse widths with high repetition rates. However, the bulk components typically employed to generate the pulses, e.g. electro-optic and acousto-optic modulators based on crystals, cause high cavity losses [20,21]. This requires higher pump energy to achieve the laser operation, which consequently reduces

the overall performance of the laser. Moreover, bulk components can also degrade the laser beam quality, which requires fine alignment and good mechanical stability. On the other hand, acousto-optic modulators based on optical fibers have been successfully employed in Q-switched and mode-locked fiber lasers, offering an alternative solution to enable monolithic fiber setups [13–15,22–24].

However, in standard optical fibers, the acoustic power is mostly distributed over the fiber cross section reducing the interaction with the grating in the core with the increasing frequency. Consequently, several approaches of AOMs using combinations of long grating lengths and high modulation index (strong gratings), high acoustic powers, cladding-etched and tapered fibers have been employed to increase the acousto-optic interaction. The reduction of the fiber diameter by means of etching or tapering techniques makes the optical properties susceptible to surface contamination and degrades the fiber mechanical stability. Moreover, the inscription of long gratings is challenging and expensive, since it requires the use of long phase masks or additional equipment to shift the fiber and the phase mask with respect to the beam [25]. The use of long fiber or grating lengths also increases the switching time of AOMs because the acoustic wave takes more time to travel along the fiber, reducing in some cases, the maximum pulse repetition rate in Q-switched fiber lasers [22–24].

The present thesis intends to numerically and experimentally investigate the interaction of longitudinal acoustic waves and fiber Bragg gratings in standard and suspended-core fibers to evaluate how the fiber and the modulator design can be optimized to increase the modulation efficiency, bandwidth and frequency. In addition, the study aims to investigate specific acousto-optic interactions which can reduce the fiber or the grating lengths and, consequently, the size and power consumed by the acousto-optic devices.

Chapter 2 provides the basic theory on FBGs and the numeric methods employed in the simulations presented in this thesis. A brief review of the light guiding mechanism and of the calculation of modal properties in standard step-index optical fibers by using the finite element method (FEM) is also introduced. The properties of FBGs are reviewed by means of the coupled mode theory and the transfer matrix method (TMM), which is employed to simulate the FBG reflectivity in the subsequent chapters. Chapter 3 provides the basic theory on the interaction of longitudinal acoustic waves and FBGs and discusses the influence of the acousto-optic parameters on the modulation efficiency and frequency.

Chapter 4 discusses the numerical and experimental characterization of an acousto-optic modulator excited at frequencies lower than 1.2 MHz. A piezoelectric transducer (PZT), an acoustic horn and an optical fiber segment are modeled using the 3-D FEM. The frequency

response and the acoustic modes of the AOM are investigated. The reflectivity modulation of a 5 cm long FBG is derived by the TMM. Experimental and simulation results are compared to provide information on the design and characterization of acousto-optic devices.

The interaction of longitudinal acoustic waves and FBGs in suspended-core fibers (SCFs) is numerically investigated in Chapter 5. The geometric parameters of two SCFs are varied, and the strain and grating properties are simulated by means of the FEM and TMM methods, respectively. The reflectivity and group delay modulation of a FBG in a four air holes SCF is experimentally investigated. In addition, the coupling between orthogonal modes of a high birefringence SCF induced by acoustic waves is also demonstrated. The experimental results presented in Chapter 5 use a similar approach of the modulator as described in Chapter 4 to compare the modulation efficiency of the SCFs to previous studies employing standard fibers.

Chapter 6 investigates the interaction of acoustic waves and chirped fiber Bragg gratings in a standard fiber. A dynamic notch filter caused by an acoustically induced phase-shift is experimentally investigated. The chapter also introduces an optimized and compact design of AOM, which is used to increase the acousto-optic interaction compared to the devices described in Chapter 4. The studies discussed in Chapters 3 - 6 are based in the $\lambda = 1550$ nm wavelength range and modulation at frequencies lower than 1.2 MHz, which might be suitable for CW and Q-switched fiber lasers and other dynamic filters.

Chapter 7 studies the modulation of a FBG in three air holes SCF and its application to mode-lock an ytterbium-doped fiber laser at the 1060 nm wavelength range. Acousto-optic modulation at frequencies higher than 5 MHz is achieved by an optimized modulator design based on two PZTs. The study also aims to investigate the influence of the reduction of the grating length (1 cm) to shorten the pulse width of fiber lasers at a repetition rate of 10 MHz.

Chapter 8 describes the assembly and characterization of two approaches of acousto-optic modulators being excited at frequencies higher than 10 MHz. The first AOM is based on a combination of a tapered optical fiber and a high reflectivity grating. This combination allows obtaining high modulation efficiencies and frequencies at the $\lambda = 1060$ nm wavelength range. The second approach investigates an output coupler modulator having a design for use in both reflection and transmission. The interaction of an acoustically induced radial long period grating (RLPG) and a FBG is also investigated. The RLPG couples power of the fundamental mode to higher-order modes supported by the FBG. In summary, the results indicate an increased modulation efficiency, bandwidth and frequency compared to previous studies, which is suitable to shorten the pulse width of future fiber lasers at the repetition rates higher than 26 MHz.

2. Fiber Bragg gratings

2.1 Light guiding in standard optical fibers

A step-index optical fiber is a cylindrical dielectric waveguide composed by a central core of refractive index n_{co} embedded in an outer cladding of lower refractive index n_{cl} . The light is guided in the core by means of the total internal reflection mechanism if the incidence angle at the core-cladding boundary is larger than the critical angle $\theta_c = \sin^{-1}(n_{cl}/n_{co})$ and $n_{co} > n_{cl}$.

Fig. 2.1 illustrates a step-index fiber of core radius r_{co} and cladding diameter d_{cl} .

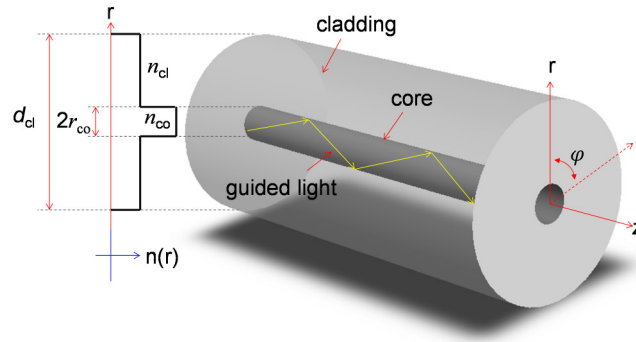


Figure 2.1: Geometrical and refractive index properties of a step-index optical fiber.

The core-cladding refractive indices have a small difference in an step-index fiber given by [26],

$$\Delta = \frac{n_{co}^2 - n_{cl}^2}{2n_{co}^2}. \quad (2.1)$$

In axially symmetric optical fibers, the refractive index changes with the radial distribution r and does not depend on angular variation φ , as illustrated in Fig. 2.1. Thus, $n(r) = n_{co}$ in the core ($r < r_{co}$) and, $n(r) = n_{cl}$, in the cladding to ($r > r_{co}$). The components of the electric and magnetic fields of the propagating light obey the Helmholtz equation,

$$\nabla^2 U + n^2(r)k_0^2 U = 0, \quad (2.2)$$

which is written in cylindrical coordinate as,

$$\frac{\partial^2 U}{\partial r^2} + \frac{1}{r} \frac{\partial U}{\partial r} + \frac{1}{r^2} \frac{\partial^2 U}{\partial \phi^2} + \frac{\partial^2 U}{\partial z^2} + n^2(r) k_0^2 U = 0, \quad (2.3)$$

in which, $U = U(r, \phi, z)$ represents the electric $E_z = E_z(r, \phi) e^{j(\omega t - \beta z)}$ or magnetic $H_z = H_z(r, \phi) e^{j(\omega t - \beta z)}$ fields, ω is the angular frequency and $k_0 = 2\pi / \lambda$ is the wave number in vacuum. The guided modes present a periodic dependence in the angle ϕ with the period 2π , and travel in z direction with the propagation constant β , written as,

$$U(r, \phi, z) = u_r(r) e^{-jl\phi} e^{-j\beta z}, \quad (2.4)$$

in which l is a integer. The inclusion of Eq. (2.4) in Eq. (2.3) leads to a differential equation for the radial distribution profile $u_r(r)$, written as,

$$\frac{\partial^2 u_r}{\partial r^2} + \frac{1}{r} \frac{\partial u_r}{\partial r} + \left(n^2(r) k_0^2 - \beta^2 - \frac{l^2}{r^2} \right) u_r = 0, \quad (2.5)$$

in which,

$$k_T^2 = n_{co}^2 k_0^2 - \beta^2, \quad (2.6)$$

$$\xi^2 = \beta^2 - n_{co}^2 k_0^2, \quad (2.7)$$

k_T , is the transverse propagation constant describing the spatial distribution of the modes in the core, and ξ is the decaying constant describing the modal distribution in the cladding. The light is guided in the core if the propagation constant β is smaller than the wavenumber in the core and larger than the wavenumber in the cladding ($n_{cl} k_0 < \beta < n_{co} k_0$). Considering the fiber is coated by a material of refractive index n_{coat} , the light is guided in the cladding if $n_{coat} k_0 < \beta < n_{cl} k_0$ or is radiated/damped out of the cladding if $\beta < n_{coat} k_0$. The solutions for Eq. (2.5) are described by Bessel functions as,

$$U_z(r) \propto \begin{cases} J_l(k_T r), & r < r_{co} & (core) \\ K_l(\xi r), & r > r_{co} & (cladding) \end{cases} \quad (2.8)$$

in which $J_l(k_T r)$ is the Bessel function of the first kind and order l , which oscillates similarly to the sine or cosine function with a decaying amplitude in the core. $K_l(\xi r)$ is the modified Bessel function of second kind and order l , which decays with increasing ξr .

The transversal and decaying constants are normalized in terms of the core radius r_{co} as,

$$u = k_T r_{co}, \quad (2.9)$$

$$w = \xi r_{co}, \quad (2.10)$$

and can be related via,

$$u^2 + w^2 = V^2, \quad (2.11)$$

in which,

$$V = \frac{2\pi r_{co}}{\lambda} (n_{co}^2 - n_{cl}^2)^{1/2}, \quad (2.12)$$

is the normalized frequency, which is related to the number of fiber modes and their propagation constants. In standard optical fibers, the optical modes are described by special solutions with a distinct propagation constant, field distribution in the transverse plane and two independent polarization states. The modes supported by a conventional step-index cylindrical waveguide consist of $TE(E_z = 0)$, $TM(H_z = 0)$ and hybrid modes $(E_z \neq 0, H_z \neq 0)$. Practical single-mode fibers for optical communication have a refractive index difference Δ less than 1% caused by the addition of a small dopant concentration in the core, such that $n_{cl}/n_{co} \cong 1$. This approximation simplifies the analysis of the optical fiber classifying the modes in groups designated as linearly polarized (LP) modes, which is called weakly guiding approximation since the light confinement into the core is not so tight. The dispersion equations of the $LP_{l,m}$ modes are simplified as [27],

$$\frac{J_m(u)}{uJ_{m-1}(u)} = -\frac{K_m(w)}{uK_{m-1}(w)}, \quad (2.13)$$

in which, the indices l and m describe the azimuthal and radial modal distribution, respectively. For each azimuthal index l , the characteristic equation has multiples solutions being related to the propagations constants $\beta_{l,m}$ of the modes. Therefore, modes with the same

parameters, m and l , have the same effective index and are degenerated. Table 2.1 shows the main groups of conventional LP modes [28].

Table 2.1: LP modes designation and equivalent group modes [28].

LP modes		Group modes
LP $0l$	($m=0$)	HE $1l$
		TE $0l$
LP $1l$	($m=1$)	TM $0l$
		HE $2l$
LP m	($m \geq 2$)	EH $m-1l$
		HE $m+1l$

The effective index $n_{eff} = \beta/k$ of an optical mode is related to the normalized propagation constant, written as,

$$\Upsilon = \frac{(\beta/k)^2 - n_{cl}^2}{n_{co}^2 - n_{cl}^2}. \quad (2.14)$$

Considering Eq. (2.14), Eqs. (2.9) and (2.10) are simplified as $u = V\sqrt{1-\Upsilon}$, $w = V\sqrt{\Upsilon}$, respectively. The zeros in the characteristic Eq. (2.13) satisfying u and w relations correspond to the normalized propagation constants in the dispersion curve, which is solved numerically and illustrated in Fig. 2.2 for $V < 3.5$. Note in Fig. 2.2, that there is no cutoff value for the LP₀₁ fundamental mode. The cutoff V -value of the second-order mode LP₁₁ is $V_C = 2.4048$ determining the single-mode condition.

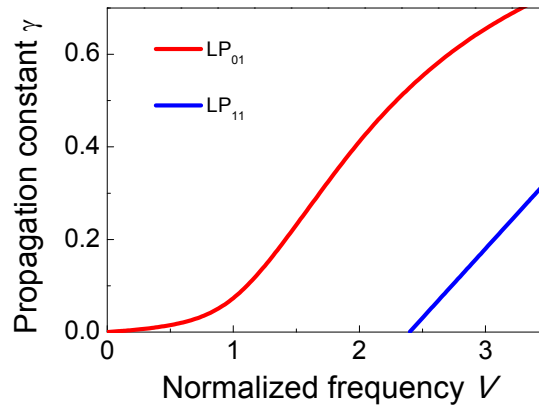


Figure 2.2: Dispersion of LP₀₁ fundamental and LP₁₁ second-order modes in a step-index optical fiber.

2.2 Modal simulation using the finite element method

The finite element method (FEM) is an efficient numerical tool to study and solve complex physical phenomena in the frequency domain or time. The FEM has been widely used in the design and characterization of microstructured optical fibers mainly to determine the optical parameters, such as, the effective index, effective area, chromatic dispersion, confinement loss, modal birefringence and coupled elasto or termo-optical properties [29–34]. The basic equation for the FEM is given by the previous Helmholtz equation Eq. (2.2), here written in terms of the electric field E as,

$$\nabla \times ([\mu_r]^{-1} \nabla \times E) - k_0^2 [\varepsilon_r] E = 0, \quad (2.15)$$

in which, k_0 is the free-space wavenumber and, $[\varepsilon_r]$ and $[\mu_r]$ are the relative dielectric permittivity and relative magnetic permeability tensors, respectively. The division of the fiber cross section (xy plane) into hybrid elements allows obtaining from Eq. (2.15) the eigenvalue equation [35,36],

$$[K]\{E\} = k_0^2 n_{eff}^2 [M]\{E\}, \quad (2.16)$$

in which, the eigenvector $\{E\}$ is the discretized electric field vector, n_{eff} is the effective index and, $[K]$ and $[M]$ are the finite element matrices, which are solved by high performance numeric solvers. The variation of the refractive index caused by the silica chromatic dispersion is calculated by using the Sellmeier equation,

$$n(\lambda) = \sqrt{1 + \sum_{i=1}^3 \frac{m_i \lambda^2}{(\lambda^2 - q_i^2)}} \quad (2.17)$$

in which, m_i and q_i are the silica coefficients listed in Table 2.2 [37].

Table 2.2: Sellmeier coefficients for the silica [37].

$m_1 = 0.6961663$	$q_1 = 0.0684043$
$m_2 = 0.4079426$	$q_2 = 0.1162414$
$m_3 = 0.8974794$	$q_3 = 9.896161$

To evaluate the confinement of leaky modes, a perfectly matched layer (PML) is employed as a boundary condition at the computational window edges. The PML is a fictitious absorption layer which truncates the computational domain avoiding the electromagnetic field to reflect at the window edges. The layer is often used to calculate the propagation constant with the imaginary part, allowing to estimate the confinement loss of the optical modes. Considering an anisotropic PML, the wave equation in Eq. (2.15) is written as [35],

$$\nabla \times ([s_i]^{-1} \nabla \times E) - k_0^2 n^2 [s_i] E = 0, \quad (2.18)$$

in which,

$$[s_i] = \begin{bmatrix} s_y / s_x & 0 & 0 \\ 0 & s_x / s_y & 0 \\ 0 & 0 & s_x s_y \end{bmatrix}. \quad (2.19)$$

The parameters s_x and s_y for an anisotropic rectangular PML are defined in [35], in which, s_x and s_y are complex values written as,

$$s_i = 1 - j\alpha \left(\frac{\Xi}{\Pi} \right), \quad (2.20)$$

in which, α is the maximum value of the attenuation constant, Ξ is the distance between the fiber central axis up to the internal PML interface and Π is the PML thickness. The simulations presented in the next sections are performed using the commercial package COMSOL Multiphysics® 3.5, which is based on the finite element method. The fiber modeling and design consist of three main steps: pre-processing, processing and post-processing, which are subdivided into smaller steps as shows in the diagram of Fig. 2.3. The core-cladding reflective indices are calculated using the Sellmeier equation and attributed to the subdomains.

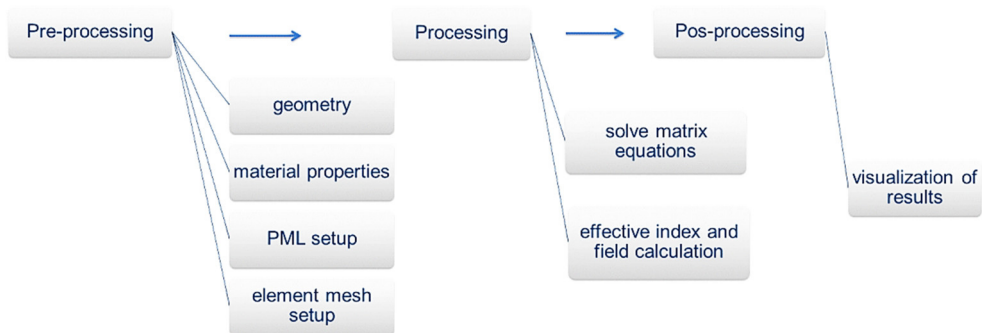


Figure 2.3: Methodology for the simulation of optical modes using the FEM (Comsol).

The FEM divides the physical problem in smaller subdomains (elements), which are often squares or triangles defining a mesh. In the processing step, the software solves the matrix equations and calculates the effective index and the field components.

Fig. 2.4 illustrates the electric field vector (black arrows) and the transversal distribution of the time average power flow in z direction (Poynting vector in W/m^2) for the fundamental mode LP_{01} (HE_{11}) and second-order cladding mode group LP_{11} ($TE_{01}, TM_{01}, HE_{21}$) in a standard optical fiber, considering that the cladding is exposed in the air.

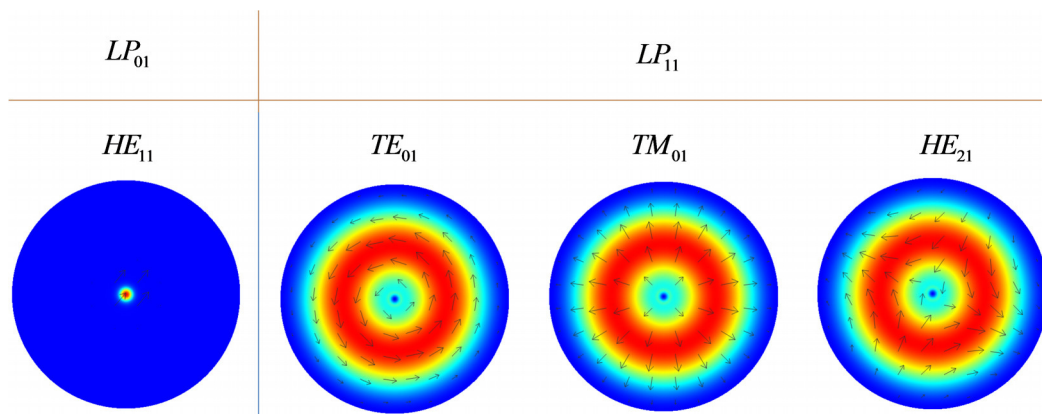


Figure 2.4: Poynting vector for the fundamental mode LP_{01} (HE_{11}) and second-order cladding mode group LP_{11} ($TE_{01}, TM_{01}, HE_{21}$).

2.3 Refractive index modulation of the grating

The refractive index change induced by light in a photosensitive fiber was first demonstrated by Hill *et. al.* in 1978 [38]. In this experiment, an Argon laser at 488 nm was launched into a germanium doped fiber and partially reflected at the opposite fiber end. The resulting standing wave pattern in the core induced a permanent modulation of the refractive index. In 1989, Meltz *et. al.* produced the periodic index change using the transverse holographic method and the single photon absorption at 244 nm ultraviolet (UV). In this method, the light from a coherent source is split into two beams using an amplitude splitting interferometer. The beams are transversally superposed on the fiber to produce an interference pattern in the core, which results in the index modulation. The holographic method enables the grating inscription at distinct wavelengths because the grating period depends on the angle between the two interfering beams [39].

A fiber Bragg grating (FBG) is a periodic modulation of the refractive index along the fiber length being formed by exposing the core to an optical interferometric pattern [25]. The index modulation couples light of a forward-propagating mode to a backward-propagating mode, with propagation constants, β_1 and β_2 , respectively. A FBG is considered as a diffraction grating in which the interaction between the forward and backward modes are described by [40],

$$\beta_1 + \beta_2 = m \frac{2\pi}{\Lambda_B}, \quad (2.21)$$

in which, Λ_B is the grating period and $m = 1$ is the first-order diffraction. A FBG couples modes in reflection and transmission if two conditions are satisfied: (1) phase matching and (2) sufficient modal overlap in the grating. The phase matching condition is written from Eq. (2.21) considering, $\beta = (2\pi / \lambda)n_{eff}$, in terms of the effective index n_{eff} [25],

$$n_{eff1} + n_{eff2} = \frac{\lambda}{\Lambda_B}, \quad (2.22)$$

in which, λ is the optical wavelength. Considering the coupling between two identical optical modes in an uniform grating, $n_{eff1} = n_{eff2} = n_{eff}$, the resonant wavelength at the center reflection band is given by the Bragg condition, written as,

$$\lambda_B = 2n_{eff}\Lambda_B. \quad (2.23)$$

Fig. 2.5 illustrates an uniform Bragg grating, in which the sinusoidal refractive index modulation in the fiber core is merely represented by planes separated by the period Λ_B . An optical mode propagating in the core interacts with each plane. At the Bragg condition, the guided light is reflected in phase between the adjacent planes resulting in a reflected band centered at λ_B . On the other hand, if the condition is not satisfied, the reflected light is out of phase between the planes, causing the incident light to be completely transmitted.

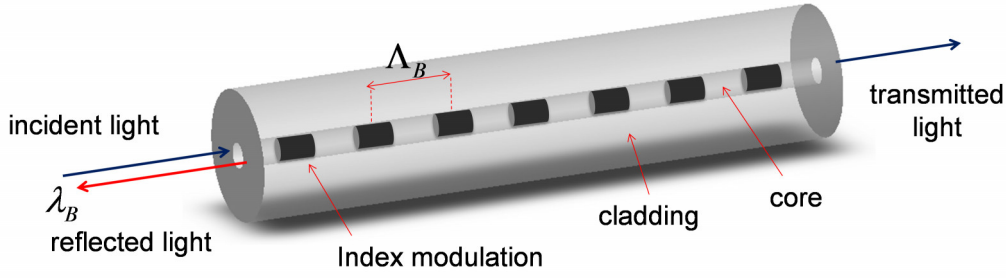


Figure 2.5: Illustration of the index modulation of a uniform Bragg grating into the core of a step-index optical fiber.

Fiber gratings present distinct properties for sensor applications since external parameters, such as, temperature and mechanical deformation can be used to change the grating effective index n_{eff} and/or period Λ_B , and consequently, the Bragg resonance λ_B . According to Eq. (2.23), the Bragg wavelength shift caused by strain and temperature, is written as [41],

$$\Delta\lambda_B = 2 \left[\Lambda_B \frac{\partial n_{eff}}{\partial L} + n_{eff} \frac{\partial \Lambda_B}{\partial L} \right] \Delta L + 2 \left[\Lambda_B \frac{\partial n_{eff}}{\partial T_p} + n_{eff} \frac{\partial \Lambda_B}{\partial T_p} \right] \Delta T_p, \quad (2.24)$$

in which, the first term is related to the strain effect changing the grating period and the mode effective index. The Bragg wavelength shift caused by an isotropic and homogeneous axial strain $S_z = \Delta L / L$ into a grating of length L_g , is given as [42],

$$\Delta\lambda_B = \lambda_B (1 - p_e) S_z, \quad (2.25)$$

in which,

$$p_e = \frac{n_{eff}^2}{2} [p_{12} - \nu(p_{11} + p_{12})], \quad (2.26)$$

is the effective elasto-optic constant, which is related to the strain-optic tensor coefficients p_{11} and p_{12} , and Poisson ratio ν . The second term in Eq. (2.24) is related to the temperature effect on the optical fiber. The Bragg wavelength shift is caused by changes in the grating period caused by the thermal expansion of the fiber and, changes of the refractive index caused by the thermo-optic effect, written as,

$$\Delta\lambda_B = \lambda_B (\vartheta + \zeta) \Delta T_p, \quad (2.27)$$

in which, $\mathcal{G} = (1/\Lambda_B)(\partial\Lambda_B/\partial T_p)$, is the thermal expansion coefficient ($\mathcal{G} \approx 0.55 \times 10^{-6}$ for silica) and, $\zeta = (1/n)(\partial n/\partial T_p)$, is the thermo-optic coefficient ($\zeta \approx 8.6 \times 10^{-6}$ for germanium-doped silica fiber) [43].

Acoustic waves are useful to dynamically change the Bragg wavelength shift in Eq. (2.25) inducing a periodic strain in the fiber. The modulated spectrum in the simulations discussed in the next sections is calculated by means of the transfer matrix method, which is based on solutions of coupled mode equations, as described in the following section.

2.4 Coupled mode theory

The coupled mode theory is a useful tool to describe the properties and spectrum of FBGs. The transverse component of the electric field is written as a superposition of modes in an ideal waveguide without grating modulation [40,44],

$$\vec{E}_t(x, y, z, t) = \sum_j \left[A_j(z) e^{i\beta_j z} + B_j(z) e^{-i\beta_j z} \right] \psi_j^T(x, y) e^{-i\omega t}, \quad (2.28)$$

in which, β_j is the propagation constant of different modes, ω is the angular frequency and, $A_j(z)$ and $B_j(z)$, are the amplitudes of the j th mode traveling in the $+z$ and $-z$ directions, respectively. The variable $\psi_j^T(x, y)$ describes the transverse modal fields in the core or cladding. The periodic index modulation couples energy between the modes causing variation in $A_j(z)$ e $B_j(z)$ field amplitudes, given as,

$$\frac{\partial A_j}{\partial z} = i \sum_k A_k (K_{kj}^T + K_{kj}^z) e^{i(\beta_k - \beta_j)z} + i \sum_k B_k (K_{kj}^T - K_{kj}^z) e^{-i(\beta_k + \beta_j)z}, \quad (2.29)$$

$$\frac{\partial B_j}{\partial z} = -i \sum_k A_k (K_{kj}^T - K_{kj}^z) e^{i(\beta_k + \beta_j)z} - i \sum_k B_k (K_{kj}^T + K_{kj}^z) e^{-i(\beta_k - \beta_j)z}, \quad (2.30)$$

in which, $K_{kj}^T(z)$ and $K_{kj}^z(z)$ are the transverse and longitudinal coupling coefficients between the j and k modes. $K_{kj}^z(z)$ is usually neglected and $K_{kj}^T(z)$ is written as,

$$K_{kj}^T(z) = \frac{\omega}{4} \iint_{-\infty}^{\infty} \Delta\varepsilon(x, y, z) \psi_k^T(x, y) \psi_j^{T*}(x, y) dx dy, \quad (2.31)$$

which is related to the permittivity modulation $\Delta\varepsilon \cong 2n_{co}\Delta\bar{n}_{co}$, considering the induced index modulation $\Delta\bar{n}_{co}(x, y, z)$ is uniformly distributed only in the core cross section with reflective index n_{co} . Consequently, the ‘‘DC’’ coupling coefficient and the ‘‘AC’’ coupling coefficient are defined, respectively as,

$$\sigma_{kj}(z) = \frac{\omega n_{co}}{2} \Delta\bar{n}_{co}(z) \iint_{core} \psi_k^T(x, y) \psi_j^{T*}(x, y) dx dy, \quad (2.32)$$

$$\kappa_{kj}(z) = \frac{\nu}{2} \sigma_{kj}(z). \quad (2.33)$$

Consequently, the transverse coupling coefficient is given as,

$$K_{kj}^T(z) = \sigma_{kj}(z) + 2\kappa_{kj}(z) \cos\left(\frac{2\pi}{\Lambda_B} z + \phi(z)\right). \quad (2.34)$$

Based on this approach, a fiber Bragg grating is described as a periodic modulation in the effective refractive index of the guided mode as,

$$\Delta n_{eff}(z) = \overline{\Delta n_{eff}}(z) \left[1 + \nu \cos\left(\frac{2\pi}{\Lambda_B} z + \phi(z)\right) \right], \quad (2.35)$$

in which, $\overline{\Delta n_{eff}}$ is the ‘‘DC’’ index change averaged over a grating period Λ_B , ν is the fringe visibility of the index modulation and $\phi(z)$ is the grating chirp. As previously discussed, an uniform FBG couples a forward-propagating mode to a backward-propagating mode with electric fields amplitudes $A(z)$ and $B(z)$, respectively. The interaction between incident and reflected modes is described by the solution of the coupled-mode equations, given as [40],

$$\frac{\partial A}{\partial z} = i\hat{\sigma}A(z) + i\kappa B(z), \quad (2.36)$$

$$\frac{\partial B}{\partial z} = -i\hat{\sigma}B(z) - i\kappa^* A(z), \quad (2.37)$$

in which $A = A(z) \exp(i\delta z - \phi/2)$ and $B = B(z) \exp(-i\delta z + \phi/2)$ are the amplitude fields, $\hat{\sigma} = \delta + \sigma$ is the ‘‘DC’’ self-coupling coefficient and κ is the ‘‘AC’’ coupling coefficient, written as

$$\kappa = \nu \frac{\sigma}{2} = \nu \frac{\pi}{\lambda} \overline{\Delta n_{eff}}, \quad (2.38)$$

which is related to the “DC” coupling coefficient,

$$\sigma = \frac{2\pi}{\lambda} \Delta n_{eff}. \quad (2.39)$$

The dependence of the coupling between the incident and reflected mode with the wavelength is measured by a parameter named as detuning, given as,

$$\delta = 2\pi n_{eff} \left(\frac{1}{\lambda} - \frac{1}{\lambda_D} \right), \quad (2.40)$$

in which, $\lambda_D \equiv 2n_{eff}\Lambda_B$ is the “design wavelength” which considers the effective index of the optical mode without changes induced by the grating refractive index modulation in the core.

2.5 Transfer matrix method

The transfer matrix method (TMM) is a numerical method based on solutions of the coupled-mode equations employed to calculate the spectrum of FBGs. A grating of length L_g is divided into m uniform sections of length Δz , and for each section a 2x2 matrix is attributed. The field amplitudes, A_j and B_j , after propagating each j section, are given as [40],

$$\begin{bmatrix} A_j \\ B_j \end{bmatrix} = \mathbf{F}_j^B \begin{bmatrix} A_{j-1} \\ B_{j-1} \end{bmatrix}, \quad (2.41)$$

in which,

$$\mathbf{F}_j^B = \begin{bmatrix} \cosh(\gamma_B \Delta z) - i \frac{\hat{\sigma}}{\gamma_B} \sinh(\gamma_B \Delta z) & -i \frac{\kappa}{\gamma_B} \sinh(\gamma_B \Delta z) \\ i \frac{\kappa}{\gamma_B} \sinh(\gamma_B \Delta z) & \cosh(\gamma_B \Delta z) + i \frac{\hat{\sigma}}{\gamma_B} \sinh(\gamma_B \Delta z) \end{bmatrix}, \quad (2.42)$$

with,

$$\gamma_B = (\kappa^2 - \hat{\sigma}^2)^{1/2}. \quad (2.43)$$

The result is a single 2x2 matrix obtained by the multiplication of m matrixes $\mathbf{F}^B = \mathbf{F}_M^B \cdot \mathbf{F}_{M-j}^B \dots \mathbf{F}_1^B$, represented by the matrix coefficients,

$$\mathbf{F}^B = \begin{bmatrix} \zeta_{11} & \zeta_{12} \\ \zeta_{21} & \zeta_{22} \end{bmatrix}. \quad (2.44)$$

Fig. 2.6 illustrates the interaction between the forward and backward amplitude fields for a segment of a uniform FBG.

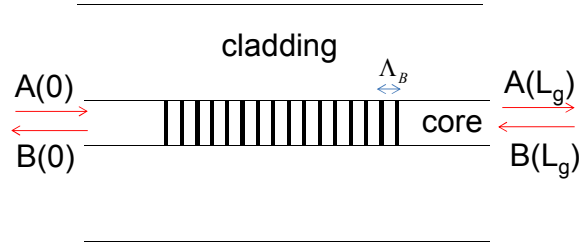


Figure: 2.6: Forward and backward amplitude fields in a segment of a uniform FBG.

Considering the incident amplitude to be $A(0) = 1$ at the grating input, and the reflection to be null $B(L_g) = 0$ at the grating output, the resultant matrix can be written as,

$$\begin{bmatrix} 1 \\ B(0) \end{bmatrix} = \mathbf{F}^B \begin{bmatrix} A(L_g) \\ 0 \end{bmatrix}. \quad (2.45)$$

By solving Eq. (2.45) in terms of the coefficients in Eq. (2.44), the reflected and transmitted amplitudes are given, respectively, as,

$$\mathcal{I}(\lambda) = \frac{A(0)}{B(0)} = \frac{A(0)}{1} = \frac{\zeta_{21}}{\zeta_{11}}, \quad (2.46)$$

$$t(\lambda) = \frac{A(L_g)}{A(0)} = \frac{A(L_g)}{1} = \frac{1}{\zeta_{11}}. \quad (2.47)$$

The reflectivity (ratio between the reflected and incident power) and transmissivity (ratio between the transmitted and incident power) of a uniform FBG are therefore obtained as,

$$\mathfrak{R}(\lambda) = |\mathcal{I}|^2 = \frac{\sinh^2(\sqrt{\kappa^2 - \hat{\sigma}^2} L_g)}{\cosh^2(\sqrt{\kappa^2 - \hat{\sigma}^2} L_g) - \frac{\hat{\sigma}^2}{\kappa^2}}, \quad (2.48)$$

$$\mathfrak{T}(\lambda) = |t|^2 = \frac{\kappa^2 - \hat{\sigma}^2}{\kappa^2 \cosh^2(\sqrt{\kappa^2 - \hat{\sigma}^2} L_g) - \hat{\sigma}^2}. \quad (2.49)$$

The maximum reflectivity is obtained from Eq. (2.48) for $\hat{\sigma} = 0$ as,

$$\mathfrak{R}_{\max}(\lambda_{\max}) = \tanh^2(\kappa L_g), \quad (2.50)$$

in which,

$$\lambda_{\max} = \left(1 + \frac{\overline{\Delta n_{eff}}}{n_{eff}}\right) \lambda_D. \quad (2.51)$$

The maximum reflectivity is described replacing Eq. (2.38) in Eq. (2.50) as a function of the ‘‘AC’’ part of the induced index modulation $\nu \overline{\Delta n_{eff}} = \Delta n_{ac}$, as [39],

$$\mathfrak{R}_{\max}(\lambda_{\max}, L_g) = \tanh^2\left(\frac{\pi \Delta n_{ac} L_g}{\lambda_{\max}}\right). \quad (2.52)$$

The bandwidth of a uniform Bragg grating defines the type of grating according to the index modulation amplitude Δn_{ac} and grating length L_g . A FBG is called ‘‘weak-grating’’ if $\Delta n_{ac} \ll \lambda_D / L_g$. However, the grating is called ‘‘strong’’ if $\Delta n_{ac} \gg \lambda_D / L_g$. In this case, the bandwidth is length independent and proportional to the induced index change. Fig. 2.7 shows an example of the simulated spectrum of a weak (red) and a strong (blue) uniform FBG calculated by the TMM.

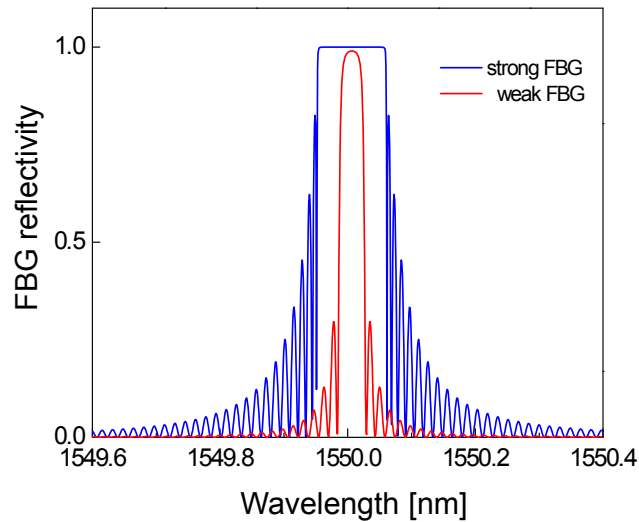


Figure 2.7: Reflectivity of a strong (blue) and a weak (red) uniform Bragg grating.

3. Interaction of longitudinal acoustic waves and fiber Bragg gratings

3.1 Acousto-optic modulation of distinguished side lobes

The interaction of longitudinal acoustic waves and Bragg gratings enables the dynamic change of the reflectivity and the wavelength of reflection bands on both sides of the Bragg resonance, which is useful for the control of tunable reflectors, modulators and fiber lasers [6,7,13,24,45]. Fig. 3.1 illustrates the acousto-optic modulation with longitudinal waves. Fig. 3.1(a) illustrates an optical mode with effective index n_{eff} interacting with a non-perturbed FBG of period Λ , resulting in a reflected band at the Bragg wavelength $\lambda_B = 2n_{\text{eff}}\Lambda$. Fig. 3.1(b) illustrates a longitudinal acoustic wave producing a periodic strain, which compresses and stretches the grating. The strain modulates the mode effective index $n_{\text{eff}}(z)$ and the grating period $\Lambda(z)$, inducing lobes on both sides of the Bragg wavelength. The normalized side lobe reflectivity η is given as [6,7,46],

$$\eta = \tanh^2 \left[\frac{\pi \Delta n_{ac} \Gamma}{\lambda_B} L_g J_m \left(\frac{\lambda_L}{\Lambda} S \right) \right]. \quad (3.1)$$

Here, S is the peak strain, J_m is the Bessel function of the first kind of order m , Δn_{ac} is the grating index modulation amplitude, L_g is the grating length, λ_L is the acoustic period and Γ is the fraction of the optical power into the propagating mode that overlaps with the grating (confinement factor). For a step-index single-mode optical fiber (SMF), the peak strain S is approximated as [7],

$$S = \sqrt{\frac{2P_{ac}}{YA_s v_{ext}}}, \quad (3.2)$$

in which, P_{ac} is the acoustic power, Y is the Young's modulus, A_s is the silica fiber cross section and v_{ext} is the extensional acoustic velocity in silica. Note in Eqs. (3.1) and (3.2) that for a specific value of P_{ac} , the reflectivity η is increased by increasing the index modulation Δn_{ac} or the grating length L_g , as well, by reducing the fiber cross section A_s .

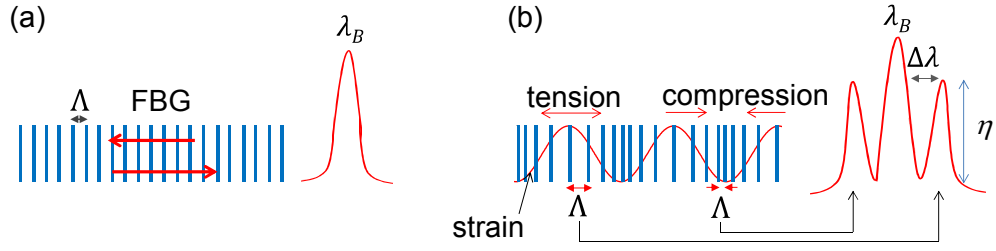


Figure 3.1: Behavior of the fiber Bragg grating (a) without and (b) with longitudinal acousto-optic modulation.

3.2 Acousto-optic modulation of overlapped side lobes

Reflectivity and bandwidth modulation of FBGs is of interest for applications in dispersion compensators, fiber lasers, optical pulse sources and bandpass filters [47–51]. Temperature based techniques have been proposed to induce dynamic chirp in FBGs since they allow the electrical control of the grating properties [48,50]. However, the device response time is also limited because the material heating-cooling process is relatively slow. In addition, the low sensitivity of the silica thermo-optic coefficient requires high temperatures to produce small spectral variations in the nanometer range.

Although the grating excitation with longitudinal waves with distinguished side lobes has been fully described and understood, the excitation of the modulator at lower frequencies, which is clearly marked by the increase of the spectrum bandwidth, has not been discussed in detail so far. Here, it is considered as “low frequencies” the frequency range in which the side lobes are not resolved in the reflection spectrum or the separation $\Delta\lambda$ between the lobes is small enough to make them overlap each other. Fig. 3.2(a) illustrates this acousto-optic modulation. The side lobe separation $\Delta\lambda$ is described as [6],

$$\Delta\lambda = \frac{f\lambda_B^2}{2n_{\text{eff}}v_{\text{ext}}}, \quad (3.3)$$

which is related with the acoustic frequency f , the Bragg wavelength λ_B , the extensional acoustic velocity in silica v_{ext} , and the effective index n_{eff} . For weak gratings, the m order side lobe λ_s has a full width at half maximum (FWHM) bandwidth written as [6],

$$\lambda_{\text{sFWHM}} = \frac{1.39\lambda^2}{\pi L_g n_{\text{eff}}}. \quad (3.4)$$

Note in Eq. (3.3) that the decrease of frequency f reduces the distance between the side lobes, while the reduction of the grating length L_g in Eq. (3.4) increases the side lobe bandwidth. For frequencies in the order of kHz and short gratings, this combined effect makes the side lobes to overlap resulting in a broader overall grating spectrum. Previous works have demonstrated that the Bragg wavelength reflectivity is reduced by increasing the acoustic power or, in other words, the reflected power at λ_B is coupled to higher-order side lobes [24]. As a result, the total grating reflectivity is reduced and the spectrum bandwidth is broader, as illustrated in Fig. 3.2.

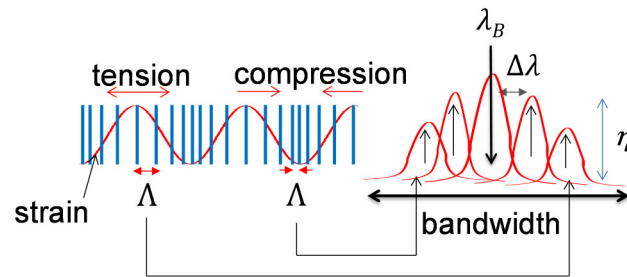


Figure 3.2: Behavior of a fiber Bragg grating with longitudinal acousto-optic modulation indicating the reflectivity and bandwidth modulation caused by the acoustic wave.

The increased bandwidth has been mainly observed for frequencies lower than $f = 600$ kHz which satisfy the conditions above discussed [52–54]. In addition, two other factors are relevant to strengthen the acousto-optic effect. The first is the interaction length between the grating and the acoustic wave. The grating length should support the extension and compression zones induced by the acoustic-wave (e.g. a grating with length of at least the half of the acoustic period). Second, the piezoelectric transducer (PZT), which is used as an acoustic driver, should work at low frequencies in which the side lobes overlap. For this case, the first resonances of PZTs with circular geometry are useful to increase the spectrum bandwidth, since they provide stronger mechanical deformations at lower frequencies to generate the acoustic waves. Consequently, the broader spectra has been noticed in the frequency range $f = 50$ kHz – 250 kHz.

4. Low frequency acousto-optic modulators

An acousto-optic modulator is composed of a piezoelectric transducer (PZT), an acoustic horn and an optical fiber segment. The PZT deformations are amplified and coupled in the fiber by the acoustic horn. Fig. 4.1 illustrates a coaxial acousto-optic modulator, in which the PZT, horn and fiber are connected into an axial configuration [55]. The PZT is commonly fixed to a metal support that also works as a heat sink. This setup is suitable for the excitation of longitudinal acoustic waves and modulation of Bragg gratings [6].

The acousto-optic modulator excites standing acoustic waves by fixing the two fiber ends. In this way, the PZT, horn and fiber, form a resonant acoustic cavity exciting acoustic waves at resonant frequencies. The frequency and amplitude of the acoustic wave depend on the horn-fiber setup [56], as well, of the resonances and the deformation pattern of the vibration modes of the PZT.

In this section, the numerical and experimental characterization of an acousto-optic modulator using an FBG usually employed at frequencies lower than 1.2 MHz is investigated. This device is useful to decrease the reflectivity of the Bragg wavelength and increase the bandwidth by means of acoustically induced overlapped side lobes, as discussed in Sec. 3.2. Such modulators generally employ a relatively large PZT (25 mm in diameter and 2 mm thickness) which makes it easier the connection between the PZT and the acoustic horn, as well, the device assembly. In addition, conventional soldering techniques can also be employed to connect the transducer to the electrodes, since a large part of the PZT surface is generally available. The connection between the PZT-support, PZT-horn and horn-fiber can be made by employing commercial adhesives (e.g. super glue).

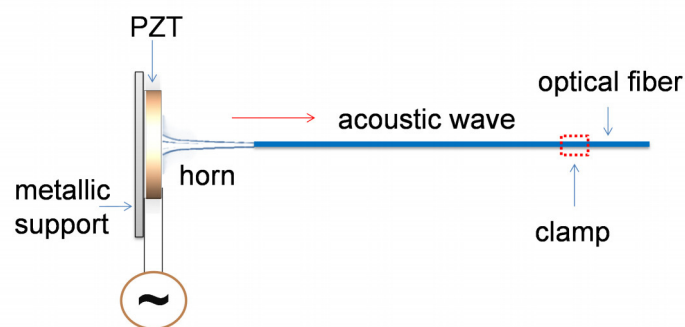


Figure 4.1: Illustration of a coaxial acousto-optic modulator.

4.1 Piezoelectric transducers

The control of modal properties in optical fibers by acoustic waves often requires a piezoelectric transducer (PZT) as an acoustic driver. The analysis of the piezo material and its mechanical deformation is necessary for the operation of acousto-optic devices, because the acoustic wave depends on the vibration modes and frequency of the transducer. However, the PZTs commonly employed in the modulators do not respond to any excitation frequency, but only to narrow bands of resonances in which the vibration modes manifest larger and specific mechanical displacements [57–59]. The excitation of the transducer at non-resonant frequencies implies higher electric power consumption and reduction of the device lifetime. Although the piezo resonances can be measured by impedance-phase methods, the frequency response itself is not sufficient to characterize the mechanical behavior of the acoustic modes, which depend on other parameters, such as, material anisotropy, electric polarization and geometric dimensions. In this section, a PZT is modeled using three-dimensional finite element method (3D-FEM) to investigate the effect of the vibration modes on the excitation of acoustic waves in a fiber segment.

4.1.1 Numerical modeling

Fig. 4.2(a) illustrates a PZT disc. A metallic thin film is deposited on transducer surfaces to compose two polarization electrodes. The transducer is compared to a capacitor because of its high dielectric constant and the electric polarization of the electrodes. Therefore, the PZT can be represented by an equivalent circuit illustrated in Fig. 4.2(b), known as Butterworth-Van Dyke [60,61]. The circuit is composed of a \mathcal{RLC} series and a parallel circuit ($\mathcal{RLC} // C_0$), in which the resistor, \mathcal{R} , the inductor, \mathcal{L} , and the capacitor, C , represent the damping, mass and the elastic constant of the PZT, respectively. C_0 is the electric capacitance between the electrodes. A transducer based on this circuit with angular frequency $\omega = 2\pi f$ is modeled using only electrical parameters. The frequency response of the transducer is obtained solving the \mathcal{RLC} circuit in terms of the impedance Z , written as,

$$Z = \mathcal{R} + j \left(\omega \mathcal{L} - \frac{1}{\omega C} \right). \quad (4.1)$$

The series resonance frequency f_s is obtained from Eq. (4.1) at the condition of irrelevant losses ($\mathcal{R}=0$) and null impedance ($Z=0$),

$$f_s = \frac{1}{2\pi\sqrt{\mathcal{L}C}}. \quad (4.2)$$

A similar interpretation applied to the parallel circuit ($\mathcal{R}\mathcal{L}C//C_o$) in Fig. 4.2(b) allows to obtain the parallel or anti-resonance frequency f_p , written as,

$$f_p = \left(2\pi\sqrt{\mathcal{L}\frac{CC_o}{C+C_o}}\right)^{-1}. \quad (4.3)$$

Fig. 4.2(c) illustrates the PZT frequency response in terms of the impedance magnitude $|Z|$ and phase in degrees. The resonance frequency, f_s , and anti-resonance frequency, f_p , correspond to the condition of minimum and maximum impedance, respectively. At these frequencies, the effect of the inductance \mathcal{L} and the capacitance C cancel each other making the phase null. Since the mechanical deformation is proportional to the electrical current flowing across the piezo, the lowest impedance Z causes a maximum current flow I , inducing a maximum PZT deformation at the resonance f_s .

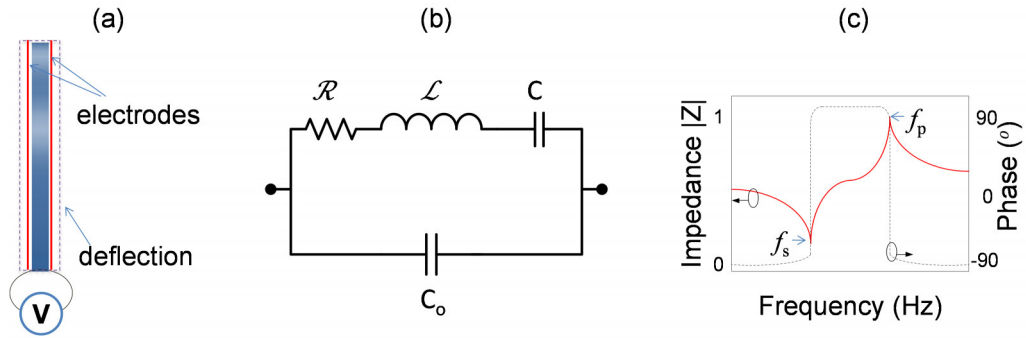


Figure 4.2: (a) PZT lateral illustration, (b) equivalent electric circuit and (c) impedance response.

Piezoelectric transducers excite vibration modes oscillating in each resonance with a particular behavior. The behavior and magnitude of the deformation manifested by the modes depend on the direction of the electric field polarization, dimensions and geometric shape, and material anisotropy. If these materials are subjected to an electric field E , they are mechanically deformed by a stress T or strain S . However, if a mechanical deformation is applied to the material, an electric field E is induced, resulting in an electric displacement D . For PZTs based on piezoceramics, the stress-charge relationship is written as [57],

$$T_p = c_{pq}^E S_q - e_{pi} E_i, \quad (4.4)$$

$$D_i = e_{ip} S_p + \varepsilon_{ij}^S E_j, \quad (4.5)$$

or in matrix form as

$$\begin{bmatrix} T_1 \\ T_2 \\ T_3 \\ T_4 \\ T_5 \\ T_6 \end{bmatrix} = \begin{bmatrix} c_{11} & c_{12} & c_{13} & 0 & 0 & 0 \\ c_{12} & c_{11} & c_{13} & 0 & 0 & 0 \\ c_{13} & c_{13} & c_{33} & 0 & 0 & 0 \\ 0 & 0 & 0 & c_{44} & 0 & 0 \\ 0 & 0 & 0 & 0 & c_{44} & 0 \\ 0 & 0 & 0 & 0 & 0 & c_{66} \end{bmatrix} \begin{bmatrix} S_1 \\ S_2 \\ S_3 \\ S_4 \\ S_5 \\ S_6 \end{bmatrix} - \begin{bmatrix} 0 & 0 & e_{31} \\ 0 & 0 & e_{31} \\ 0 & 0 & e_{33} \\ 0 & e_{15} & 0 \\ e_{15} & 0 & 0 \\ 0 & 0 & 0 \end{bmatrix} \begin{bmatrix} E_1 \\ E_2 \\ E_3 \end{bmatrix}, \quad (4.6)$$

$$\begin{bmatrix} D_1 \\ D_2 \\ D_3 \end{bmatrix} = \begin{bmatrix} 0 & 0 & 0 & 0 & e_{15} & 0 \\ 0 & 0 & 0 & e_{15} & 0 & 0 \\ e_{31} & e_{31} & e_{33} & 0 & 0 & 0 \end{bmatrix} \begin{bmatrix} S_1 \\ S_2 \\ S_3 \\ S_4 \\ S_5 \\ S_6 \end{bmatrix} + \begin{bmatrix} \varepsilon_{11} & 0 & 0 \\ 0 & \varepsilon_{11} & 0 \\ 0 & 0 & \varepsilon_{33} \end{bmatrix} \begin{bmatrix} E_1 \\ E_2 \\ E_3 \end{bmatrix}, \quad (4.7)$$

in which, c_{pq}^E , is the elastic stiffness at constant electric field, e_{pi} and e_{ip} are the piezoelectric stress constants and, ε_{ij}^S , is the dielectric permittivity at constant strain. The indices $i, j = 1, 2, 3$ and $p, q = 1..6$ indicate the directions of the material constants in 3-D xyz planes in Fig. 4.3.

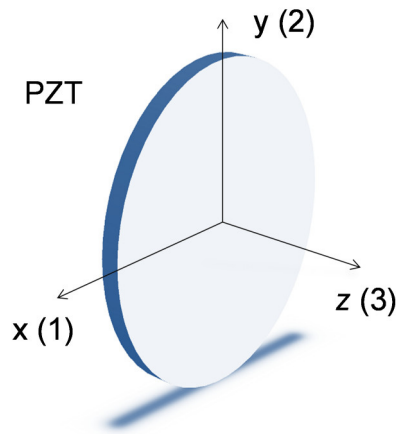


Figure 4.3: PZT disc illustration in 3-D xyz planes indicating the indices $i, j = 1, 2, 3$ and the directions of the material constants.

The constants c_{pq}^E , e_{pi} , e_{ip} and ε_{ij}^S , are defined in terms of two subscripts. The first provides the direction of the electric field associated with the voltage applied to the electrodes. The second provides the stress or strain direction. This approach is based on transversely isotropic materials, in which the elastic properties are invariant with respect to the rotation of any angle about a given axis [62]. For example, an electric field E polarized in direction 3 results in displacements along directions 1 and 2 (e.g. $e_{31} = e_{32}$).

A real PZT disc (2 mm in thickness and 25 mm in diameter) is modeled using the coupled electromechanical relations and material constants included in Eqs. (4.6) and (4.7), which are solved by the commercial 3-D FEM package Comsol Multiphysics v3.5. The PZT has $\sim 10 \mu\text{m}$ thickness silver electrodes deposited on its polarization surfaces. The electrodes are also modeled in the simulations considering isotropic elastic properties such as, density, ρ , Young modulus, Y , and Poisson ratio, ν . The material constants are obtained from the manufacturer (PZ26 model [63]). The PZT is set free of loads and simulated initially alone to calculate the impedance response and the displacements of the natural resonant modes. The disc is excited by a 500 mV harmonic voltage in a frequency range of $f = 1 \text{ kHz} - 1200 \text{ kHz}$, in 0.5 kHz steps, and the corresponding impedance-phase values are calculated for each frequency value. Later, the impedance-phase response of the real PZT is measured using an impedance analyzer to verify the accuracy of the simulation.

4.1.2 PZT resonance response and vibration modes

Figs. 4.4(a) and 4.4(b) show, respectively, the measured and simulated PZT response in terms of the impedance magnitude and phase, as a function of the excitation frequency. The piezo presents vibration modes spaced by series frequencies f_s , obtained by the condition of minimum impedance and null phase. The amplitude difference in the impedance magnitude and phase responses is because the distinct losses for each resonance, since each pair composed by, f_s and f_p , is associated with a specific \mathcal{RLC} circuit. For modes with small damping values, the resonances become sharper and show high amplitudes. Experimental and simulated PZT impedance responses are compared in Fig. 4.4(c). The simulated response shows larger impedance and phase amplitudes compared to experimental values. This is because the material constants considered in the simulations include only real values and do not consider the entire piezoelectric losses of the transducer. However, a good agreement between experiment and simulation is obtained in terms of the resonances, mainly at low

frequencies. The resonances in terms of the simulated PZT displacements (sum of the displacements in xyz directions) are seen in Fig. 4.4(d), indicating the localization of the modes by the maximum displacements.

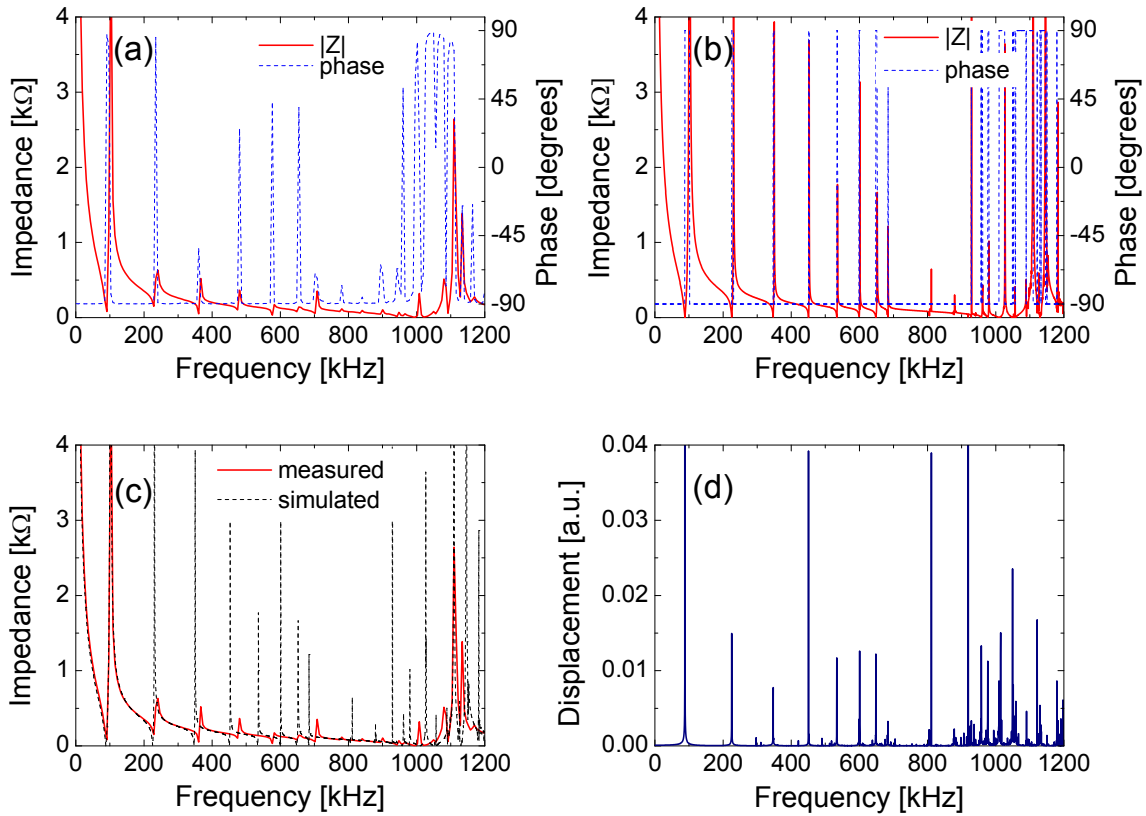


Figure 4.4: PZT impedance response: (a) measured, (b) simulated, (c) measured-simulated and (d) simulated displacement [64].

The displacement behavior of the vibration modes is shown in Fig. 4.5 in yz and xy planes, for the resonances calculated in Fig. 4.4. The displacements are magnified to facilitate the observation of the maximum (red) and minimum (blue) displacements. The PZT analysis of these profiles allows the verification of the longitudinal and radial deformations, respectively. It is observed that all modes have points of longitudinal displacements at their polarization surfaces, which is useful for the excitation of longitudinal waves in the fiber. The deformation of the modes shows that the displacements are not perfectly uniform and axial. The displacement along z is predominant at 958 kHz, 1049 kHz and 1058.5 kHz resonances, in which the maximum deflection is located at the disc center.

Fig. 4.6(a) shows the x and z displacements of the PZT for the frequency range of $f=1$ kHz – 1200 kHz. Note in Fig. 4.6(a), the $f=88$ kHz vibration mode has a higher x displacement (radial deformation) compared to all other modes. In addition, the x and z displacements decrease with the increasing frequency.

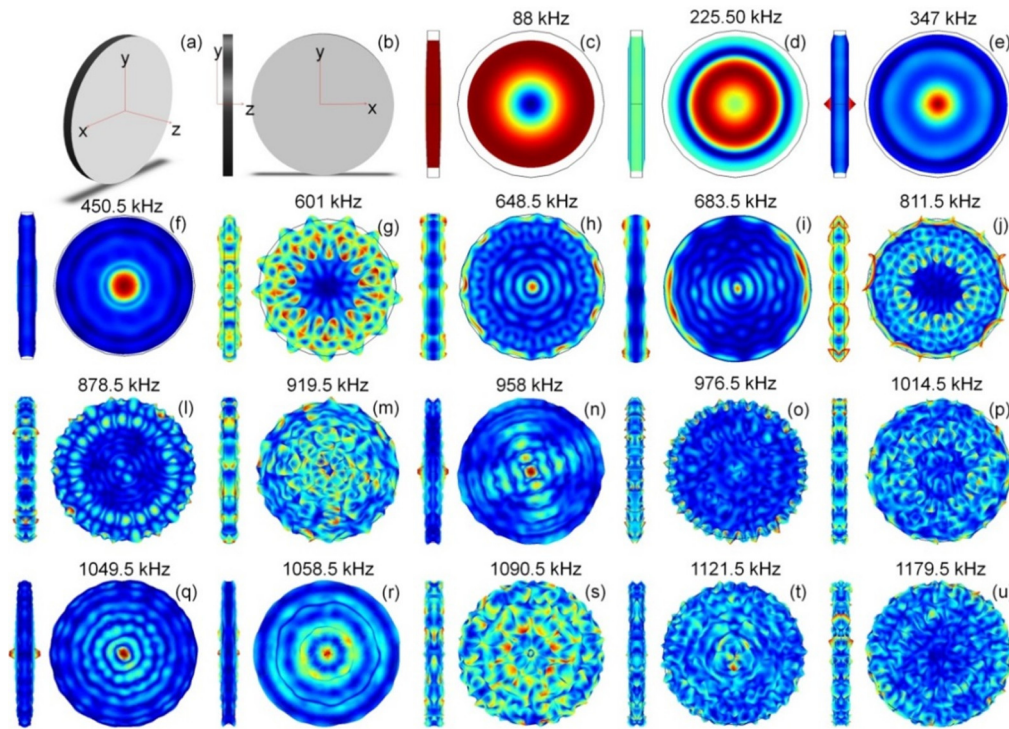


Figure 4.5: Displacement behavior of the piezoelectric transducer vibrations modes in resonances [64].

Fig. 4.6(a) shows the radial (xy plane) and the thickness (yz plane) deformations of the $f=88$ kHz resonant mode indicating the vibration direction with red arrows.

Fig. 4.6(b) shows the x and z displacements for the frequency range of $f=200$ kHz - 1200 kHz and the radial and the thickness deformations of the 1049.5 kHz vibration mode. Although the displacements of the 1049.5 kHz mode are predominant in z direction compared to the $f=88$ kHz mode, the study indicates that modes at lower frequencies can also be useful to excite longitudinal acoustic waves in an optical fiber, since they also show relevant thickness deformations.

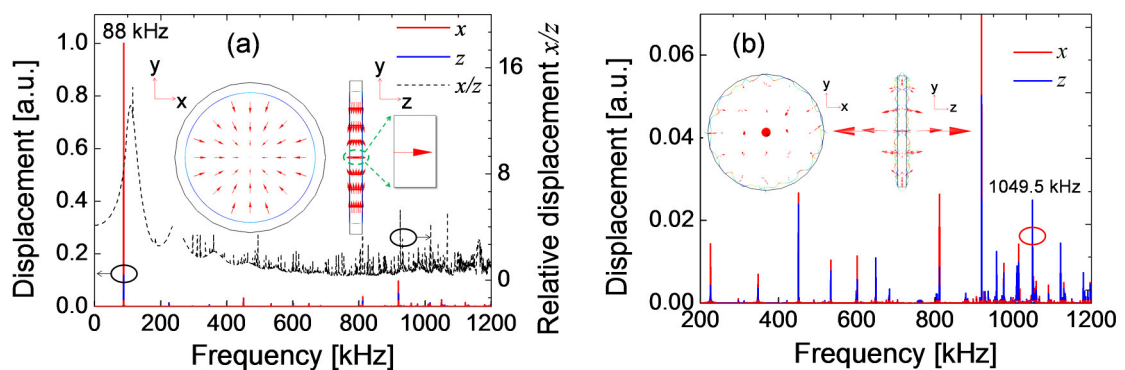


Figure 4.6: Simulated frequency response of the x (radial) and z (longitudinal) displacements of the PZT, indicating the deformation behavior (arrows) of (a) radial and (b) thickness modes [64].

4.2 Characterization of longitudinal acousto-optic resonances

In this section, the analysis of the modulator response and displacement behavior of longitudinal acoustic waves is numerically investigated, and the experimental characterization of the resultant acousto-optic effect in a Bragg grating is assessed. The device is numerically modeled using the transfer matrix method (TMM) and the 3-D finite element method (FEM), as discussed in Sec. 2.5 and Sec. 4.1.1, respectively. The fiber displacements and the modulated FBG spectrum are evaluated. Simulations are compared to experimental measurements of the wavelength shift for the grating under the excitation of resonant acoustic modes. The numerical approach allows the investigation of the electrical, mechanical and grating properties of an acousto-optic device.

4.2.1 Numerical modeling

Fig. 4.7 shows the 3-D design of the acousto-optic modulator which is composed of a PZT disc, a silica horn and a standard single-mode fiber being modeled as a solid rod. Details of the device in the yz , xyz and xy planes are shown in Figs. 4.7(a), 4.7(b) and 4.7(c), respectively. The PZT has silver electrodes deposited on its polarization surfaces, as illustrated in the detail of the Fig. 4.7(a). Further geometrics dimensions are included in Fig. 4.7.

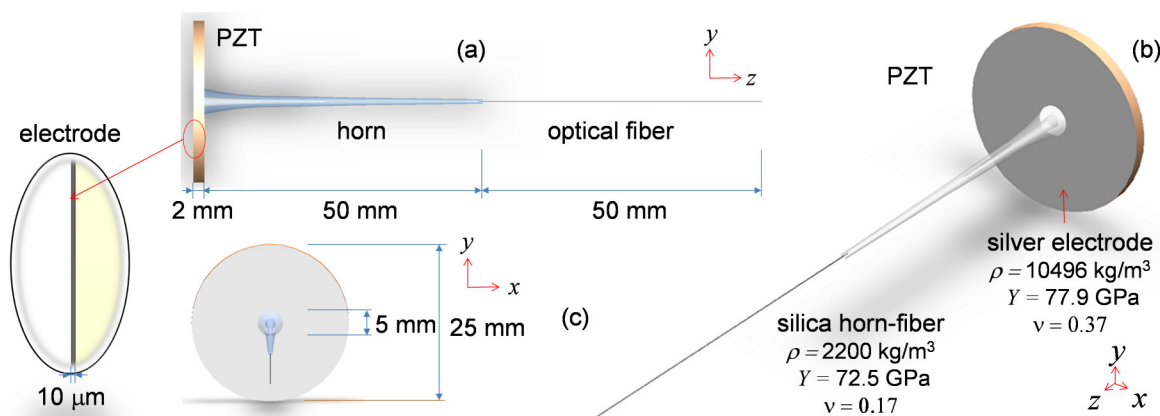


Figure 4.7: Acousto-optic modulator design and geometric properties: (a) yz , (b) xyz and (c) xy views.

Fig. 4.8(a) shows the modulator with details of the real device and the acoustic horn. Fig. 4.8(b) shows the modulator with the finite element mesh that consists of 2 946 205 tetrahedral elements distributed in an approximated regular way, as seen in the detail of Fig. 4.8(c). A detail of the electrode and the fiber are seen in Figs. 4.8(d) and 4.8(e), respectively. The PZT and the fiber end are fixed for the calculation of the acoustic modes supported by the device. The simulations are performed using a computer with 8 x 2.8 GHz Intel® processor cores and 96 GB RAM.

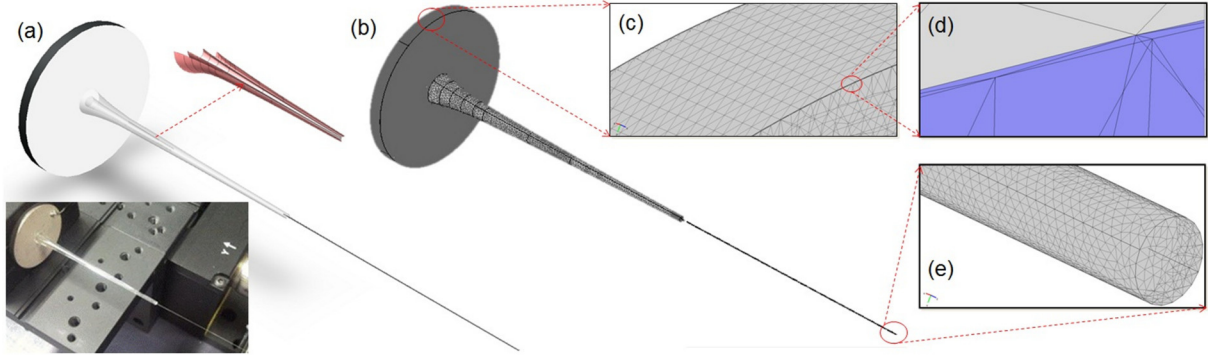


Figure 4.8: (a) acousto-optic modulator design and (b) FEM mesh, with details of the (c) PZT, (d) electrode and (e) optical fiber.

The PZT is modeled using the methodology described in Sec. 4.1.1., which includes the PZT anisotropy to simulate the impedance-response. The PZT is polarized in z direction and excited by a sinusoidal electric field. The resulting longitudinal wave causes a periodic strain $S(z) = S_0 \cos(2\pi fz)$ in the fiber core, in which a uniform Bragg grating is inscribed. The variation of the design wavelength $\lambda_D = 2n_{\text{eff}}\Lambda_B$ caused by the strain $S(z)$ is written as [53],

$$\lambda_D(S(z)) = \lambda_{D0} [1 + (1 - p_e)S(z)], \quad (4.8)$$

in which, λ_{D0} , is the wavelength for the grating at rest, and p_e is the elasto-optic constant. The device is excited with a voltage of 10 V in the $f = 600 \text{ kHz} - 1200 \text{ kHz}$ frequency range, with 1 kHz steps, and the fiber axial (z direction) and the transversal displacements (xy directions) are solved for each frequency. Later, 1000 samples of the acoustically induced strain along the fiber z axis are obtained at the fiber cross section center for the longitudinal resonances (acoustic modes with a larger displacement in z direction). The strain samples are used as an input parameter in Eq. (4.8) for deriving λ_D . With λ_D inserted in Eq. (2.40) the detuning parameter δ can be applied to simulate the modulated spectrum of the FBG by using the TMM, as discussed in Sec. 2.5.

4.2.2 Experiment and discussion

The modulator is assembled considering the components and boundary conditions previously discussed in Sec. 4.2.1. The device includes a 5 cm long grating with a reflectivity of $\sim 99\%$, and with a Bragg wavelength at $\lambda_B \sim 1538.42$ nm. Fig. 4.9 illustrates the experimental setup used for the characterization of the modulated FBG. The FBG is characterized with a broadband source (SLED) and the reflection spectrum is obtained by means of a circulator and an optical spectrum analyzer (OSA) with a 60 pm wavelength resolution. The PZT is excited by a 10 V maximum sinusoidal signal from a signal generator (SG) in the $f = 600$ kHz – 1200 kHz frequency range. By fixing the PZT base and the fiber tip, the modulator works as a resonant acoustic cavity for exciting standing acoustic waves at certain resonant frequencies. The grating spectrum is recorded for the frequencies in which a relevant modulated side lobe is observed.

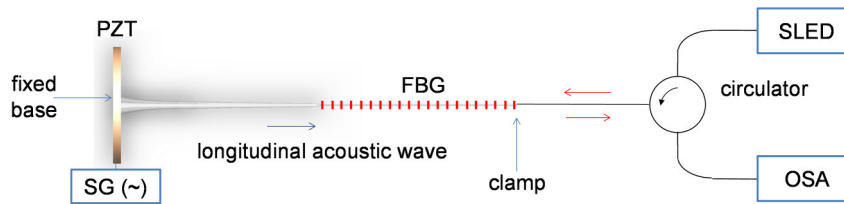


Figure 4.9: Experimental setup used to characterize the FBG acousto-optic interaction.

Fig. 4.10(a) shows the measured-simulated PZT responses in terms of the impedance magnitude and phase as a function of the excitation frequency, as previously discussed in Sec. 4.1.2. (Fig. 4.4) and repeated here for convenience. The PZT response in terms of displacements indicates the localization of the modes by the maximum values in Fig. 4.10(b).

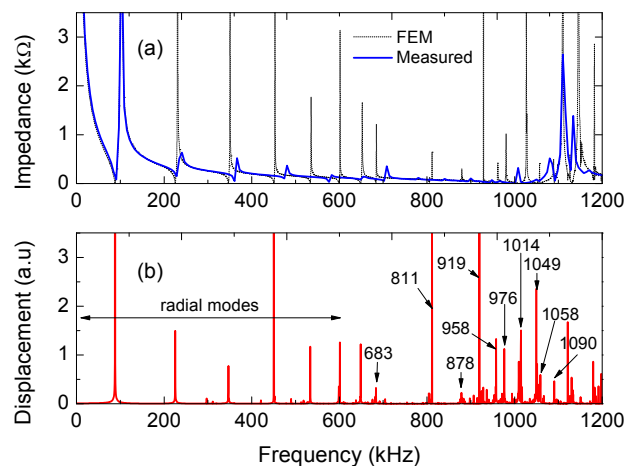


Figure 4.10: (a) Measured-simulated PZT electric frequency response and (b) simulated displacements in resonances.

Some resonances of the relevant longitudinal modes are indicated with arrows in Fig. 4.10(b). In the lower frequency range, the PZT has strong radial modes which are useful to acoustically induce overlapped side lobes, as discussed in Sec. 3.2. However, in this section, only resonances inducing distinguished side lobes are investigated ($f > 600$ kHz).

Fig. 4.11(a) shows the modulator response in terms of fiber displacements (x, y, z), which are decomposed into axial (z direction) and transversal displacements (xy directions). The longitudinal acoustic waves are characterized by a larger displacement along the z direction. The transversal displacements are composed by lower amplitude flexural oscillations polarized in xy plane transversally to the fiber axis. Note that Fig. 4.11(a) shows an increase in the number of resonances compared to PZT resonances in Fig. 4.10. The modulator response shows that the device only works at certain frequencies, which limits the wavelength shift step of the induced side lobe. Fig. 4.11(b) shows the ratio between axial and transversal displacements (z/x and z/y), providing an improved distinction of the longitudinal acoustic resonances. The agreement between some PZT-fiber resonances in Figs 4.10(b) and 4.11(b) indicates the dependence of the fiber deformations originated by the PZT. The variations in displacement amplitude are caused by the distinct vibration modes of the PZT. Such amplitude variations also cause variations of the reflectivity of the modulated side lobe.

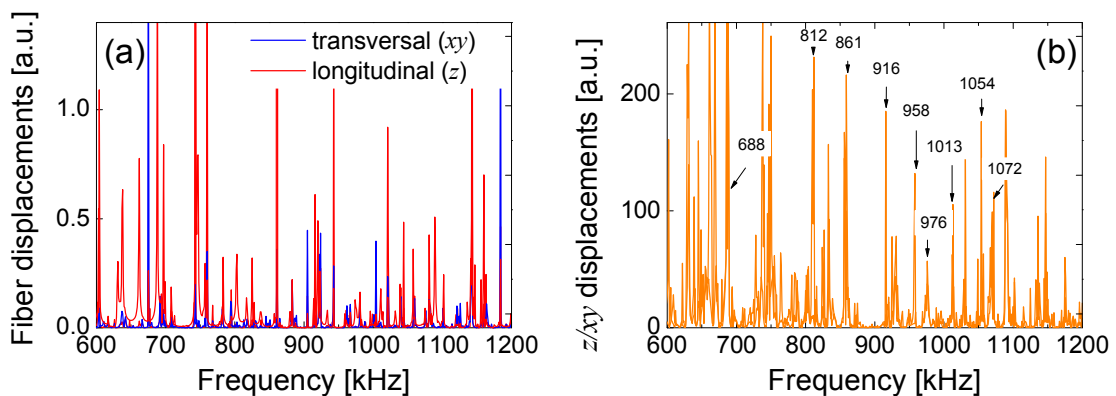


Figure 4.11: (a) Modulator frequency response in terms of the fiber transversal and axial displacements and (b) longitudinal acoustic resonances obtained by the ratio between axial (z direction) and transversal displacements (xy directions) [65].

Fig. 4.12 shows the simulation of the 3-D modulator displacement behavior for the 688 kHz and 1013 kHz longitudinal resonances, respectively. These resonances are excited by the 683 kHz and 1014 kHz modes of the PZT. However, the mode in Fig. 4.12(a) shows a stronger and more uniform axial displacement if compared to the one in Fig. 4.12(d). This is because the resonance in Fig. 4.12(e) is affected by the transversal and backward acoustic

reflections. Figs. 4.12(b) and 4.12(e) show the horn displacement field (red arrow), and Figs. 4.12(c) and 4.12(f) show the strain in the fiber for the considered modes. Fig. 4.12(b) shows that the acoustic wave is strongly coupled and amplified by the horn causing the maximum strain in the fiber (red color) in Fig. 4.12(c). However, Fig. 4.12(e) shows that the acoustic reflections in the horn reduce the strain in the fiber (Fig. 4.12(f)).

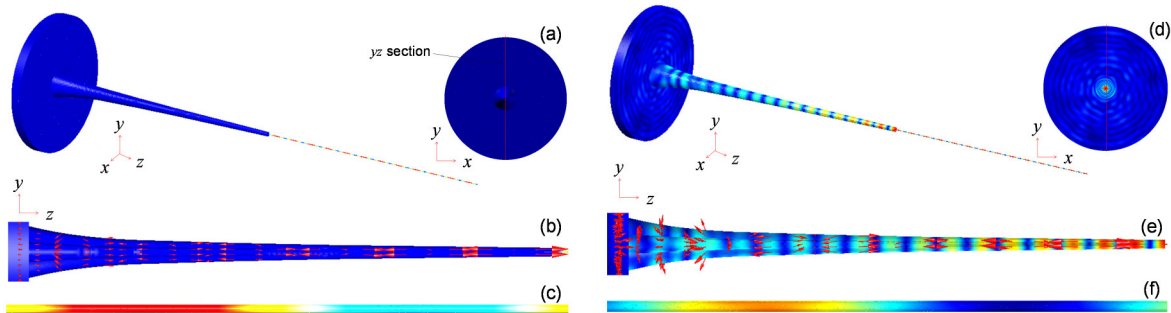


Figure 4.12: Longitudinal acoustic modes. (a) and (d) 3D model and xy horn section representing the displacements at 688 kHz and 1013 kHz, respectively. (b)-(c) yz section of horn displacement and fiber strain at 688 kHz. (e)-(f) yz section of horn displacement and fiber strain at 1013 kHz [65].

Fig. 4.13(a) shows the measured FBG spectrum for the acoustic modulation at 679 kHz and 1019 kHz resonances, respectively. The experimental result is compared to the simulation in Fig. 4.12. The differences in reflectivity and bandwidth between measured-simulated results are caused by grating variations originated the grating inscription process and the OSA resolution that cannot accurately distinguish the side lobes. Note that the measured 679 kHz resonance (which corresponds to the strongest longitudinal mode in Fig. 4.12(a)) has a side lobe reflectivity higher than the 1019 kHz resonance. The measured-simulated side lobe wavelength shift $\Delta\lambda$ is compared to calculated values by using Eq. (3.3) and shown in Fig. 4.13(b). The results show a good agreement between measured-simulated values, indicating the grating modulation takes place only at specific frequencies, which depend on the PZT and horn-fiber resonances.

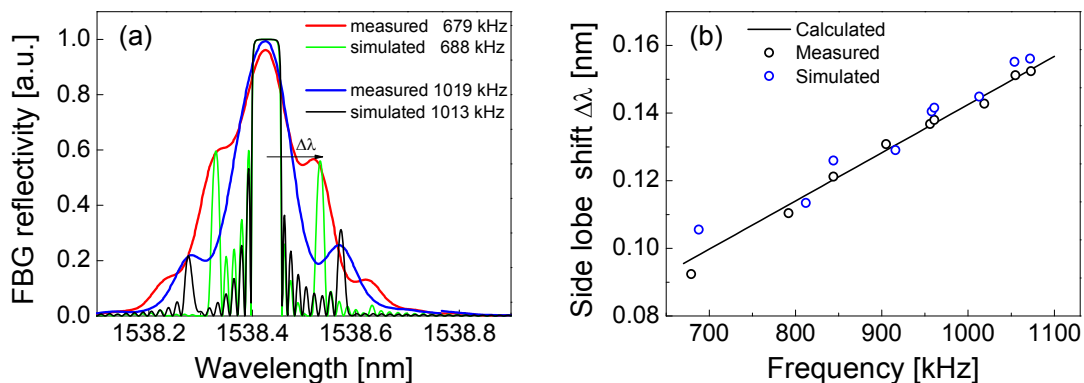


Figure 4.13: (a) FBG measured-simulated spectrum and (b) spectral response in resonances [65].

5. Acousto-optic modulation of fiber Bragg gratings in suspended-core fibers (SCFs)

In a standard single-mode fiber, the acoustic power is evenly distributed over the whole fiber cross section. This reduces the overlap between the acoustic power and the Bragg grating in the core causing the reduction of the side lobe reflectivity η . Cladding-etched fibers with strong gratings or tapered fibers with long gratings enhance the acousto-optic interaction and, hence, the reflectivity η [6,24]. However, the inscription of strong gratings requires higher power densities, germanium dopants or hydrogen loading [46]. In addition, a higher grating modulation index Δn_{ac} can also limit the side lobe operation wavelength, because the FBG bandwidth should be kept smaller than the distance between the main Bragg wavelength and the side lobe to avoid overlap. The inscription of long gratings is limited by the spatial and temporal coherence of interferometry techniques (e.g. Talbot interferometer) or implies the use of long phase masks or additional equipment to shift the fiber or the laser beam [46,66]. Moreover, the experimental realization of tapers is laborious, mainly due to the relatively long fiber transitions required to efficiently increase the acousto-optic interaction. The reduction of the fiber diameter also makes the optical properties more susceptible to surface contamination and affects its mechanical stability [67].

One promising option, besides the above mentioned techniques, is the use of suspended-core fibers (SCFs) [68–72]. These fibers present a very small core in size of a few micrometers suspended by thin radial walls, and surrounded by a single ring of large air holes. This causes a significant reduction of the amount of silica in the cladding, which leads to a larger acousto-optic interaction between the acoustic wave and the grating in the core.

The interaction between longitudinal acoustic waves and fiber Bragg gratings in suspended-core optical fibers is numerically investigated. The fiber core size and the air hole size are varied, and the strain and grating properties are simulated by means of the finite element method and the transfer matrix method, respectively. Changes of the effective index, confinement factor, silica area, strain and wavelength shift induced by the acoustic wave are evaluated, and the resultant side lobe reflectivity is estimated. Experimental results are also shown. A larger reduction of the required acoustic power for achieving the acousto-optic modulation points out to more efficient modulator devices in suspended-core fibers.

5.1 Numerical modeling

The simulations are conducted by means of a 3D finite element method (FEM) and the methodology used to evaluate the strain induced in the core by the longitudinal acoustic wave is described in Sec. 4.2.1. For the simulation of the acoustic wave, Young's modulus $Y = 72.5$ GPa, Poisson ratio $\nu = 0.17$ and the density $\rho = 2200$ kg/m³ for silica are considered [73]. The FEM is also used to simulate the modal properties, such as the effective index n_{eff} of the fundamental mode and the confinement factor Γ . The FBG spectrum is simulated by means of the transfer matrix method (TMM) considering an initial grating of index modulation $\Delta n_{ac} = 10^{-4}$, a reflectivity of $\sim 99\%$ and a Bragg wavelength centered at $\lambda_B = 1550$ nm. The FBG and the fiber length is 25 mm in both cases.

Fig. 5.1 shows a cross section of two SCFs fabricated at IPHT which served as the initial models for the simulations. Fig. 5.1(a) shows a three air holes SCF (SCF3) composed of holes $\phi = 27$ μm in diameter separated by silica bridges of $t = 360$ nm thickness, which form a solid core of $d = 2$ μm incircle diameter. Fig. 5.1(b) shows a four air holes SCF (SCF4) of holes $\phi = 25$ μm in diameter separated by silica bridges of $t = 900$ nm thickness, forming a solid core of $d = 3.3$ μm incircle diameter. A solid SMF with the same outer diameter of $D = 125$ μm , a core diameter of $d = 8.2$ μm and a refractive index contrast of $\Delta n = 0.0036$ is simulated for comparison to evaluate the effect of the SCF geometry on the acousto-optic interaction.

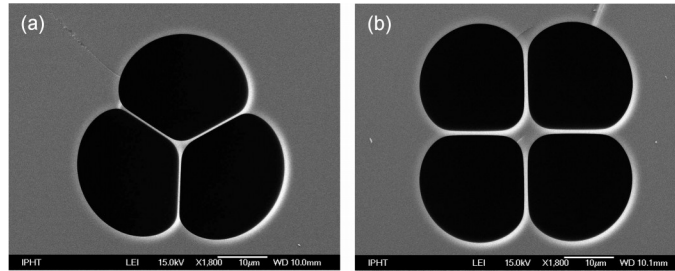


Figure 5.1: Cross section of the suspended-core fibers with (a) three and (b) four air holes used as model for the simulations.

The acoustic excitation is applied upon the area corresponding to the incircle core diameter d directly at the end face of the fibers using a sinusoidal mechanical force with amplitude $F = 1.225 \times 10^{-4}$ N at the frequency $f = 1.091$ MHz. This frequency f is an acoustic resonance of the SMF with a strong longitudinal component. By considering this approach, the acoustic power is efficiently coupled into the SCF. The acoustic power $P_{ac} = 6.05$ mW is estimated for

the SMF considering a side lobe reflectivity $\eta = 50\%$ and the above parameters by means of Eqs. (3.1) and (3.2).

Figs. 5.2(a) and 5.2(b) show a 3D simulation of the displacement distribution for SCF3 and SCF4 samples excited by a longitudinal acoustic wave. The maximum (red color) and minimum (blue color) displacements illustrate the extension and compression regions of the standing acoustic wave, respectively. Although the acoustic wave is coupled into the core only, the mechanical deformations are spread in the cladding, leading to a field amplitude of the acoustic wave that spreads uniformly over the fiber cross section.

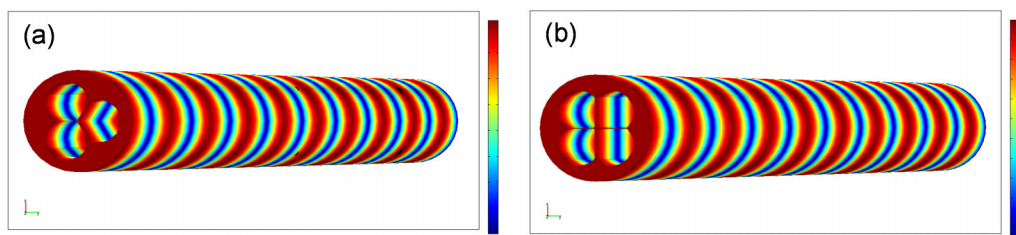


Figure 5.2: Exemplary 3D simulation of the displacement distribution for (a) SCF3 and (b) SCF4 excited in the core by a longitudinal acoustic wave.

5.1.1 Effect of the core size

The incircle core diameter is changed to values of $d = 1.5 \mu\text{m}$, $2 \mu\text{m}$, $3 \mu\text{m}$, $4 \mu\text{m}$, $5 \mu\text{m}$ and $6.6 \mu\text{m}$ to study the effect of the SCF3 core size. For the SCF4 samples, $d = 1.5 \mu\text{m}$, $2 \mu\text{m}$, $3.3 \mu\text{m}$, $4 \mu\text{m}$, $5 \mu\text{m}$ and $6.6 \mu\text{m}$ are employed. Figs. 5.3(a)-(f) and Figs. 5.3(g)-(l) show the fundamental mode intensity distribution over the modeled cross sections of SCF3 and SCF4 considering the core size variation.

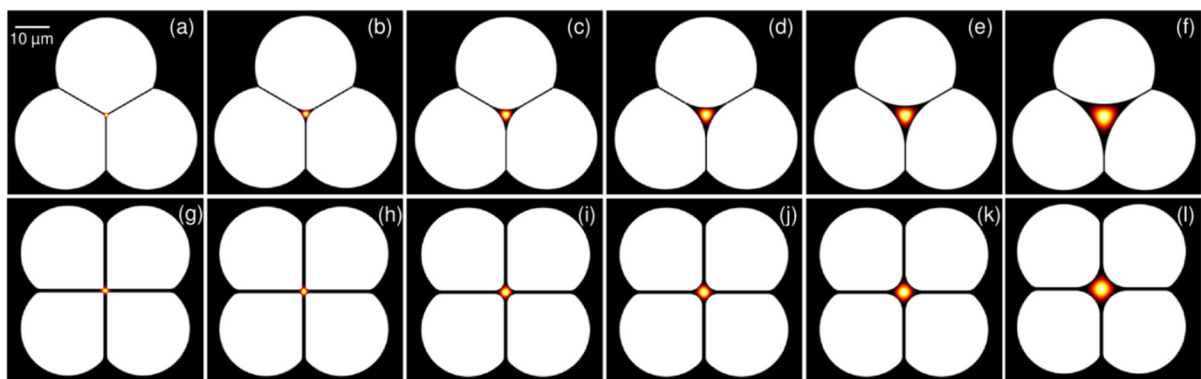


Figure 5.3: SCF cross sections with the fundamental mode intensity distribution of: SCF3 for the incircle core diameter values of (a) $d = 1.5 \mu\text{m}$, (b) $2 \mu\text{m}$, (c) $3 \mu\text{m}$, (d) $4 \mu\text{m}$, (e) $5 \mu\text{m}$, and (f) $6.6 \mu\text{m}$. SCF4 for the incircle core diameter values of (g) $d = 1.5 \mu\text{m}$, (h) $2 \mu\text{m}$, (i) $3.3 \mu\text{m}$, (j) $4 \mu\text{m}$, (l) $5 \mu\text{m}$, and (m) $6.6 \mu\text{m}$ [74].

The smallest d value is chosen to keep a minimum radius of curvature at the core-air boundary. The maximum value is defined considering the saturation of the confinement factor. The air holes and bridges are kept constant in the simulations for both fibers

Figs. 5.4(a) and 5.4(b) compare the modulated FBG spectra of the SMF with the modulated spectra of the smallest and largest SCF3 and SCF4 core sizes, respectively. The relative increase in reflectivity η compared to the SMF varies between $\Delta\eta = 1.4\%$ and 9.4% for the SCF3 and between $\Delta\eta = 11.6\%$ and 18.1% for the SCF4. In addition, the smallest core diameters in both SCFs induce a larger side lobe separation $\Delta\lambda$ than in the SMF case.

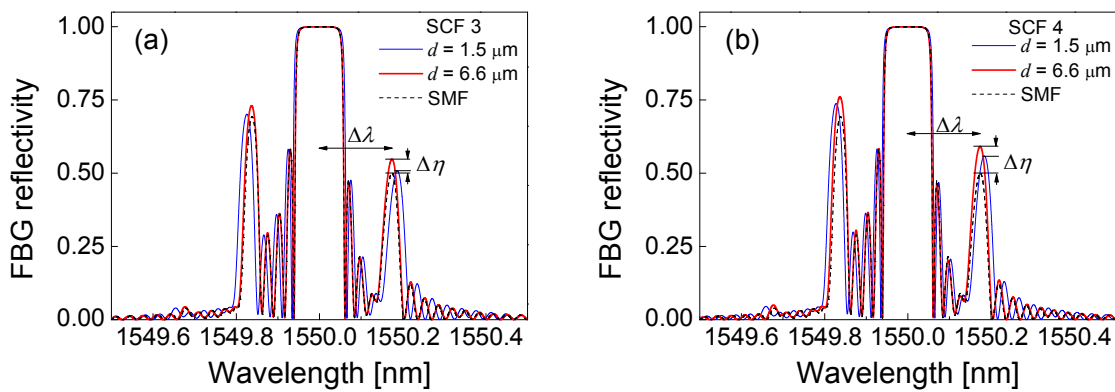


Figure 5.4: (a) Modulated FBG spectra for $d = 1.5 \mu\text{m}$ and $6.6 \mu\text{m}$ SCF 3 samples compared to the SMF. (b) Modulated FBG spectra for $d = 1.5 \mu\text{m}$ and $6.6 \mu\text{m}$ SCF 4 samples compared to the SMF [74].

Fig. 5.5(a) shows the side lobe reflectivity variation for the SCF3 and SCF4 with the increasing core diameter compared to SMF. The reflectivity increase is because of the increased confinement factor Γ , as shown in Fig. 5.5(b). Oppositely, the reduced core diameter induces the optical field to propagate partially in the air holes, reducing the overlap with the FBG in the core, and consequently, the side lobe reflectivity.

However, Figs. 5.5(c) and 5.5(d) show that the strain S_z and the silica area A_s (amount of silica in the fiber cross section) is nearly constant with the increasing core diameter. The strain variation for both SCFs is small compared to the confinement factor effect, which means that the confinement factor is predominant compared to the strain effect for the core size variations in the investigated range.

Fig. 5.5(e) shows the dependence of the side lobe separation $\Delta\lambda$ with the core diameter. The largest shift $\Delta\lambda$ is achieved for the smallest diameter. The increase in $\Delta\lambda$ is because the lower effective index n_{eff} with decreased core diameter, as shown in Fig. 5.5(f). The reduction of n_{eff} is also related to the confinement factor, since the reduced core diameter increases the optical field in the air holes.

Although the silica bridge effect on the strain and optical parameters is not considered in this study, it is expected that variations of the silica bridge thickness induce an effect similar to that of the core variations. An increase in the bridge thickness produces larger silica transition regions around the core increasing the confinement factor.

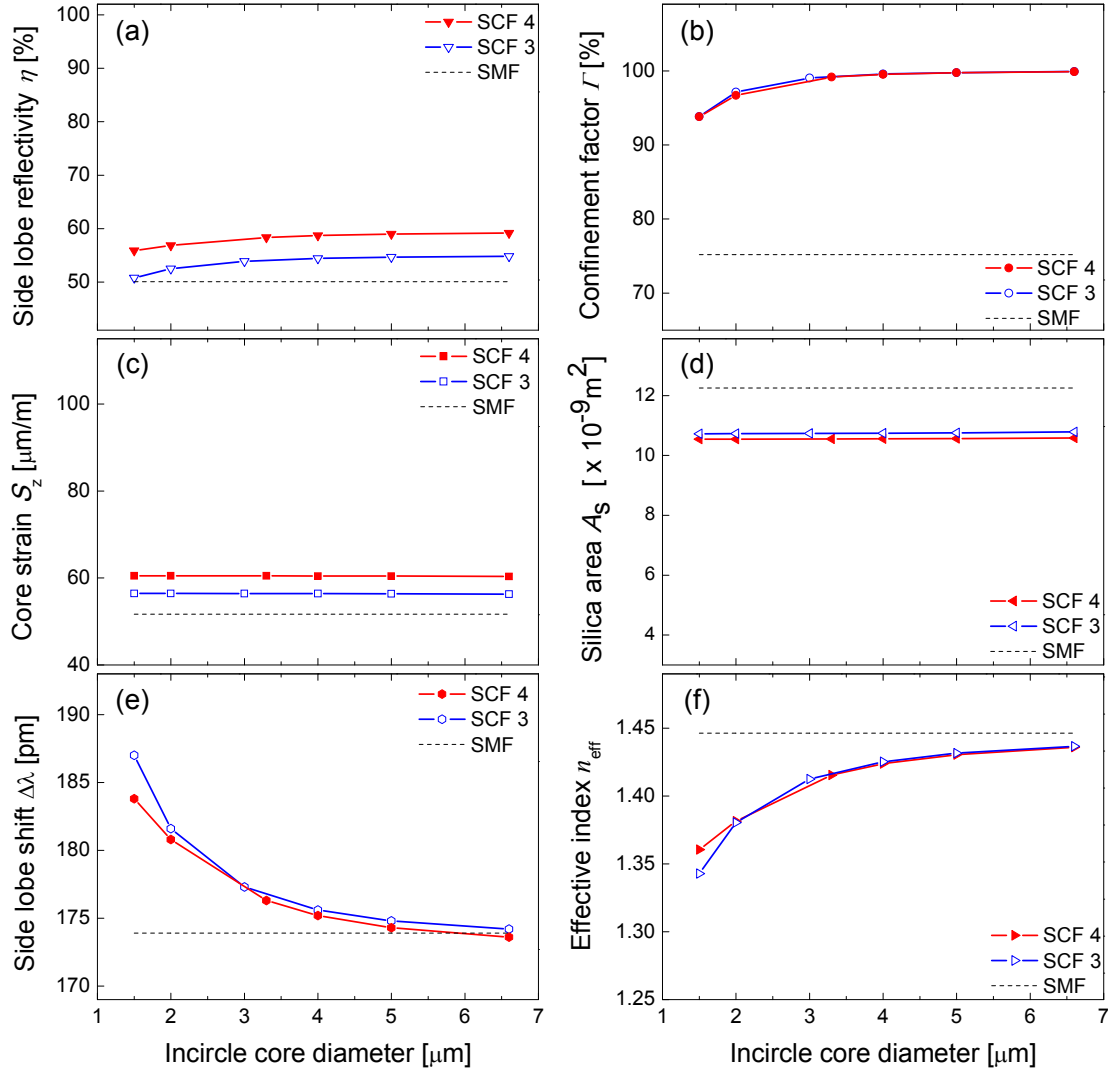


Figure 5.5: (a) Side lobe efficiency η , (b) confinement factor Γ , (c) strain S_z , (d) silica area A_s , (e) side lobe shift $\Delta\lambda$ and (f) effective index n_{eff} variation for the SCF 3 and SCF 4 as a function of core diameter [74].

5.1.2 Effect of the air hole size

The air hole diameter is increased in steps of 5 μm , from $\phi = 27$ to 52 μm for the SCF3 and, from $\phi = 25$ to 50 μm for the SCF4, to study the effect of the air hole size. The corresponding cross sections are shown in Fig. 5.6. The core diameter and bridge thickness are kept constant.

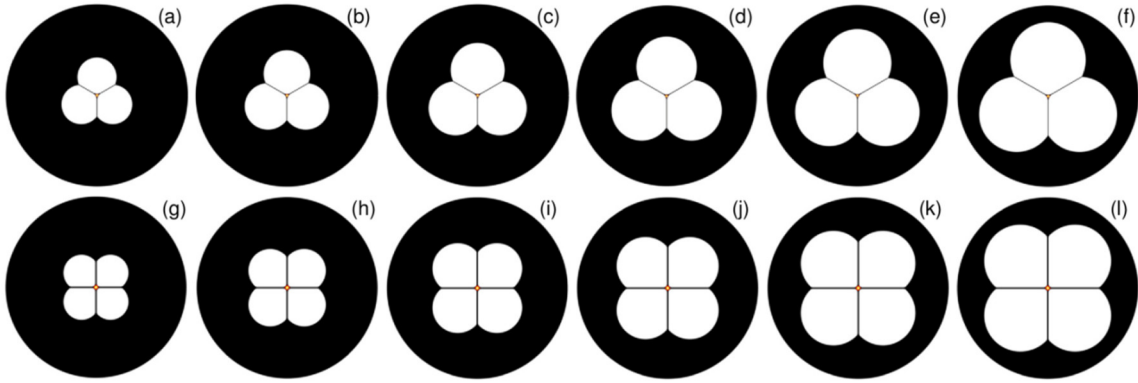


Figure 5.6: SCF cross sections for the investigation of the influence of the air hole diameter. (a)-(f) SCF3 diameter values from $\phi = 27 \mu\text{m}$ to $52 \mu\text{m}$. (g)-(l) SCF4 diameter values from $\phi = 25 \mu\text{m}$ to $50 \mu\text{m}$. The increment is $5 \mu\text{m}$ in both cases [74].

Figs. 5.7(a) and 5.7(b) show the modulated spectra of the FBG for the SCF3 and SCF4 compared to SMF, for the smallest and largest air hole diameter. The reflectivity of the side lobes in the SCF is significantly higher than in SMF in both cases. The relative increase in reflectivity η compared to the SMF varies between $\Delta\eta = 5\%$ and 48% for SCF3 and between $\Delta\eta = 16\%$ and 66% for SCF4. A higher reflectivity for the SCF4 is due to a larger confinement factor Γ and a smaller silica area A_s compared to the SCF3.

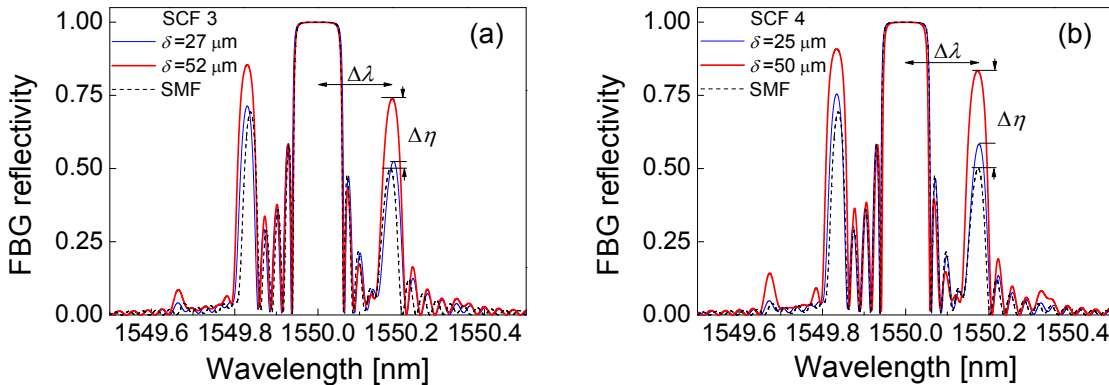


Figure 5.7: Modulated FBG spectra of (a) SCF3 of air hole diameters $\phi = 27$ and $52 \mu\text{m}$, and (b) SCF4 of air hole diameters $\phi = 25$ and $50 \mu\text{m}$ compared the modulated FBG spectra of the SMF [74].

Fig. 5.8(a) shows the side lobe reflectivity η variation for the SCFs with increased air hole diameter compared to the SMF. Note that the confinement factor Γ remains unchanged (Fig. 5.8(b)) and the increase in reflectivity is now caused by the strain variation, as shown in Fig. 5.8(c). The strain increases with the increasing air hole diameter which reduces the amount of silica area in the fiber cross section. As a result, the interaction between the acoustic power and the grating increases in the core, increasing the side lobe reflectivity.

The dependence of the side lobe separation $\Delta\lambda$ on the air hole diameter is shown in Fig. 5.8(e). Although the outer diameter effect on the strain and optical parameters is not considered in this study, it is expected that variations of outer diameter induce a similar effect compared to air hole variations. An increase in the outer diameter results in a larger overall silica area decreasing the strain in the core.

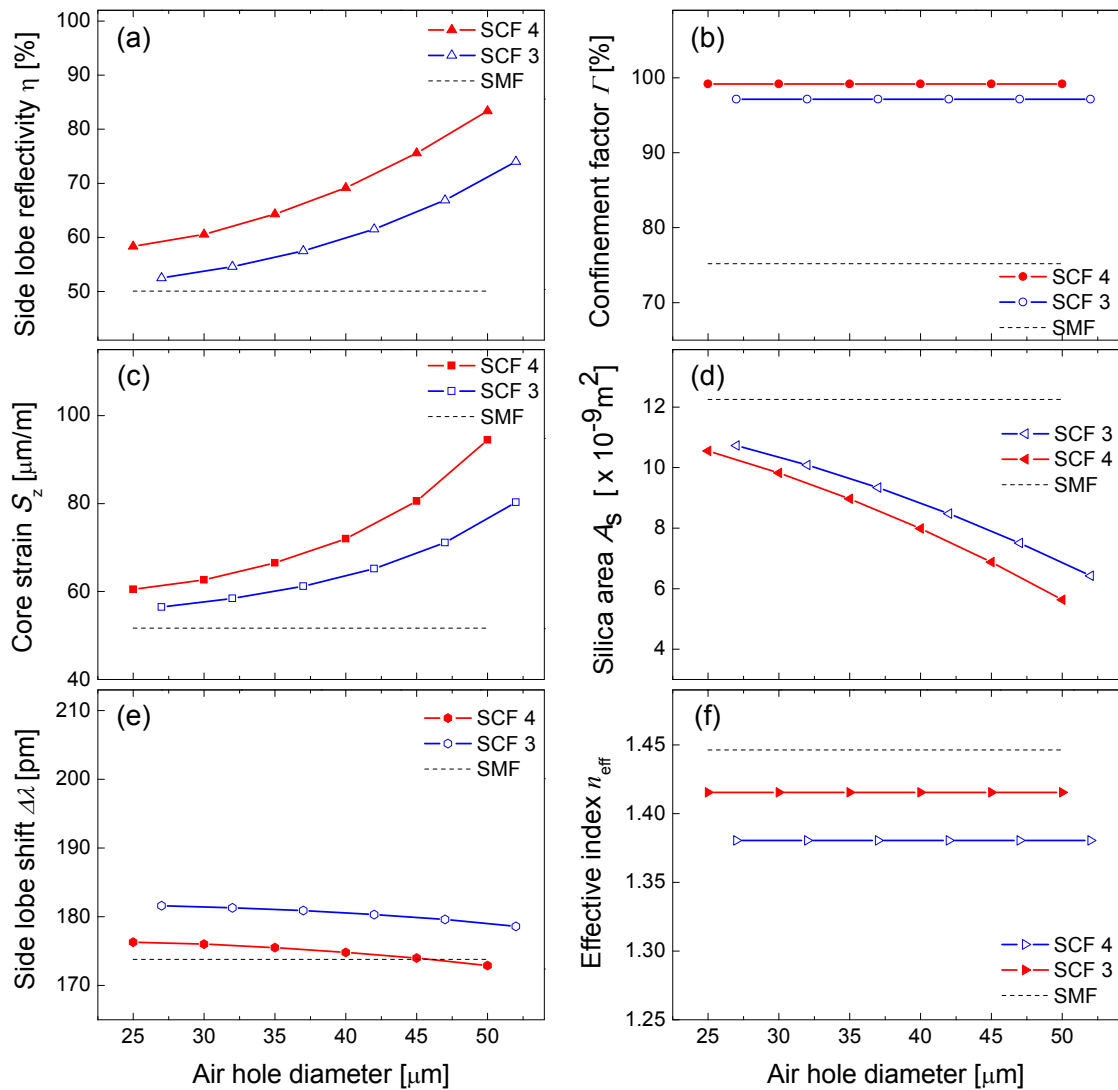


Figure 5.8: (a) Side lobe efficiency η , (b) confinement factor Γ , (c) strain S , side lobe shift $\Delta\lambda$ and effective index n_{eff} variation for the SCF air hole diameter range. All figures are at the same scale as in Fig. 5.5 to improve comparability [74].

The influence of the SCF air holes is compared to typical SMF parameters to estimate the importance of the increased reflectivity η in SCFs for the development of acousto-optic devices. Figs. 5.9(a)-(d) show, respectively, the equivalent modulation index Δn_{ac} , grating length L_g , acoustic power P_{ac} and cladding diameter D required for a modulated FBG in the SMF to achieve the same side lobe reflectivity obtained for the SCFs in Fig. 5.8(a). The parameters are calculated using Eqs. (3.1) and (3.2) and data provided in Sec. 5.1. The initial SMF parameters for $\eta = 50\%$ are shown in insets of Fig. 5.9. The SCF4 sample with the highest reflectivity $\eta = 83\%$ (50 μm air hole diameter) is compared to the SMF, in the following analysis, for example.

In summary, the results indicate that the use of the SCF with the largest air hole allows a reduction of the modulation index n_{ac} (75%), of the fiber/grating length (75%) and of the acoustic power (230%) to achieve the same modulation compared to the SMF in Figs. 5.9(a), 5.9(b) and 5.9(c), respectively. In addition, the modulation in the SCF is equivalent to a SMF with a diameter reduced up to 45% (Fig. 5.9(d)).

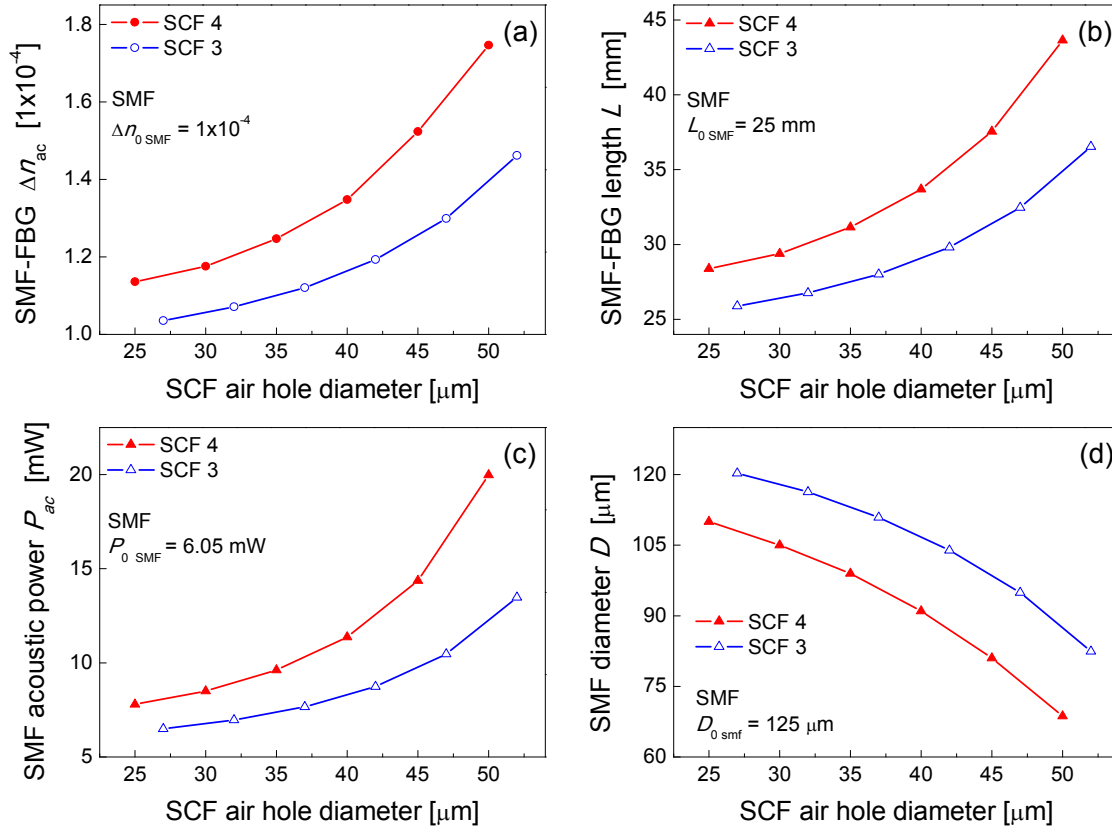


Figure 5.9: Equivalent FBG and SMF parameters required to achieve the same side lobe reflectivity η for variation of SCFs air holes. (a) SMF-FBG modulation index Δn_{ac} , (b) SMF-FBG length L_g , (c) SMF acoustic power P_{ac} and (d) SMF diameter D [74].

In summary, the interaction between longitudinal acoustic waves and fiber Bragg gratings in suspended-core optical fibers is numerically investigated to evaluate the influence of the core and air hole sizes on side lobe reflectivity and side lobe separation.

A relative increase in side lobe reflectivity up to 66% compared to the SMF case is obtained with the largest simulated air holes. This suggests that fibers with large air holes reduce the amount of silica in the cladding increasing the induced strain in the core. However, a minor decrease of the side lobe separation by increasing the air hole size is verified.

On the other hand, a higher side lobe reflectivity is achieved with larger cores because of an increased overlap of the guided mode with the Bragg grating. The possibility to induce higher efficiencies with larger fiber cores makes the SCF fabrication process easier and increases the mechanical stability of the acousto-optic interaction. Furthermore, the increased core diameter facilitates coupling between the acoustic horn and the fiber, and the optical coupling with standard fibers. However, a larger core size increases the number of supported optical modes and decreases the difference of the effective indices of the modes. An upper boundary of the core size is reached if the modulated FBG spectrum of the fundamental mode is superimposed by the modulated FBG spectrum of the next higher order propagating mode.

The side lobe separation increases with decreasing core size, which is caused by a decrease of the effective index. Therefore, the side lobe reflectivity and the wavelength separation are properties changing oppositely if the SCF core size is changed.

The increase of the side lobe reflectivity compared to the one in the SMF allows a reduction of the modulator size and the acoustic power required to excite the acoustic waves. Moreover, the SCF provides better mechanical stability compared to fiber taper techniques and protects the acoustic wave in the core, due to the acoustical shielding by the cladding against external acoustic noise.

An additional simulation by exciting transversely both fibers with the same force ($F = 1$ N) and frequency ($f = 1.091$ MHz) is performed to compare the acoustic efficiency between the SCF and the SMF to generate acoustic-tunable long period gratings (LPGs) [75]. The amplitude of the flexural acoustic wave in the SCF is 83% higher compared to the SMF, indicating a lower acoustic power is required to generate acoustic LPGs in SCF. However, for the modal coupling efficiency, a more detailed study of the modal beat length and its dependence on the acoustic frequency is required.

5.2 Reflectivity modulation of a FBG in a four holes SCF

The acousto-optic modulation of a fiber Bragg grating in a four holes suspended-core fiber is experimentally demonstrated. Modulations with a reflectivity amplitude decrease of 67% in the Bragg resonance are obtained. The reduction of the grating length and the acoustic power for achieving the acousto-optic modulation compared to previous studies employing conventional solid core single mode fibers points to more efficient modulator devices in suspended-core fibers.

5.2.1 Experiment and discussion

Fig. 5.10 illustrates the experimental setup used for the characterization of the modulated FBG spectrum with a detail of the cross section of the SCF used in the modulator. The SCF fabricated at Leibniz Institute of Photonic Technology (IPHT) is composed of four air holes of $\phi \sim 24 \mu\text{m}$ in diameter separated by silica bridges of $t \sim 700 \text{ nm}$ thickness, which form a solid core of $d = 5 \mu\text{m}$ incircle diameter. The fiber cross section diameter is $D = 100 \mu\text{m}$. A grating of 1 cm length is inscribed in the SCF by means of a femtosecond laser and two-beam interference using the Talbot interferometer arrangement according to the methodology described in [66,76]. The FBG is not apodized. The grating 3-dB bandwidth is 0.26 nm and the maximum reflectivity is $\sim 99\%$.

The acoustic waves are excited by an acousto-optic modulator being composed of a piezoelectric transducer (PZT disc of 2 mm thickness with diameter of 25 mm), a 5 cm long acoustic silica horn and a 5 cm long SCF with the inscribed FBG. The grating is characterized by a broadband source (LED) and the reflection spectrum is recorded by means of an optical spectrum analyzer (OSA) with a 50 pm wavelength resolution.

The SCF and SMF at the circulator are spliced by using an arc-discharge fusion splicer (Sumitomo F36) and a modified method to prevent the collapse of the core and the bridges [77]. The PZT is excited by a 1 V – 9 V sinusoidal signal from a signal generator at $f = 216 \text{ kHz}$, 343 kHz, 360 kHz and 497 kHz resonances, respectively.

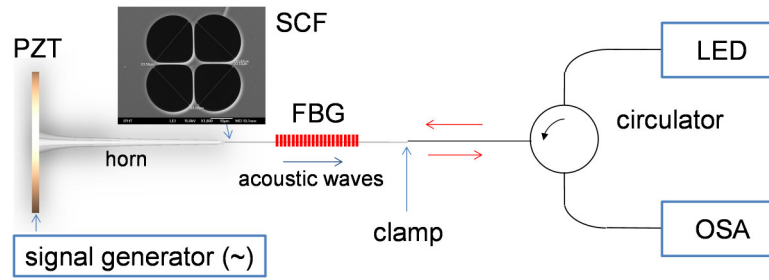


Figure 5.10: Experimental setup used to characterize the modulated FBG spectrum with a detail of the cross section of the four air holes SCF used in the modulator.

Fig. 5.11(a) shows the modulated FBG spectrum for the acoustic resonance at $f = 216$ kHz and the 1 V - 9 V voltage range applied to the PZT. The bandwidth change is not evaluated for this grating since the spectrum changes asymmetrically. The spectrum is normalized in linear scale in relation to the maximum reflectivity at $\lambda_B \sim 1538.46$ nm for the grating without acoustic excitation. The reflectivity variations for the modulated spectra are evaluated only at this wavelength. The side lobes on the short wavelength range of the Bragg resonance are caused mainly by the non-uniform average refractive index along the grating resultant of the inscription process and influence of overlapped higher-order modes [76,78].

Fig. 5.11(b) shows the FBG reflectivity variation for the $f = 216$ kHz, 343 kHz, 360 kHz and 497 kHz resonances and 1 V - 9 V voltage range applied to the PZT. The modulation is reduced at higher frequencies mainly because of the natural behavior of this acousto-optic modulation (Eq. (3.1)) and the decrease of the PZT deformations with the increased frequency, as discussed in Sec. 4.1.2. No relevant effect is observed at frequencies higher than $f = 500$ kHz.

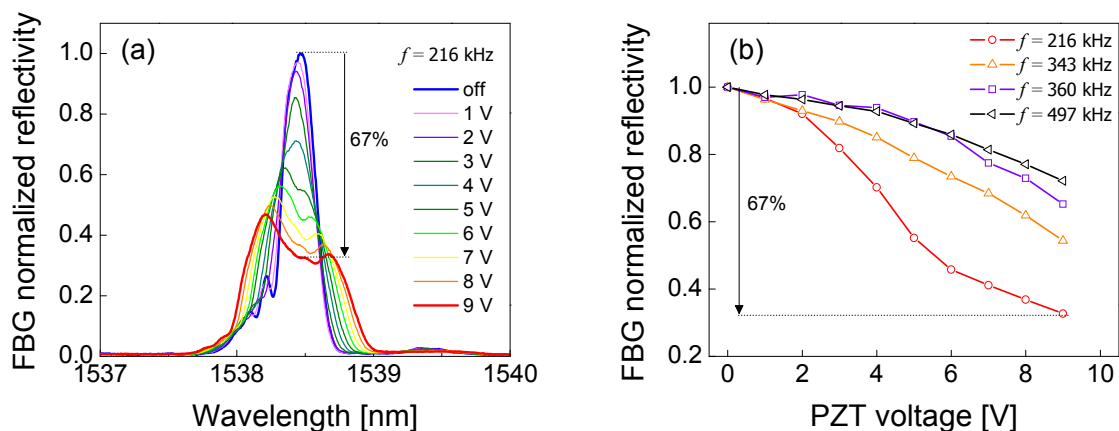


Figure 5.11: (a) Modulated FBG spectra for a 1 V - 9 V voltage range applied to the PZT at the resonance of $f = 216$ kHz. (b) Reflectivity modulation of the FBG for the considered resonances and voltage range [79].

Fig. 5.11(a) shows that the modulated reflectivity is higher at the shorter wavelength range. This is because the non-modulated grating already has intrinsic lobes on the left side. As a result, the acoustically induced lobes cause also higher reflectivity on the left side of the Bragg resonance, resulting in an asymmetric spectrum.

It is verified from previous works that a similar reflectivity modulation has been obtained by employing a SMF and a similar setup [56]. In that case, the grating inscribed in the SMF is 2 cm long and the PZT is excited at the resonance of $f = 230$ kHz. A RF signal amplifier is used to increase the voltage applied to the PZT up to 150 V. The maximum side lobe reflectivity modulation is 68% at 150 V. In comparison, a similar maximum modulation of 67% at $f = 216$ kHz is obtained. However, the grating inscribed in the SCF is 1 cm long (half the length) and the voltage used is 9 V (16x lower than the voltage applied in the SMF modulator). In summary, these previous results point to new possibilities to reduce the size and the power consumed by the acousto-optic devices.

5.3 Acousto-optic modulation of the FBG group delay in a four holes SCF

In this section, the acoustic modulation of the group delay of a broad FBG inscribed in a four holes suspended-core fiber is investigated. The grating bandwidth is increased, while adjusting the spectrum envelope to an almost Gaussian shape. An almost linear group delay response is obtained over a wavelength range larger than 0.7 nm. The tuning of the grating dispersion is also evaluated for a 6 V– 10 V voltage range.

5.3.1 Experiment and discussion

Fig. 5.12 illustrates the experimental setup used for the characterization of the modulated group delay and spectrum of the FBG. The PZT, acoustic horn and SCF are the same as described in Sec. 5.2.1. A grating of 1 cm length is inscribed in a 4.5 cm long SCF. The FBG spectrum has a 3-dB bandwidth of ~ 1 nm and a maximum reflectivity of 99%. The PZT is excited by a 6 V – 10 V voltage range with a signal generator at $f = 282$ kHz. For other frequencies no relevant effect is noticed. The grating is characterized by means of an optical network analyzer (ONA) with a 5 pm wavelength resolution.

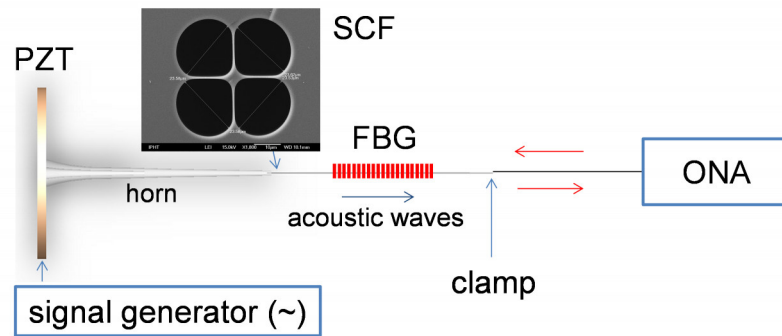


Figure 5.12: Experimental setup used to characterize the modulated group delay and spectrum of the FBG with a detail of the cross section of the four air holes SCF used in the modulator.

Fig. 5.13(a) shows the FBG spectrum without acoustic modulation (blue line) and with acoustic modulation (red line) for the resonance at $f = 282$ kHz and 10 V applied to the PZT. The non-modulated grating has intrinsic lobes on the left side, which are caused probably by the non-uniform average refractive index along the grating resultant of the inscription process and influence of overlapped higher-order modes [76,78].

However, the modulated spectrum shape is changed to a more Gaussian shape. The reflectivity amplitude is decreased 24% and the 3-dB bandwidth is increased 57% at 10 V. The side lobes composing the wider bandwidth are not resolved in the grating spectrum.

Fig. 5.13(b) shows the group delay for the grating without acoustic modulation (blue line) and with acoustic modulation for the resonance at $f = 282$ kHz and 10 V. The non-modulated grating shows a complex group delay response mainly in the wavelength range from 1539.6 nm - 1540.8 nm. Note in Figs. 5.13(a) and 5.13(b), the group delay varies rapidly with wavelength near the grating bandwidth edges and side lobes. This behavior of the delay and dispersion may be explained comparing the side lobes with separated uniform FBGs. For wavelengths outside the lobe bandwidth, the boundaries of the grating work as abrupt interfaces forming a Fabry-Perot cavity. The minima in the reflection spectrum are comparable to Fabry-Perot resonances, in which the light is trapped inside the cavity for many round-trips experiencing enhanced delay [40]. On the other hand, the acoustic wave induces side lobes overlapping in between the grating resonances causing an almost linear response of the group delay.

Fig. 5.13(c) shows the group delay in the wavelength range of 1539.6 nm – 1540.8 nm. This response is noticed over a 0.7 nm wavelength for the considered voltage range. It indicates a longer wavelength range compared to previous works employing solid standard fibers [9]. Since the modulated grating reflectivity and phase are changed by the amplitude of

the acoustic wave, the slope of the group delay in Fig. 5.13(c) is also changed due to the applied voltage.

Fig. 5.13(d) shows that the dispersion response of the grating has also an almost linear behavior for the 6 V – 10 V voltage range. The group delay wavelength range and the dispersion slope could be increased by increasing the voltage applied to the PZT or improving the modulator design. Other parameters as group delay ripple, time response and PZT frequency dependence are not investigated in this study. However, the results indicate good possibilities to compensate dispersion of optical channels in wavelength division multiplexing systems (WDM) or for application in fiber lasers or other dynamic filters requiring gratings with a tunable bandwidth.

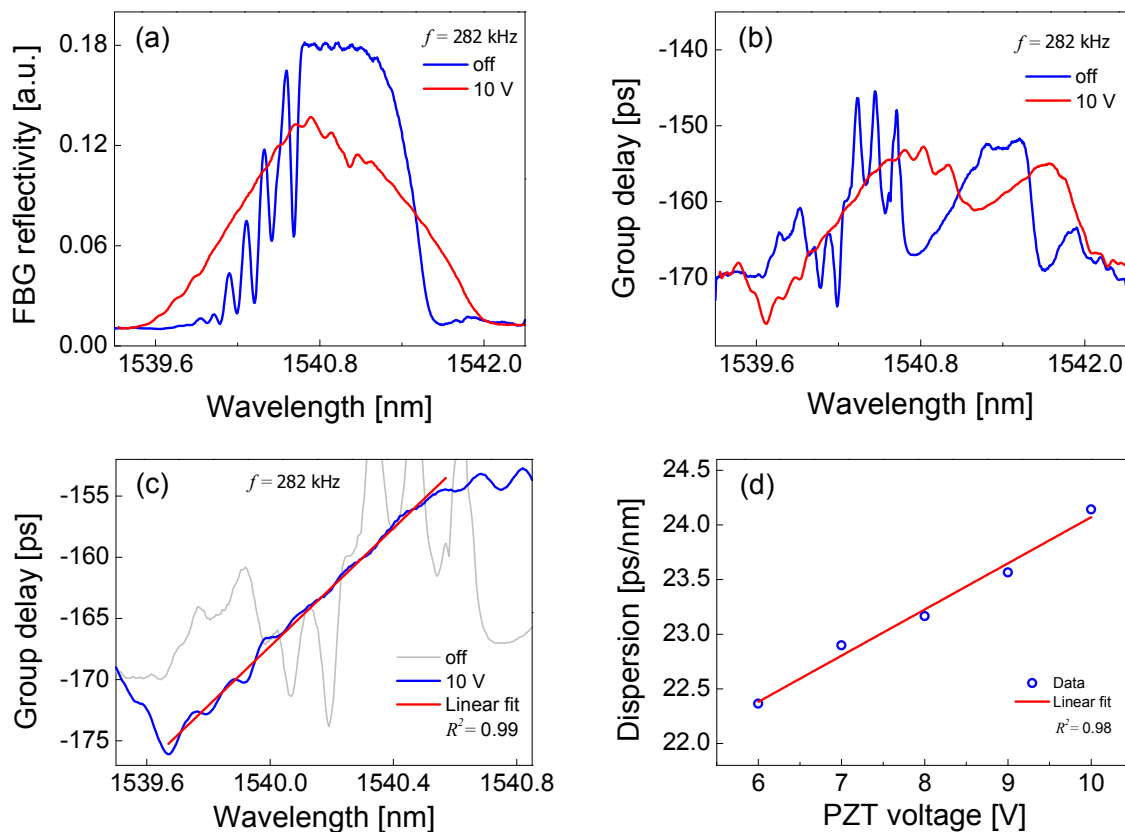


Figure 5.13: Modulated (a) spectrum and (b) group delay of a FBG in SCF at $f = 282$ kHz and 10 V. (c) Detail of the group delay response for the 1539.6 – 1540.8 nm wavelength range. (d) Dispersion modulation for a 6 V - 10V voltage range applied to PZT.

5.4 Reflectivity modulation of a FBG in a high birefringence SCF

Multi-wavelength erbium-doped fiber lasers employing birefringence optical fibers have attracted considerable interest because of their potential application in wavelength division multiplexing (WDM) fiber communication systems and optical fiber sensors. In optical fibers with linear birefringence, the two orthogonal axes are associated with two polarization modes with different effective indices n_{eff} . These modes are usually named as “fast Y” and “slow X” polarizations because they propagate in the fiber with different phase velocities ($v_Y=c/n_{effY} > v_X=c/n_{effX}$). The interaction of the two orthogonal modes with a FBG results in two reflected bands centered at wavelength resonances λ_Y and λ_X , which are separated according to the Bragg condition $\Delta\lambda_{XY} = 2\Delta n_{effXY}\Lambda$, in which, Δn_{effXY} , is the modal effective index difference between the two orthogonal modes and, Λ , is the grating period. For application in fiber lasers, external perturbations may change the properties of a grating inscribed in a low birefringence fiber, consequently, changing the wavelengths of laser emission. In addition, anisotropies in the refractive index of the active fiber can also induce a difference between the two orthogonal modes resulting in variations of the laser output [80]. For gratings in high-birefringence (Hi-Bi) fibers, the influence of external perturbations on the refractive index is small and the output of the laser is fixed by the spectral characteristics of the grating. Moreover, the cavity losses for both polarization modes can be adjusted by a polarization controller compensating the difference of reflectivity between the two grating peaks. Based on this approach, fiber lasers with single or dual-wavelengths tuned by means of a polarization controller have been demonstrated [81]. The use of two Hi-Bi FBGs in an erbium-doped fiber laser with two overlapping cavities allows to obtain simultaneous four-wavelength laser output by adjusting the polarization losses, the pump power and the EDF lengths in the laser cavities [82]. A multi-wavelength erbium-doped fiber laser by using only one cavity and FBGs inscribed in a few-mode Hi-Bi elliptical core fiber has also been reported [83].

In this section, the acousto-optic modulation of a Bragg grating in a high birefringence double-core suspended-core fiber (HB-SCF) is experimentally investigated. The grating reflectivity and bandwidth is strongly modulated at the resonance of $f=289$ kHz. In addition, the superposition between the orthogonal modes by an acoustically induced central lobe at $f=874$ kHz is also demonstrated. The results indicate high acousto-optic modulation in SCFs and new possibilities of dynamic filters for multi-wavelength applications.

5.4.1 Experiment and discussion

Fig. 5.14(a) shows the $D \sim 124 \mu\text{m}$ diameter cross section of the HB-SCF fabricated at the IPHT and used in the experiment. The fiber is composed of a rectangular solid silica region ($14 \mu\text{m}$ length \times $7.7 \mu\text{m}$ width) with an central air hole ($6 \mu\text{m}$ length \times $2 \mu\text{m}$ width) surrounded by four air holes of $\phi \sim 40 - 43 \mu\text{m}$ in diameter separated by silica bridges of $t \sim 2.7 \mu\text{m}$ thickness. The larger air holes and the central air hole form two similar birefringent solid cores, as shown in Fig. 5.14(a). A grating of 1 cm length is inscribed in the HB-SCF by means of a femtosecond laser and two-beam interference, using the phase mask interferometer arrangement according to the methodology described in [66,76]. The birefringence of the HB-SCF is estimated of the grating spectrum as $\Delta n_{effXY} \sim 2.2 \times 10^{-4}$. Fig. 5.14(b) illustrates the setup used for the characterization of the modulated spectrum. The acoustic waves are excited by an acousto-optic modulator being composed of a piezoelectric transducer (PZT disc of 2 mm thickness with diameter of 25 mm), a 5 cm long acoustic silica horn and a 4.4 cm long SCF with the inscribed FBG (this modulator is composed of the same PZT and horn employed to characterize the four holes SCF described in Sec. 5.2.1 to compare with previous results). The HB-SCF and the SMF connecting the circulator are spliced by using an arc-discharge fusion splicer (Sumitomo F36) and the method described in [77]. The fibers are carefully aligned and the coupling power is monitored in transmission by means of a power meter. The simultaneous power coupling between the SMF core to both HB-SCF cores 1 and 2 induces high insertion losses. Therefore, the SMF core is aligned only to one HB-SCF core. The PZT is excited by 1 V – 10 V sinusoidal signal of a signal generator (SG) at the $f = 289 \text{ kHz}$ and $f = 874 \text{ kHz}$ resonances. A polarization controller (PC) is employed to align the polarization directions to the fast (pol Y) and slow (pol X) axes of the HB-SCF.

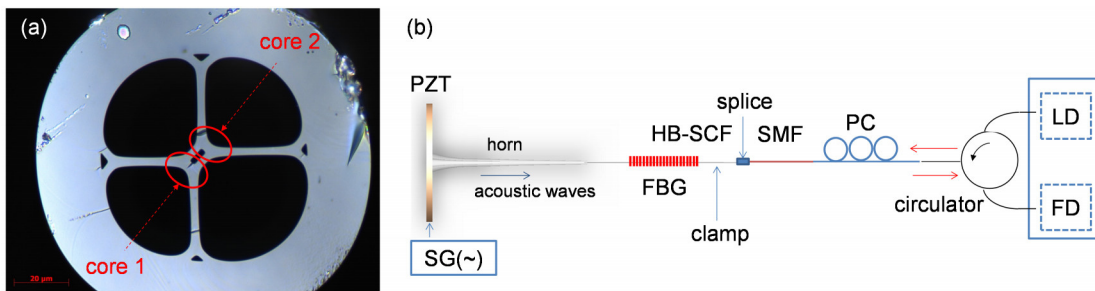


Figure 5.14: Illustration of (a) the HB-SCF cross section used in the modulator and (b) the experimental setup used to characterize the modulated FBG spectrum.

The modulated spectrum is characterized for the X, Y, and XY polarizations (45° between the orthogonal modes) by a tunable laser diode (LD) with an integrated photodiode with a 5 pm wavelength resolution (Agilent 8164A Lightwave Measurement System).

Fig. 5.15 shows the FBG spectrum for the polarizations (a) Y, (b) X and (c) XY for the grating without and with acoustic modulation at the resonance of $f = 289$ kHz and the maximum voltage of 10 V applied to the PZT. Fig. 5.15(d) shows the reflectivity modulation for the fast Y ($\lambda_Y \sim 1540.7$ nm) and slow X ($\lambda_X \sim 1540.9$ nm) modes for the 1 V – 10 V voltage range applied to the PZT. Note in Figs. 5.15(a), 5.15(b) and 5.15(d), that the decrease in the grating reflectivity is almost the same for both X and Y polarizations achieving a maximum of 84% at 10 V. Although a smaller reflectivity decrease is obtained for the XY polarization (72%), both X, Y and XY polarizations have almost the same 3-dB bandwidth increase (the bandwidth of the non-modulated grating increases from 0.07 nm to 1.7 nm at 10 V). The frequency response is not investigated in this study; however, it is observed during the experiment a decrease of the modulation strength for higher frequencies, as discussed in Sec. 3.1.

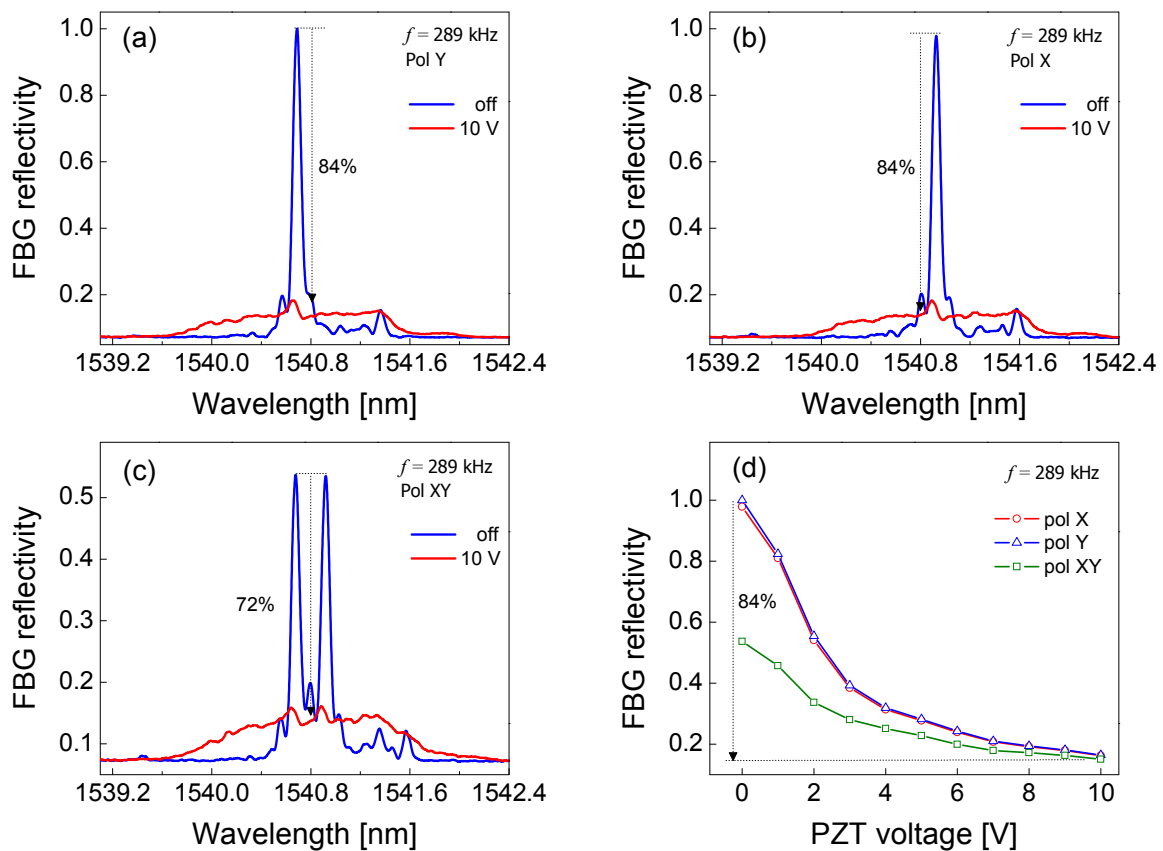


Figure 5.15: FBG spectrum for the polarizations (a) Y, (b) X and (c) XY for the grating without and with acoustic modulation at the $f = 289$ kHz resonance and 10 V. (d) FBG reflectivity modulation response for X, Y, and XY polarizations for the 1 V - 10V voltage range applied to the PZT.

A modulation of the reflectivity of 84% of a 1 cm long grating in HB-SCF indicates higher modulation efficiencies compared to previous studies employing standard single-mode fibers (~68% modulation at 150 V for a 2 cm long grating [56]), cladding etched fibers (~80% modulation at 30 V for a 1.5 cm long grating in a fiber with the diameter reduced to 30 μm [84]), and the four holes SCF discussed in Sec. 5.2 (~67% modulation at 9 V for a 1 cm long grating).

Fig. 5.16 shows the FBG spectrum for the polarizations (a) Y, (b) X and (c) XY for the grating without and with acoustic modulation at the $f=874$ kHz resonance and 10 V applied to the PZT. The longitudinal acoustic wave induces side lobes on both sides of the fast and slow modes. A maximum reflectivity modulation of ~42% is obtained at the Y and X peaks for the maximum 10 V. Fig. 5.16(e) shows the modulation of the reflectivity for the Y, X and XY polarizations for a 1 V – 10 V voltage range. Note in Fig. 5.16(e), while the reflectivity at the peaks λ_Y and λ_X decreases, the reflectivity of the induced side lobes increases up to a maximum of $\Delta\eta = 16\%$ compared to the non-modulated grating.

Note in Fig. 5.16(c), that the non-modulated grating has an intrinsic lobe centered at $\lambda_{XYC} \sim 1540.8$ nm overlapping the reflectivity of the fast and slow modes. It indicates the modes have the same effective indices and travel in phase at this wavelength. The PZT resonance $f=874$ kHz is purposely chosen to induce side lobes at coupling wavelength λ_{XYC} , as indicated in Figs. 5.16(a) and 5.16(b). Consequently, the induced side lobes couple power from the fast and slow modes to a superposed central lobe, as seen in Fig. 5.16(c). Note in Fig. 5.16(d), the central lobe is almost unchanged for both polarizations. Fig. 5.16(e) shows that the reflectivity of the fast and slow modes decreases by increasing the central lobe for the considered voltage range. Consequently, the fast, slow and superposed mode achieves the same reflectivity at 10 V.

The coupling to the central lobe is limited by the maximum of 10 V of the signal generator. However, it is expected that higher voltages applied to the PZT can couple a higher level of power to the superposed lobe. In addition, a higher reflectivity modulation could be obtained by improving the modulator design.

The frequency response is not investigated in this study. However, a reduction of the reflectivity of the central lobe is expected for acoustic excitation at frequencies in which the side lobe separation does not match with the coupling wavelength λ_{XYC} . Nevertheless, this detuning might be useful to adjust the reflectivity of the central and side lobes to the same

power level. In this case, an increase of voltage might induce five flat wavelengths, which is suitable for applications requiring multi-wavelength channels and fiber lasers.

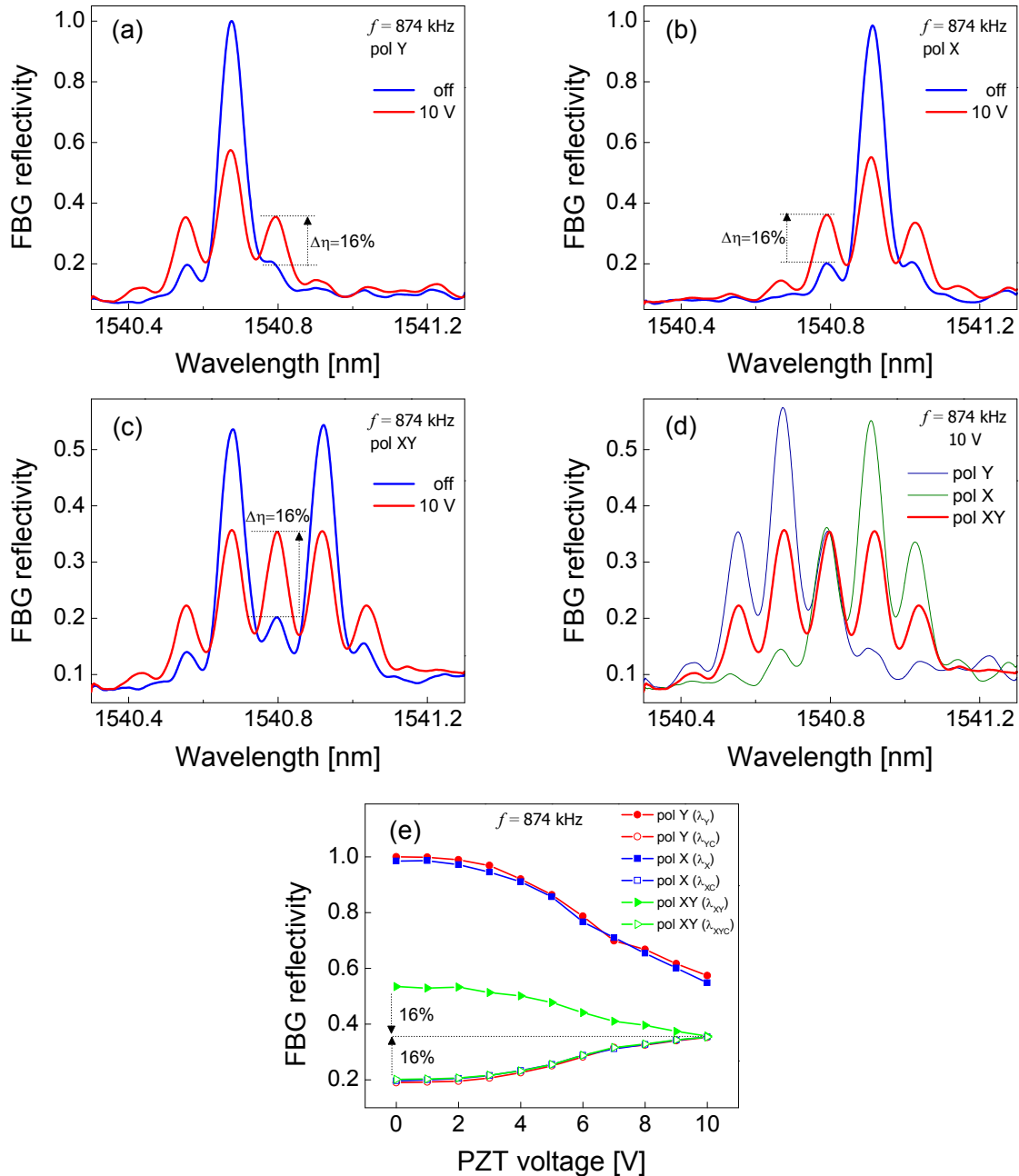


Figure 5.16: FBG spectrum for the polarizations (a) Y, (b) X and (c) XY for the grating without and with acoustic modulation at the resonance of $f = 874$ kHz and 10 V. (d) Comparison of the modulated spectrum for Y, X and XY polarizations at 10 V. (e) Reflectivity modulation for both modes for a 1 V – 10 V voltage range applied to the PZT.

6. Notch filter acoustically induced in a chirped fiber Bragg grating

Notch filters based on optical fibers are suitable for applications as gain equalizers in fiber amplifiers, as attenuation filters and band-rejection filters in fiber lasers [55,85,86]. Long period gratings (LPGs) inscribed permanently in optical fibers have been employed because their transmission parameters can be tuned by temperature and strain [86]. LPGs can also be obtained by mechanically pressing an optical fiber between a flat plate and a periodically grooved plate [87]. Other approaches to the fabrication of notch filters are implemented by introducing a permanent or dynamic phase-shift in a uniform fiber Bragg grating (FBG) or in a chirped fiber Bragg grating (CFBG). For example, the phase-shift in the grating structure is introduced by inserting ferrofluids in capillaries of microstructured optical fibers in which the grating is inscribed [88] or by transversally pressing a fiber in a very short region of the grating [89]. Nevertheless, such passive components are not appropriate to handle dynamic variations of the input optical power. Temperature-based techniques employing thermal heating provide an electrical control for dynamically inducing a phase-shift in FBGs [90]. However, the device response time is limited because of the slow material heating/cooling process.

In contrast to these known methods, acousto-optic devices permit a fast control of the modal and elasto-optic properties of optical fibers by electrically tunable acoustic waves. A device normally employed as a notch filter is based on the interaction of flexural acoustic waves and optical modes in a single-mode or multi-mode fiber. Although this approach provides relatively high rejection efficiencies (-34 dB) and reasonable switching times ($\sim 40 \mu\text{s}$), the devices in general require high electric power and long fiber lengths to achieve the acousto-optic modulation [2,3]. The interaction of acoustic waves with FBGs and LPGs is a good alternative for reducing the size, the switching time and the power consumed by the acousto-optic devices [10,85]. In particular, the interaction of flexural waves with long LPGs ($\sim 5 \text{ cm}$ length) allows the dynamic tuning of the grating transmission properties, which is suitable to equalize the gain of optical channels in erbium-doped fiber amplifiers (EDFAs) [85]. As discussed in Sec. 3.1, in standard single-mode fibers (SMFs), the acoustic power is distributed over the full fiber cross section, which reduces the overlap between the acoustic wave and the grating inscribed in the core.

The reflectivity modulation of a chirped fiber Bragg grating by acoustic waves is experimentally investigated in this section. To increase the interaction of the acoustic wave and the grating in a standard fiber, the modulator design is optimized by reducing the size of the PZT, of the acoustic horn and the optical fiber. The notch reflectivity significantly decreases by changing the electrical power compared to results of previous studies [3,85,87–89]. In addition, the notch bandwidth is also tunable. The results indicate strong acousto-optic interactions in short lengths of standard fibers, which is attractive for reducing the size and the power consumed by acousto-optic devices.

6.1 Physical principle

Fig. 6.1(a) illustrates the period variation and the resulting reflection spectrum of a chirped fiber Bragg grating (CFBG). An optical mode with effective index n_{eff} is propagating in z direction in a non-perturbed grating with a period varying linearly from Λ_1 to Λ_n . Consequently, the mode is reflected in different positions in the grating at the wavelength $\lambda_n(z) = 2n_{eff}\Lambda_n(z)$. The grating reflectivity and period variation are approximated as [41],

$$\mathfrak{R} = 1 - \exp\left(\frac{\pi^2 \Delta n_{ac}^2}{2n_{eff}^2 |C|}\right), \quad (6.1)$$

$$\Lambda_n(z) = \Lambda_0 + C(z - z_0), \quad (6.2)$$

in which, Δn_{ac} , is refractive index modulation and, $C = \partial\Lambda(z)/\partial z$, is the chirp parameter being usually expressed in nm/cm. Fig. 6.1(b) illustrates the grating reflection properties with acoustic modulation. The acoustic wave causes a periodic strain $S(z) = S_0 \cos(2\pi fz)$ in the grating with a maximum amplitude S_0 . The variation of the grating period caused by the induced strain $S(z)$ and the grating chirp in Eq. (6.2), is written using Eq. (2.25) as,

$$\Lambda(z) = \Lambda_n(z) \left[1 + (1 - p_e) S(z) \right], \quad (6.3)$$

in which, p_e is the elasto-optic constant. Note in Eq. (6.3), if the acoustically induced strain $S(z)$ is null or has a low amplitude, the grating period variation is mainly caused by the grating chirp. However, if the induced strain $S(z)$ achieves a maximum amplitude S_0 , the variation of the grating period $\partial\Lambda(z)/\partial z$ along the grating is mainly caused by the acoustic wave, reducing the grating reflectivity in Eq. (6.1). In other words, the acoustic wave induces a dynamic period variation in the grating (phase-shift) at the position of maximum strain S_0 , which

decreases the grating reflectivity at the optical wavelength λ_p . The acoustic period λ_L is longer than the grating length, as illustrated in Fig. 6.1(b). The periodic strain $S(z)$ also changes the adjacent grating periods Λ_n resulting in a rejection filter centered at the notch wavelength λ_p . The notch reflectivity/bandwidth and position of λ_p are tuned by the amplitude and position of the maximum strain S_0 in the grating. For acoustic excitation at frequencies in which the grating supports two or more acoustic wave peaks, more notches can be induced in the grating spectrum, which is suitable for multi-wavelength rejection filters.

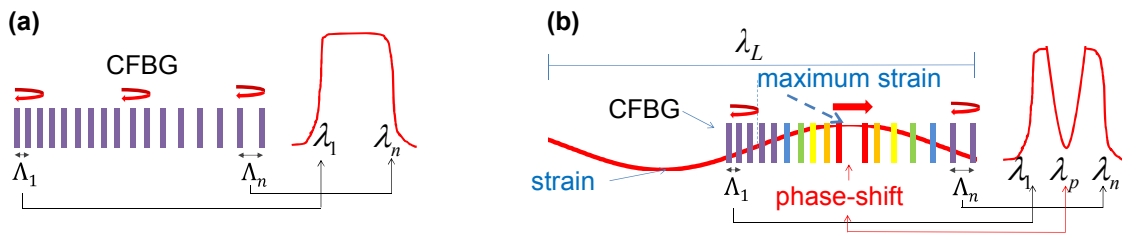


Figure 6.1: Behavior of a chirped fiber Bragg grating (a) without modulation and (b) with an acoustically induced phase-shift.

6.2 Experiment and discussion

Fig. 6.2 illustrates the setup used for the characterization of the modulated CFBG spectrum. A CFBG of 1 cm length is inscribed in the SMF by means of a chirped phase mask interferometer, based on two beam interferometry and a lateral nonhomogeneous beam splitter arrangement, according to the methodology described in [66,91]. The modulator is composed of a piezoelectric transducer (PZT) disc of 2 mm thickness and 5 mm diameter, which excites the acoustic waves by means of a solid silica horn of 2.3 cm length (tapered from 1 mm to 125 μm in diameter) and of the SMF with the inscribed CFBG. The whole modulator is 6.9 cm long. The PZT basis is fixed on a metallic support which is connected to a signal generator. Conductive glue is used to make the electrical connection between the PZT and the metallic support. By using this technique, conventional soldering methods which may cause undesired loads on the PZT are avoided.

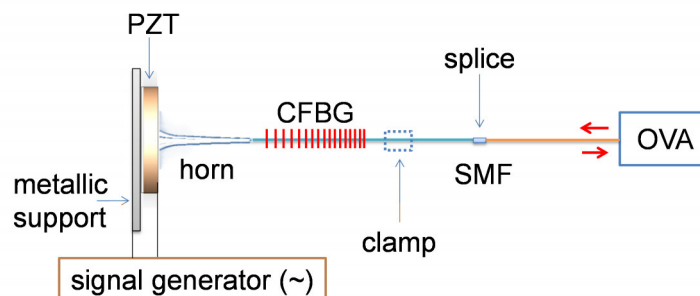


Figure 6.2: Illustration of the experimental setup used to characterize the modulated CFBG spectrum.

The fiber tip and PZT basis are fixed and the modulator works as a resonant acoustic cavity. The PZT is excited by a 6 V - 10 V sinusoidal signal at the $f=456$ kHz and $f=665$ kHz resonances. The grating is characterized by an optical vector analyzer (Luna OVA-5000) with a 1.6 pm wavelength resolution. The SMF of the modulator is spliced to the SMF connecting the optical vector analyzer by use of an arc-discharge fusion splicer, and the fiber with the grating is spliced to the silica horn.

Fig. 6.3(a) shows the CFBG spectrum without acoustic modulation and with acoustic modulation at the resonance of $f=456$ kHz for a maximum voltage of 10 V applied to the PZT. The non-modulated grating has the center wavelength at $\lambda_B \sim 1535$ nm, a 3-dB bandwidth of ~ 10 nm and a maximum reflectivity of $\sim 99.9\%$. No relevant notch effect in the CFBG spectrum is noted for voltages lower than 6 V. However, a notch filter is induced in the spectrum by increasing the voltage. The grating reflectivity is reduced from -5.8 dB to -32 dB by increasing the voltage from 6 V - 10 V. The notch wavelength is $\lambda_p \sim 1534$ nm for the maximum voltage of 10 V. The acoustic wavelength of $\lambda_L = 1.3$ cm is estimated by considering the longitudinal acoustic velocity in silica as $v_L = f\lambda_L = 5740$ m/s [73] and the resonance of $f=456$ kHz. As seen in Fig. 6.1(b), the acoustic wavelength $\lambda_L = 1.3$ cm is longer than the 1 cm grating used in this study, which supports only one acoustic wave peak.

Fig. 6.3(b) shows the modulated CFBG spectrum at $f=665$ kHz. Since the estimated acoustic wavelength is $\lambda_L = 0.86$ cm, the 1 cm grating now supports two acoustic wave peaks inducing two notches in the grating spectrum. The notch wavelengths are $\lambda_{p1} \sim 1533.1$ nm and $\lambda_{p2} \sim 1536.6$ nm. The reflectivity in the notches decreases with almost the same level from -3.7 dB to -22 dB for the 6 V - 10 V voltage range. However, a few lobes are noted in the second notch in the longer wavelength range. Note in Eqs. (6.2) and (6.3) that the grating period is longer with the increasing z . Therefore, the maximum strain S_0 probably increases the grating period Λ making the grating at this region to work as a Fabry-Perot cavity, reflecting narrowband resonant wavelengths on the longer wavelength range. This effect may be reduced by choosing proper grating and fiber parameters or by inscribing the grating for a shorter wavelength range.

Figs. 6.3(c) and 6.3(d) show the decrease of the reflectivity and of the 3-dB bandwidth with the voltage at the notch wavelength λ_p for the resonances at $f=456$ kHz and $f=665$ kHz. The notch bandwidth is reduced from 2.2 nm to 1.3 nm at $f=456$ kHz and, from 1.3 nm to 0.9 nm at $f=665$ kHz.

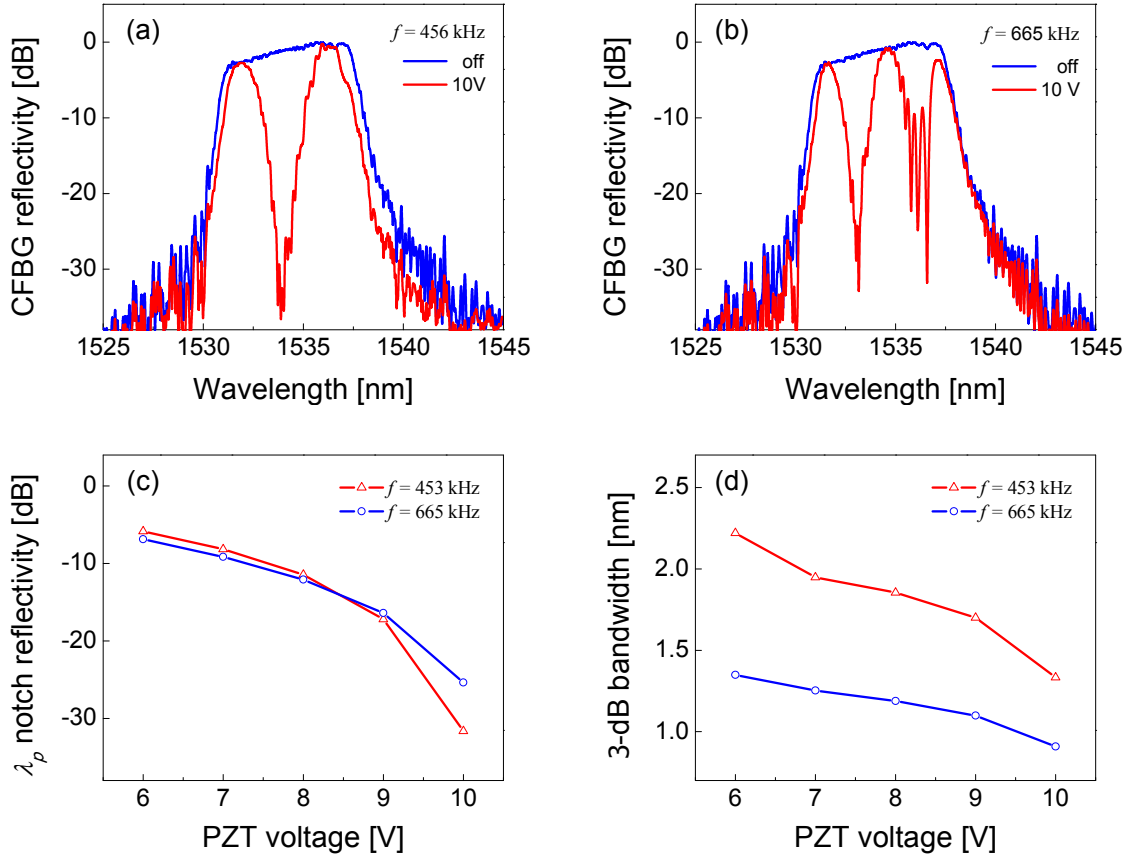


Figure 6.3: CFBG spectrum: without acoustic modulation (blue curve) and with acoustic modulation (red curve) at the (a) $f = 456$ kHz and (b) $f = 665$ kHz resonances and 10 V. (c) Notch depth and (d) bandwidth responses for the resonances and a 6 V – 10 V voltage range applied to the PZT.

Note that in Figs. 6.3(b) and 6.3(d), the frequency increase also narrows the bandwidth of the notches in the grating spectrum, because the shorter acoustic wavelength interacts with a shorter region of the grating with the increasing frequency. It is expected that higher frequencies can induce more notches in the grating spectrum, which might be limited by the grating bandwidth and the reduction of the induced strain. An increase of the notch depth could be obtained by the application of higher voltages to the PZT (in this study, the voltage is limited to a maximum of 10 V) or improvement of the modulator design, acoustic horn and PZT, or use of techniques already mentioned, such as, cladding etched, tapered fibers or suspended-core fibers.

The tuning of the wavelength λ_p is not investigated because of the discrete behavior of the PZT resonances used in this study. However, by employing acoustic drives with a broader frequency response, it is expected that variations of the acoustic frequency f (acoustic period) can sweep the phase-shift along the grating and, consequently, the notch wavelength λ_p .

7. Acousto-optic modulation of fiber lasers

Fiber lasers were reported for the first time just three years after the fabrication of the first laser [92]. However, they only received the appropriate attention after 1985 with the fabrication of rare-earth doped silica fibers and the development of the preform technology through modified chemical vapor deposition (MCVD) [93]. After the emergence of the first erbium doped fiber amplifier (EDFA), the optical sources based on fibers had significant progress [94]. Since then, fiber lasers with various dopants have been investigated, such as ytterbium, neodymium, aluminum and phosphorus [95–97]. In addition, novel types of hosts were developed, allowing the development of lasers for telecommunications, material processing, sensing and medicine [16–19]. Fiber lasers provide various advantages over other types of lasers, mainly due to intrinsic fiber characteristics, such as longer active media, compact and stable setup, and compatibility with the traditional optical fiber systems. The intrinsic low losses of the waveguide and the possibility of producing fiber cavities using Bragg grating reflectors have allowed lower pump thresholds and higher laser efficiencies [98].

Fiber lasers are stable and robust. As the light is guided in a flexible medium, it is easy to move the fiber end mechanically without the need for additional transport and directing optics which requires fine adjustment and alignment. Since the lasing is produced in a small diameter fiber core, the high beam quality allows for focusing the light in small spots, which is useful for applications such as micromarking, laser welding or metal microdrilling [17]. Optical fibers can also provide very high optical gain because the active medium can extend many kilometers long, e.g. in optical fiber amplifiers. Thus, several configurations supporting high power levels using CW or pulsed fiber lasers have been obtained, achieving in some cases, GWatt power levels [99]. Moreover, fiber lasers can be combined to build fiber sensors to monitor specific external parameters and, in many cases, with superior performance over other systems. Remote or inaccessible areas can be monitored by fiber sensors, since they allow remotely detecting the signal and transmitting it. In addition, they allow the detection of a huge volume of data, including real-time monitoring and quasi-distributed sensing [18]. Fiber sensors can be used in environments with high electromagnetic noise due to their electromagnetic immunity.

Fiber lasers are based on the stimulated emission to obtain coherent, collimated and frequency selected light. The simplest setup uses an optical fiber segment doped with an active element, a resonant cavity and a pump source. The optical pump energy is absorbed by the active region exciting its atoms to an upper energy state. The atoms can decay to the initial state emitting the stored energy in the form of optical radiation after a specific life time (spontaneous emission). These atoms are then stimulated (stimulated emission) by photons trapped in the resonant cavity generating amplified light (laser). The fiber laser must provide enough pump power to exceed the threshold and allow the laser operation. The gain must overcome the total loss, originated in the cavity, active medium, tuning elements and output laser.

Active mode-locking and Q-switching techniques have been commonly employed in fiber lasers to generate pulsed laser output. However, the bulk components typically employed to generate the pulses (e.g. electro-optic and acousto-optic modulators based on crystals [20,21]) cause high cavity losses. This requires higher pump energy to achieve the laser operation, which consequently reduce the overall performance of the laser. Moreover, bulk components can also degrade the laser beam quality, which requires fine alignment and good mechanical stability. On the other hand, acousto-optic modulators based on optical fibers have been successfully employed in Q-switched and mode-locked fiber lasers, enabling monolithic fiber setups [13–15,22–24]. In this context, FBGs and acousto-optic devices offer distinct properties to reduce the pump threshold and increase the laser efficiency, since that induce very lower loss.

In particular, longitudinal acoustic waves interacting with FBGs compress and extend the grating period inducing lobes on both sides of the Bragg wavelength [6,7,65]. AOMs employing standing longitudinal acoustic waves are suitable to mode-lock all-fiber lasers inducing amplitude modulated side lobes at twice the acoustic frequency [10,13–15]. An increase of the acoustic modulation frequency f_m and bandwidth B_m are important to shorten the pulse width τ of mode-locked fiber lasers, as described in [100],

$$\tau = \frac{1}{2\pi} \sqrt[4]{\frac{1}{mf_m^2 \left(\frac{B_m}{1.665}\right)^2}}, \quad (7.1)$$

in which, m , is the modulation depth, f_m , is the modulation frequency and, B_m , is the full width at half maximum (FWHM) bandwidth of the modulator in Hz unit. For an acoustically mode-locked fiber laser, f_m is twice the modulator frequency f and m is a parameter related to the maximum and minimum reflectivity R_{max} and R_{min} of the induced side lobe, calculated as $(R_{max} - R_{min})/R_{max}$ in linear scale [15]. However, the narrowband wavelength range modulated by the acoustic wave imposes a strong filtering in the very broad ytterbium bandwidth (FWHM > 40 nm [101]), resulting in a small wavelength range (axial modes) of the gain band for mode-locking. Since the modulated bandwidth increases by reducing the interaction length L_g between the acoustic wave and the grating (see Eq. (3.4)), the use of short Bragg gratings in the modulator is favorable to shorten the pulse width τ .

However, as discussed in Sec. 3.1, in standard single-mode fibers (SMF), the acoustic wave is mostly distributed over the whole fiber cross section A_s , reducing the interaction between the acoustic wave and the grating in the fiber core. Consequently, acousto-optic modulators (AOM) using long gratings L_g , high acoustic powers P_{ac} , cladding-etched and tapered fibers, have been employed to increase the acousto-optic interaction. For example, gratings of $L_g = 12$ cm length and voltages of $V_{PZT} = 16$ V applied to the piezoelectric transducer (PZT) have also been used in AOMs to produce mode-locking with 780 ps pulses width at a 9 MHz repetition rate [13]. High voltages $V_{PZT} = 20$ V and long gratings of $L_g = 10$ cm have also been employed to increase the acousto-optic interaction and produce a 740 ps pulses at 11 MHz in mode-locked ytterbium fiber lasers [14].

In this section, the interaction of acoustic waves and a Bragg grating in a three holes SCF is investigated, and its application in a mode-locked ytterbium-doped fiber laser is demonstrated. The use of suspended-core fibers is discussed in Sec. 5 indicating a good option to increase the acousto-optic modulation of Bragg gratings. The proposed modulator design permits a reduction of the grating length and the electric voltage applied to the PZT, which is desirable to shorten the pulse width and reduce the size and the power consumed by modulators.

7.1 Modulation of a FBG in three holes suspended-core fiber

Fig. 7.1(a) shows the $\phi = 127$ μm diameter cross section of the SCF fabricated at the IPHT and applied in the experiment. The fiber used in the modulator is 6.2 cm long and composed of a solid core of $d = 6$ μm incircle diameter surrounded by three air holes of $D \sim 44$ μm in diameter separated by silica bridges of $t \sim 1.5$ μm thickness. A FBG of 1 cm length is

inscribed in the SCF by means of a femtosecond laser and two-beam interference, using the phase mask interferometer arrangement according to the methodology described in [66,76].

Fig. 7.1(b) illustrates the experimental setup used for the characterization of the modulated FBG spectrum. A piezoelectric transducer composed of 2 layers (discs of 400 μm thickness and 5 mm in diameter) excites the acoustic waves by means of a solid silica horn (length of 1.8 cm with the cross section diameter tapered from 1 mm to 200 μm) and the SCF with the inscribed FBG. The two PZT layers are electrically connected in a stack configuration to increase the mechanical displacement of the horn, and, consequently, the amplitude of the acoustic wave [102]. The basis of one PZT is fixed on a metallic support connecting to a signal generator. Conductive glue makes the electrical connections between the two PZTs and between one PZT and the metallic support. Conventional soldering techniques which might cause loads on the PZT are avoided with this approach, increasing the strain induced by the acoustic wave in the fiber. The acoustic horn is attached to the PZT by means of a commercial adhesive being resistant to temperatures up to 100° degrees centigrade.

The SCF is spliced to a SMF using an arc-discharge fusion splicer and a method to prevent the collapse of the core and the bridges [77]. The splice loss is ~ 5 dB. On the opposite end, the SCF is spliced to the horn with the air holes and the core being intentionally collapsed, to increase the fused silica area at the SCF-horn interface and to reduce acoustic and optical reflections. The modulator works as a resonant acoustic cavity that allows exciting standing acoustic waves at certain resonant frequencies by fixing the PZT basis and the fiber tip. The PZTs are excited at 10 V sinusoidal signal at the $f = 5.0995$ MHz longitudinal resonance. The grating is characterized with the aid of a broadband superluminescent light source, and the reflection spectrum is recorded by means of an optical spectrum analyzer (OSA) with a 20 pm wavelength resolution.

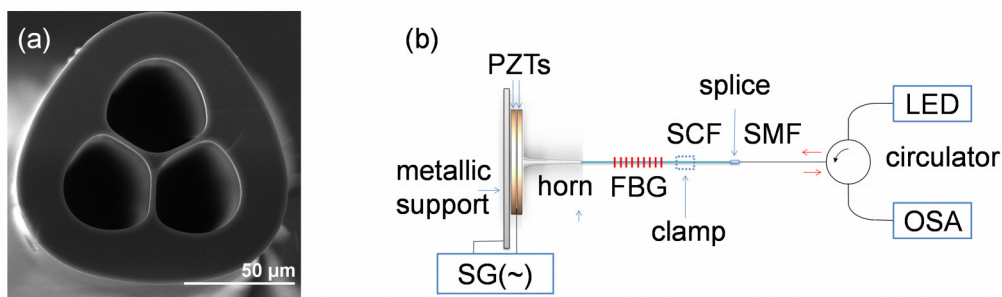


Figure 7.1: Illustration of (a) the SCF cross section used in the modulator and (b) the experimental setup used to characterize the modulated FBG spectrum.

Fig. 7.2 shows the FBG spectrum without acoustic modulation (dashed curve) and with acoustic modulation (solid curve). The non-modulated grating has the Bragg wavelength at $\lambda_B = 1065.8$ nm, a 3-dB bandwidth of 0.36 nm and a maximum reflectivity of $\sim 99.9\%$. The asymmetric spectrum caused by side lobes on the shorter wavelength range is caused by the high grating reflectivity and influence of higher order modes [76]. The PZT is excited with a signal amplitude of 10V at $f = 5.0995$ MHz inducing reflection lobes on both sides of the Bragg wavelength. The side lobe reflectivity falls and rises at twice the frequency of the electrical signal applied to the PZT, which is caused by the stationary oscillation of the acoustic wave. The laser resonator is designed on the basis of the side lobe on the longer wavelength range at $\lambda = 1066.24$ nm to avoid interactions with higher-order modes in the multimode fiber. Fig. 7.2 shows the modulated side lobe, indicating its separation of $\Delta\lambda \sim 350$ pm in relation to the Bragg wavelength and the increase of the reflectivity of $\Delta\eta \sim 11$ dB compared to the non-modulated grating. The effective lobe reflectivity is $\sim 8\%$.

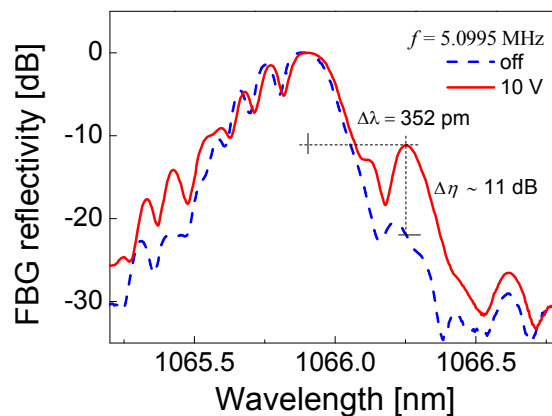


Figure 7.2: FBG spectrum: without acoustic modulation (dashed curve) and with acoustic modulation (solid curve) if the modulator is excited at 10 V and $f = 5.0995$ MHz. Short dashed lines show details of the side lobe separation $\Delta\lambda$ and modulation depth $\Delta\eta$ [10].

7.2 Acousto-optic mode-locked fiber laser

Fig. 7.3(a) illustrates the setup of the mode-locked fiber laser. The laser cavity is basically composed of two gratings, a delay line and an ytterbium-doped fiber providing the gain. An inset in Fig. 7.3(a) shows the cross section of the double D-shape doped fiber fabricated at the IPHT, with a length of 4.25 m and a core diameter of 10 μm . FBG 2 is inscribed in a double-clad fiber (Nufern FUD-3950). This grating has the Bragg wavelength at $\lambda_B = 1065.8$ nm, a 3-dB bandwidth of 0.39 nm and a maximum reflectivity of $\sim 50\%$. The reflection wavelength of FBG 2 is fine-tuned to the induced side lobe of FBG 1 by using a translational stage and a

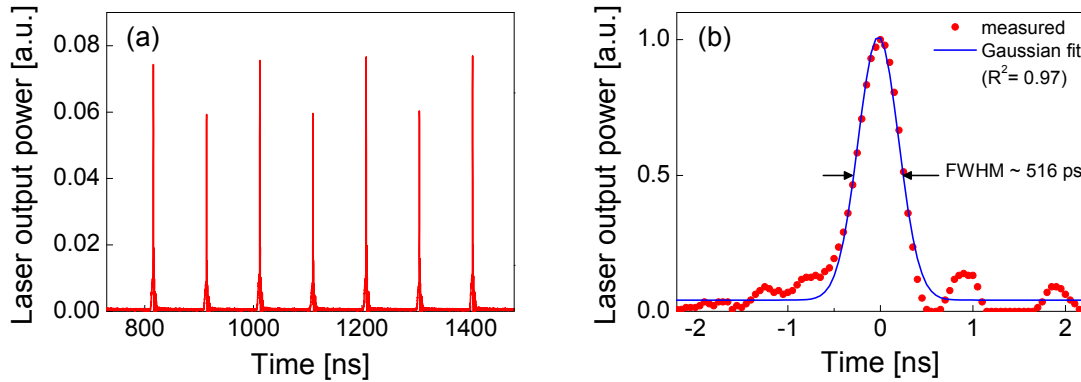


Figure 7.4: (a) Mode-locked fiber laser pulse train with repetition rate of 10.2 MHz generated for a 10 V electrical signal applied to the PZTs at $f = 5.1054$ MHz. (b) Measurement of a single laser pulse with a width less than 550 ps (FWHM) [10].

For the $L_g = 1$ cm grating length used in this study, the measured side lobe bandwidth $\lambda_{mFWHM} = 200$ pm, which is equivalent in frequency to 55 GHz. Since the cavity modes are spaced 10.2 MHz apart, the modulator is able to lock a large number of axial modes ($55 \text{ GHz} / 10.2 \text{ MHz} \sim 5400$ modes). Additionally, the lower modal effective index n_{eff} observed in SCFs compared to standard fibers also contributes to increasing the side lobe bandwidth λ_{mFWHM} and reducing the pulse width. For the SCF investigated, the effective index is estimated $n_{eff} \sim 1.43$. No relevant differences in the laser pulse shape are noticed in ± 5 kHz range. However, the best results of pulse widths, observed in the 500 - 600 ps range, are still far away from the theoretical lower limit around $0.315 / 55 \text{ GHz} = 6$ ps, considering a transformed limited laser pulse with an almost Gaussian shape in the time domain [14]. This is because the pulse width also strongly depends on other modulator and fiber cavity parameters which are not investigated in this study (e.g. side lobe reflectivity, modulation depth, pump power dependence and dispersion of the fibers composing the cavity and the active medium [100]). The use of fibers with high anomalous dispersion, such as SCFs, is also desirable to narrow the pulse width [103].

A laser efficiency of $\sim 2.3\%$ is obtained at a maximum averaged output laser power of 35mW and a maximum of 2.4 W pump power supported by the modulator. Beyond this pump power level, the power (which is not reflected by the modulated side lobe) being guided by the silica horn, reaches and damages the adhesive and the PZT surface. This drawback could be reduced or avoided by increasing the side lobe reflectivity by the application of higher voltages to the PZT (in this study, the voltage is limited to a maximum of 10 V) or by improvement of the modulator design, acoustic horn and PZT. Consequently, higher laser efficiencies and the output powers may be achieved. In addition, an increase of the laser efficiency could be obtained by reducing the losses at the splice between the SCF-SMF.

8. High frequency acousto-optic modulators for future fiber lasers

As previously discussed, the acoustic power is mostly distributed over the fiber cross section in standard optical fibers reducing the interaction with the grating in the core with the increasing frequency. For application at the 1060 nm wavelength range, devices operating at frequencies of $f = 5.58$ MHz employing long gratings lengths ($L_g = 10$ cm) have been reported [14]. However, the inscription of long gratings requires the use of long phase masks or additional equipment to shift the fiber and the phase mask with respect to the UV beam [66]. The use of long fibers or of long grating lengths increases the switching time of acousto-optic devices because the acoustic wave takes more time to travel along the fiber.

As discussed in Sec. 7, an increase of the acoustic frequency f , modulation depth m and the bandwidth is important to shorten the pulse width τ of mode-locked fiber lasers [100]. The results discussed in Sec. 7.2, with an ytterbium-doped fiber laser, show that a reduction of the grating length is useful to increase the modulated bandwidth and, consequently, shorten the pulse width. The modulation of a 1 cm grating in a SCF at 5.1 MHz has been demonstrated to mode-lock pulses shorter than ~ 550 ps. However, the inscription of gratings in SCFs and their fusion-splicing with standard fibers are a challenge and may require more elaborate techniques.

On the other hand, an increase of frequency requires the use of small and very thin PZTs, which are difficult to handle and manipulate. A reduction of the PZT thickness to increase the resonance frequency also decreases the amplitude of the deformations of the acoustic modes, being this effect more relevant with the increasing frequency. Consequently, it also reduces the acousto-optic interaction in the grating, requiring the use of small and special acoustic components to amplify the acoustic wave.

In this section, two distinct approaches of acousto-optic modulators of fiber Bragg gratings at 1065 nm wavelength and frequencies higher than 10 MHz are investigated. The devices are based on distinct components to increase the acousto-optic interaction and frequency. In addition, the modulators setup could be employed as output couplers in future fiber lasers, avoiding the heating and damage of the PZT caused by the remaining transmitted laser power through the grating, and consequently, allowing higher pump and output laser powers.

8.1 Interaction of longitudinal acoustic waves and a FBG in a tapered optical fiber

As discussed in Sec. 3.1, the side lobe reflectivity η is increased by increasing the index modulation Δn_{ac} or the grating length L_g , or by reducing the cladding cross section A_s . Consequently, several approaches of modulators operating at the wavelength range of $\lambda = 1550$ nm and the frequency range of $f \sim 5$ MHz have been proposed. Devices using long grating lengths ($L_g = 12$ cm) in combination with voltages of $V_{PZT} = 16$ V applied to the PZT achieve high reflectivity modulation [13]. Combination of gratings inscribed in tapered fibers have allowed the reduction of the grating length ($L_g = 5$ cm) while keeping higher voltages ($V_{PZT} = 38$ V) to achieve strong modulations [24]. For acoustic excitation at $f \sim 5$ MHz in the $\lambda = 1060$ nm - 1090 nm wavelength range, the use of long gratings $L_g = 10$ cm and voltages of $V_{PZT} = 20$ V have been convenient to achieve modulations of $\eta \sim 55\%$ [14]. Although the use of long gratings is useful to increase the acousto-optic interaction, long gratings narrow the modulated bandwidth increasing the pulse width of mode-locked fiber lasers. In addition, the splice between the acoustic horn tip and the fiber (which is usually required to increase the coupling of the acoustic power to the fiber) might induce optical reflections reducing the maximum modulation depth, which is also important to shorten the pulse width.

In this section, an acousto-optic device modulating a 1 cm long FBG at 1065 nm wavelength and with resonances at $f = 5.1$ MHz, $f = 10.8$ MHz and $f = 13$ MHz is experimentally investigated. The device is based on a high reflectivity grating inscribed in a tapered optical fiber to enhance the acousto-optic interaction. A distinct side coupling technique is applied to couple the acoustic wave from the horn to the fiber. High modulation efficiencies at the $f = 5.1$ MHz resonance are obtained.

8.1.1 Experiment and discussion

Fig. 8.1 illustrates the acousto-optic modulator and the experimental setup used to characterize the grating spectrum. The AOM is composed of a piezoelectric transducer (PZT) disc, a solid acoustic horn and a single-mode optical fiber (SMF). The fiber diameter is reduced from ~ 130 μm to ~ 55 μm along ~ 12 mm length by using the commercial machine Vytran GPX-3200 and the technique describe in [104]. The taper transitions are ~ 10 mm long

and have an almost linear profile. Fig. 8.1(a) shows the scanned profile of the tapered diameter. A grating of 1 cm length is inscribed in the tapered diameter by means of a femtosecond laser and two-beam interference, using the phase mask interferometer arrangement according to the methodology described in [66].

The acoustic horn is obtained by tapering a solid silica rod using a similar technique as applied to the fiber taper. The silica rod diameter is reduced from 1 mm to $\sim 50 \mu\text{m}$ along a $\sim 22 \text{ mm}$ length. The horn tip is aligned on the side of the SMF and fused together along a 3 mm by using a conventional splice machine. The horn tip and fiber are carefully aligned during the fusion process to avoid microbends and to increase the fused surface area. Later, the fiber is characterized with a helium neon laser to check the coupling of the power from the fiber to the acoustic horn through the fused region. No power transmitted through the horn is noticed. Fig. 8.1(b) shows the fused region between the horn tip and the SMF with a helium neon laser at the fiber end. Fig. 8.1(c) illustrates the PZT disc (0.2 mm thickness and 3 mm diameter) in yz and xy planes. Fig. 8.1(d) illustrates the acousto-optic modulator with the PZT, silica horn and the optical fiber indicating the tapered region. The whole modulator is $\sim 8.3 \text{ cm}$ long.

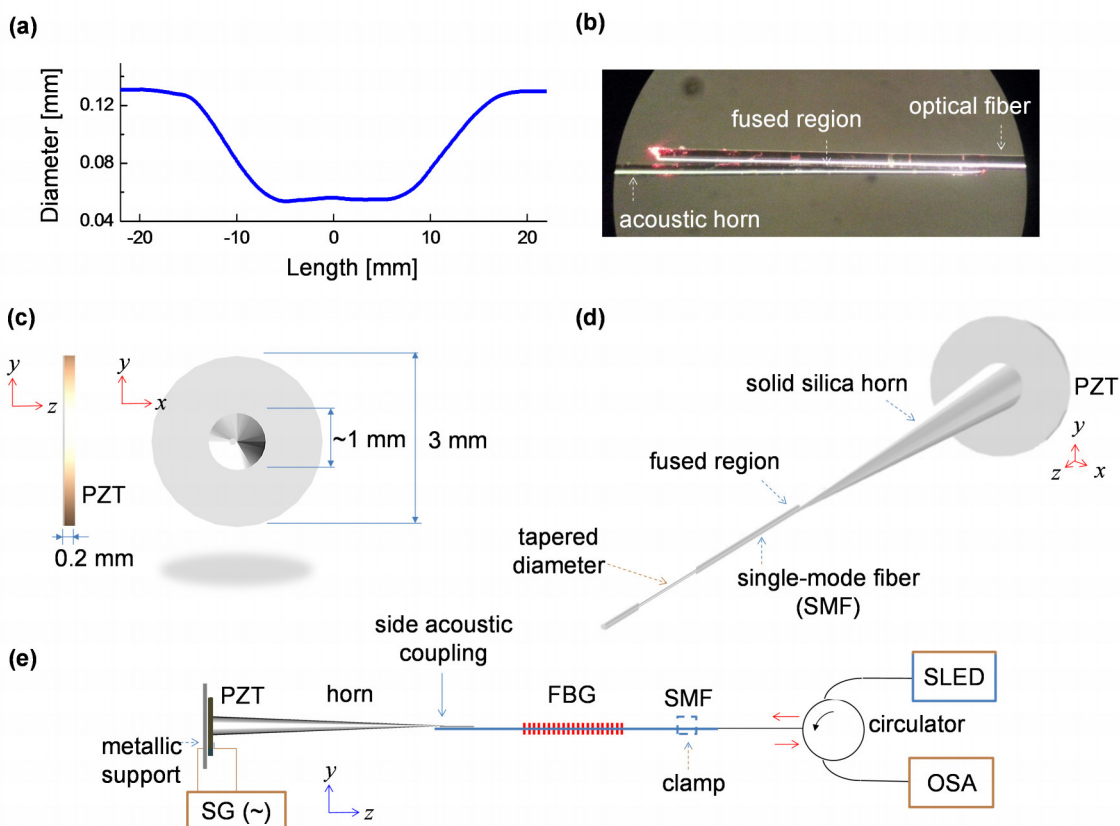


Figure 8.1: (a) Scanned profile of the tapered diameter in the SMF. (b) Microscope image of the fused region between the horn tip and the SMF. Illustrations of the (c) PZT, (d) acousto-optic modulator and (e) experimental setup.

Fig. 8.1(e) illustrates the experimental setup used to characterize the reflectivity spectrum of the FBG. The PZT basis is fixed on a metallic support connecting to a signal generator (SG). The electrical connection between the PZT and the metallic support is made by using conductive adhesive, which avoids the use of conventional soldering methods which might cause undesired loads on the PZT. The fiber tip and PZT basis are fixed and the modulator works as a resonant acoustic cavity exciting standing acoustic waves. The PZT is excited by a 9 V - 16 V sinusoidal signal at the resonances of $f = 5.1$ MHz, $f = 10.8$ MHz and $f = 13$ MHz. No relevant modulation is noticed for other resonances higher than 5 MHz. The grating is characterized by using a broadband light source (SLED), and the reflection spectrum is recorded by means of a circulator and an optical spectrum analyzer (OSA Yokogawa AQ6370C) with 20 pm wavelength resolution.

Fig. 8.2 shows the FBG spectrum without acoustic modulation and with acoustic modulation at the resonances of $f = 5.1$ MHz, $f = 10.8$ MHz and $f = 13$ MHz. The non-modulated grating has the Bragg wavelength at $\lambda_B \sim 1065.05$ nm, a 3-dB bandwidth of 0.7 nm and a maximum reflectivity of $\sim 99.9\%$.

Fig. 8.2(a) indicates the first order induced side lobes for a voltage of 16 V applied to the PZT at the resonance of $f = 5.1$ MHz. Note in Fig. 8.2(a), the reflectivity of the right side lobe achieves a saturation indicating also the modulation of second order side lobes. The absolute reflectivity of the right side lobe is $\eta \sim 72\%$. However, the side lobe overlaps with the Bragg wavelength because of its wide bandwidth and a non-uniform spectrum. On the other hand, the left side lobe remains resolved in the grating spectrum with an absolute reflectivity of $\eta \sim 30\%$. The modulation depth is $\Delta\eta = 14$ dB and the side lobe separation is $\Delta\lambda \sim 470$ pm. The difference of the reflectivity for the right and left side lobes might be caused by a difference of positive and negative strains interacting with the grating. In other words, the grating length supports a longer region of acoustic tension than compression, inducing a higher reflectivity in the right lobe.

Fig. 8.2(b) shows the reflectivity variation of the right (R) and left (L) side lobes for a 6 V – 16 V voltage range applied to the PZT. Note the reflectivity of the right side lobe achieves saturation at 15 V and slightly decreases for higher voltages. It is expected that higher voltages applied to the PZT could decrease the reflectivity of the first order side lobes while increasing the reflectivity of the second order side lobes, which is useful to avoid the overlap with the Bragg wavelength.

Fig. 8.2(c) show the first order induced side lobes for a voltage of 16 V applied to the PZT at the resonance of $f = 10.8$ MHz. The reflectivity of the right side lobe is $\eta \sim 5\%$. A decrease of the side lobe reflectivity is expected with the increased frequency, as discussed in Sec. 3.1. The modulation depth is $\Delta\eta \sim 2$ dB and the side lobe separation is $\Delta\lambda \sim 800$ pm. Fig. 8.2(d) shows the reflectivity variation of the right (R) side lobe for a 6 V – 10 V voltage range. It is expected that higher voltages applied to the PZT could increase the reflectivity of the first order side lobes, since no saturation is noted in the reflectivity-voltage response.

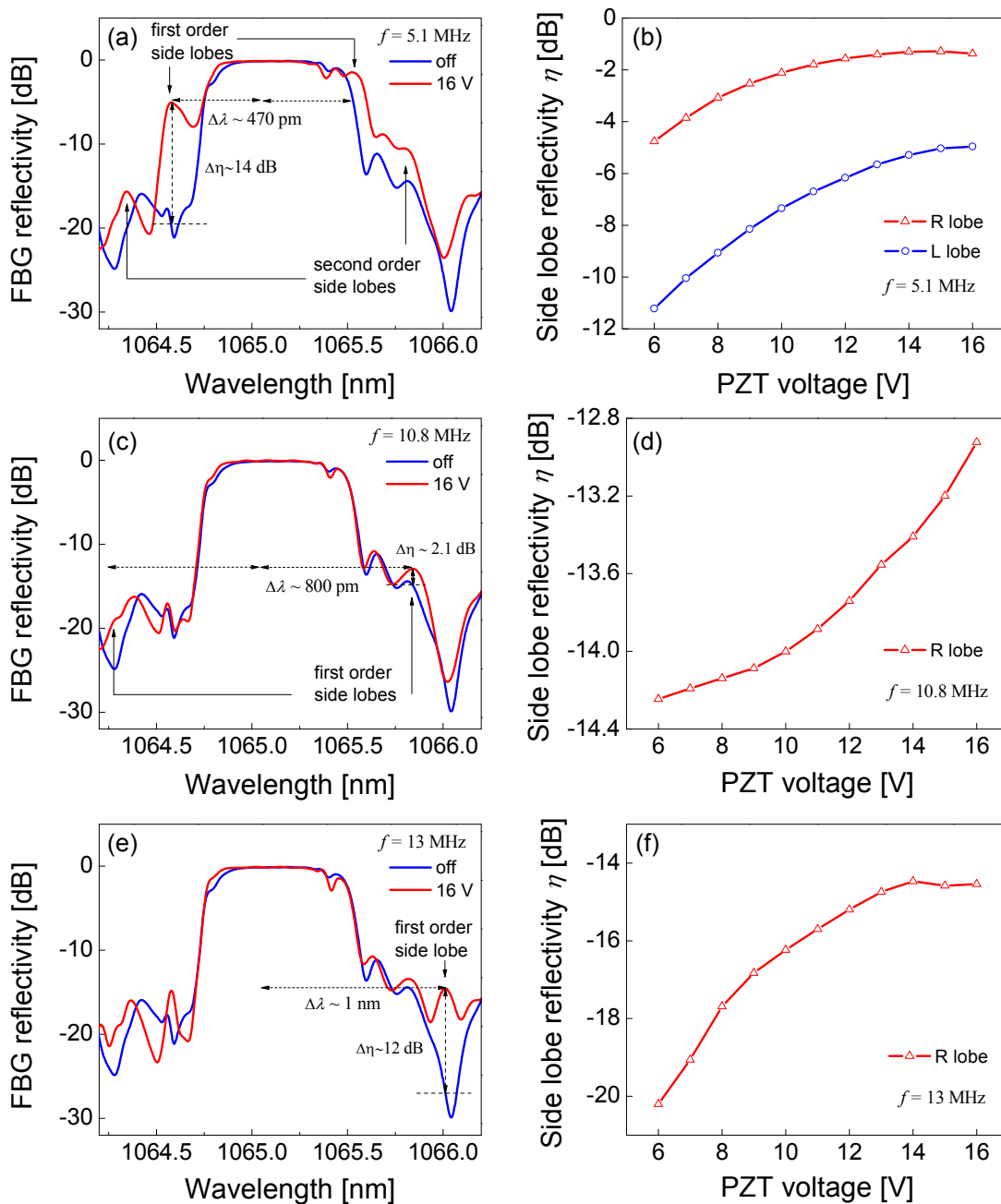


Figure 8.2: FBG spectrum: without acoustic modulation (blue line) and with acoustic modulation at 16 V (red line) and reflectivity variation of the modulated side lobe for a 9 V - 16 V voltage range applied to the PZT at the resonances of (a) (b) $f = 5.1$ MHz, (c) (d) $f = 10.8$ MHz and, (e) (f) $f = 13$ MHz.

Fig. 8.2(e) shows the right side lobe for a voltage of 16 V at the resonance of $f = 13$ MHz. No evident left side lobe is noticed on the shorter wavelength range, indicating that the side lobe might be overlapped with low reflectivity reflection noise. The right side lobe has an absolute reflectivity of $\eta \sim 3.5\%$, a modulation depth of $\Delta\eta \sim 12$ dB and a separation of $\Delta\lambda \sim 1$ nm. However, Fig. 8.2(f) shows that the reflectivity variation of the modulated side lobe achieves saturation at a voltage of 14 V, which is different from the behavior at other resonances. This effect might be caused by an induced radial strain decreasing the longitudinal strain along the fiber with the increasing frequency (this effect is discussed in the Sec. 8.2.1). Another reason might be associated with the PZT saturation at this resonance. However, both resonances have a similar 3-dB bandwidth of $\lambda_{sFWHM} \sim 100$ pm indicating a broader bandwidth compared to previous studies ($\lambda_{sFWHM} = 3.6$ pm) [14].

An unexpected DC wavelength shift of the grating spectrum with the modulated side lobe is also noticed during the experiment with the increasing voltage applied to the PZT. Fig. 8.3(a) shows the DC wavelength shift measured at the right side lobe for the considered resonances. This effect might be caused by a constant longitudinal strain resultant of a rearrangement of the grating structure compared to the grating state during the inscription process. However, the grating spectrum and the modulated side lobe remain stable after the voltage applied to the PZT is fixed. A maximum DC shift of 436 pm, 136 pm and 415 pm as noticed at the resonances of $f = 5.1$ MHz, $f = 10.8$ MHz and $f = 13$ MHz, respectively, compared to a grating without modulation. Nevertheless, the effect might be useful to tune the modulated side lobe to the reflection spectrum of the feedback grating employed in the laser cavity, as discussed in Sec. 7.2, avoiding the use of the temperature/strain techniques to tune the grating. The frequency dependence of the induced side lobe for the considered resonances is almost linear and shown in Fig. 8.3(b).

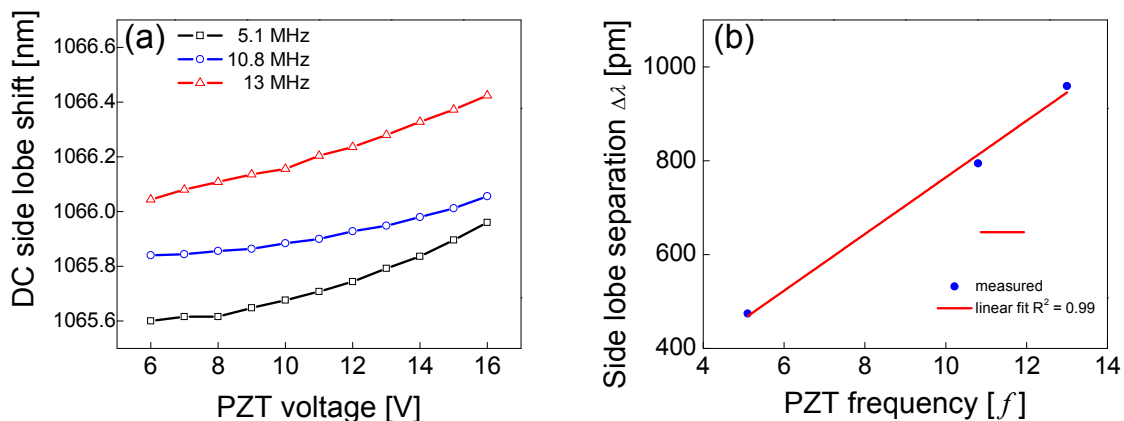


Figure 8.3: DC side lobe shift for a 9 V - 16 V voltage range applied to the PZT at the resonances of $f = 5.1$ MHz, $f = 10.8$ MHz and $f = 13$ MHz. (b) Dependence of the side lobe separation with the resonances.

8.2 Modulation of a FBG by an acoustically induced radial long period grating

Acoustically induced long period gratings (LPGs) are usually employed as notch filters with high rejection efficiencies and relative fast switching times ($\sim 40 \mu\text{s}$). The first approach of a coaxial acousto-optic modulator to induce a LPG is based on the interaction of flexural acoustic waves and modes in an optical fiber. The AOM is composed of an optical fiber passing through a drilled piezoelectric transducer (PZT) and a cone-shaped capillary silica horn axially aligned [55]. The acoustic wave creates bends along the fiber inducing a periodic refractive-index perturbation which couples power of the fundamental mode to higher-order modes. However, the AOMs in general require long fiber lengths or high powers to achieve the acousto-optic modulation [2].

In contrast, the acousto-optic modulation of fiber Bragg gratings (FBGs) by means of flexural acoustic waves enables the switching of the Bragg wavelength by coupling power of the fundamental mode to higher-order modes at shorter wavelengths [4,5]. However, the modulation of standard fibers with flexural acoustic waves is limited for frequencies $f < 10 \text{ MHz}$ because the acoustic wave tends to propagate on the fiber surface with the increasing frequency, reducing the interaction with the optical modes in the core [11,12].

On the other hand, as discussed in previous sections, longitudinal acoustic waves interacting with FBGs compress and extend the grating period inducing lobes on both sides of the Bragg wavelength. In general, modulators based on longitudinal waves operate with higher frequencies and velocities compared to the devices employing flexural waves [12], which is suitable to shorten the pulse width of mode-locked fiber lasers. In addition, an increase of the acoustic velocity v reduces the switching time of the acousto-optic devices, because the acoustic wave takes shorter time to propagate along the grating.

In this section, an acousto-optic device modulating a 1 cm long FBG at $\lambda = 1065 \text{ nm}$ wavelength and $f = 10.9 \text{ MHz}$ is experimentally investigated. The results indicate that the acousto-optic interaction can be based on an acoustically induced radial long period grating (RLPG) and a FBG. The RLPG couples power of the forward-propagating fundamental mode to backward-propagating higher-order modes supported by the FBG. The device can be used as an output coupler and exhibits a higher modulation frequency compared to previous studies using flexural acoustic waves, which is suitable to shorten the pulse width of mode-locked ytterbium-doped fiber lasers at the repetition rates higher than 20 MHz.

8.2.1 Physical principle

Fig. 8.4(a) illustrates a fiber Bragg grating (FBG) without acoustic modulation. The forward propagating mode with the effective index n_{01} , interacts with a grating of period Λ , resulting in a reflected band at the Bragg wavelength $\lambda_B = 2n_{01}\Lambda$. Fig. 8.4(b) illustrates an acoustically induced radial long period grating (RLPG) composed by the superposition of radial and longitudinal strains along an optical fiber. The distribution of the radial and longitudinal strains changes over the fiber cross section with the radius r (r varies from the fiber axial center (zero) to the maximum value a). Previous theoretical studies show that for acoustic excitation in an optical fiber with diameter $2a = 125 \mu\text{m}$, at frequencies in general higher than $f > 10 \text{ MHz}$, the distribution of the longitudinal strain is gradually reduced over the fiber cross section with the ratio r/a , giving place to a radial strain increasing with the same ratio r/a [12]. The longitudinal strain is most concentrated in the fiber core compressing and stretching the grating. The superposition of the longitudinal and radial strains causes a non-symmetric perturbation along the fiber with a period λ_{RLPG} . It is expected that the RLPG induces a very slight radial variation in the fiber cross section caused by the maximums and minimums of the resultant superposition of the strains. Fig. 8.4(b) is a simple sketch based on information in Ref. [12]. The real superposition of the radial/longitudinal strains might result in a complex strain pattern, since radial/longitudinal strains intrinsically overlap over the fiber cross section (it is illustrated in Fig. 8.4(b) as red arrows in the cladding). Fig. 8.4(c) illustrates the different power coupling interactions between the forward and backward propagating fundamental mode LP_{01} and the forward and backward propagating higher-order mode LP_{11} induced by the FBG and the RLPG. The coupling between the forward-propagating mode LP_{01} and the backward-propagating mode LP_{11} at the coupling wavelength λ_m induced by the FBG satisfies the phase-matching condition, as previously discussed in Eq. (2.22),

$$n_{01} + n_{11} = \frac{\lambda_m}{\Lambda}, \quad (8.1)$$

in which, n_{01} and n_{11} are the effective refractive indices of the LP_{01} and LP_{11} modes, respectively. Under ideal conditions the coupling between the symmetric LP_{01} mode and the spatially anti-symmetric LP_{11} mode would be expected to be negligible for a symmetric index modulation in the fiber core. However, in experimental grating structures asymmetries and modal field deformations have been observed, which could provide such coupling effects between LP_{01} and LP_{11} modes [105,106]. The modal coupling between the contra-

propagating modes, LP_{01} - LP_{01} and LP_{01} - LP_{11} , are indicated as **c1** and **c2** and illustrated as black dotted arrows in Fig. 8.4(c). On the other hand, the phase-matching condition for the coupling between the backward-propagating modes LP_{01} - LP_{11} (**c3**) at the coupling wavelength λ_m induced by the RLPG, is given as [4,5],

$$n_{01} - n_{11} = \frac{\lambda_m}{\lambda_{RLPG}}, \quad (8.2)$$

in which, λ_{RLPG} is the period of the RLPG. Eq. (8.2) satisfies also the condition for the coupling between the forward (**c4**) and backward (**c5**) propagating modes LP_{01} - LP_{11} at the Bragg wavelength λ_B induced by the RLPG. These couplings are illustrated as red dashed arrows in Fig. 8.4(c). Note in Fig. 8.4(c), if both phase-matching conditions in Eqs. (8.1) and (8.2) are simultaneously satisfied at the wavelength λ_m , the energy of the higher-order mode LP_{11} reflected by the FBG (**c2**) is coupled to the mode LP_{01} by the RLPG (**c3**) resulting in a reflected side lobe centered at λ_m . Here, the coupling between LP_{01} - LP_{11} modes is only considered. However, the principle is similar to the coupling with other higher-order modes.

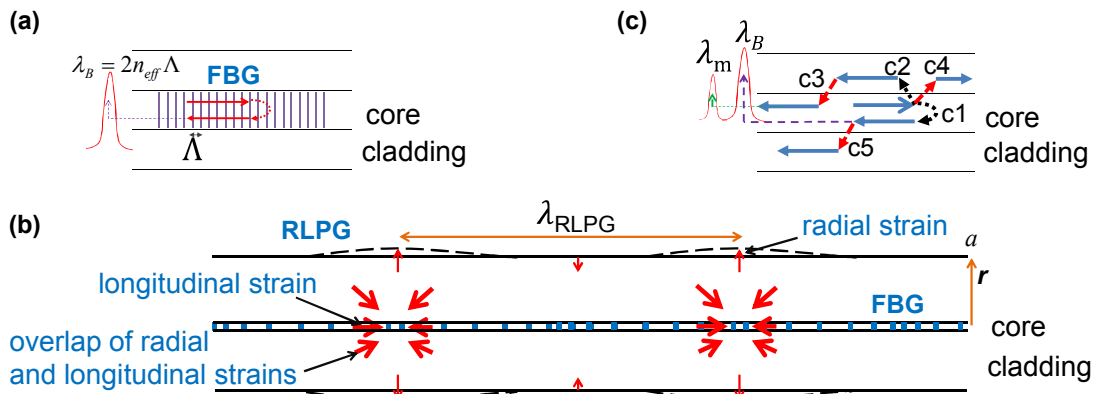


Figure 8.4: Illustration of a fiber Bragg grating (FBG) without acoustic modulation. (b) Acoustically induced radial long period grating (RLPG). (c) FBG reflectivity modulation due to the mode-couplings (cx) between LP_{01} - LP_{11} modes induced by the RLPG [107].

8.2.2 Experiment and discussion

The acousto-optic modulator is composed of a piezoelectric transducer (PZT) disc, a capillary acoustic horn and two pieces of distinct optical fibers. The acoustic horn is obtained by tapering a silica capillary with the commercial machine Vytran GPX-3200. The capillary outer/inner diameters are reduced from 1.06 / 0.81 mm to 0.18 / 0.13 mm along ~12 mm length. Later, a multimode double clad optical fiber (DCF) (fabricated at the IPHT with 125 μm cladding diameter) is inserted into the tapered capillary and fused together at the capillary tip along ~0.8 mm. The capillary and fiber are carefully aligned during the fusion

process to avoid microbends. The fusion is made by means of the commercial Vytran GPX-3400, which has additional alignment functions compared to the GPX-3200 model. Fig. 8.5(a) shows the scanned profile of the horn diameter indicating the fused region (dashed red circle). Fig. 8.5(b) shows a detail of the fused region between the capillary and the fiber. The capillary and DCF are doped with fluorine to decrease the refractive index in the cladding. It prevents the leaking and absorption of power from the core to the cladding caused by fiber bends into the capillary or along the fused region. Fig. 8.5(c) illustrates the PZT disc (0.2 mm thickness and 3 mm diameter) in yz and xy planes, which has a longitudinal acoustic resonance of ~ 10 MHz according to the manufacturer. The PZT is drilled in its center region by means of a metal driller resulting in a hole of ~ 0.5 mm in diameter, as illustrated in Fig. 8.5(c). Fig. 8.5(d) shows the DCF passing through the PZT and the horn and being spliced to a commercial single-mode optical fiber (Nufern SM-GDF-10/125). A 1 cm long FBG is inscribed in the SMF by means of a femtosecond laser and two-beam interference, using the phase mask interferometer arrangement according to the methodology described in [66]. Fig. 8.5(e) illustrates the experimental setup used to characterize the reflectivity spectrum of the FBG. The PZT basis is fixed on a metallic support connected to a signal generator (SG).

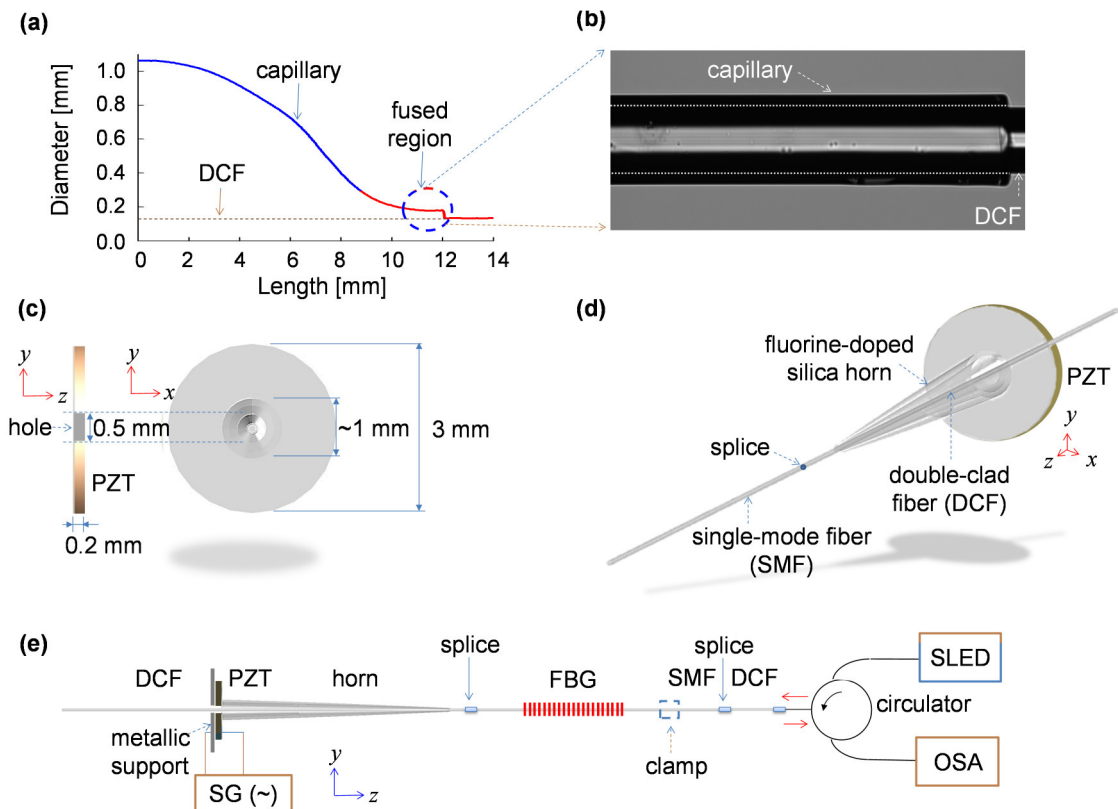


Figure 8.5: (a) Scanned profile of the horn diameter indicating the fused region (dashed red circle). (b) Detail of the fused region between the capillary and the double clad fiber (DCF). Illustrations of the (c) PZT, (d) acousto-optic modulator and (e) experimental setup used to characterize the grating spectrum [107].

The electrical connection between the PZT and the metallic support is made by using conductive glue. An electrode is also glued to the opposite PZT surface to connect the signal generator. By using this technique, the use of conventional soldering methods which cause undesired loads on the PZT is avoided. The fiber tip and the PZT basis are fixed and the modulator works as a resonant acoustic cavity exciting standing acoustic waves. The PZT is excited by a 9 V - 16 V sinusoidal signal at the resonance of $f = 10.9$ MHz. The grating is characterized by using a broadband light source (SLED), and the reflection spectrum is recorded by means of a circulator and an optical spectrum analyzer (OSA Yokogawa AQ6370C) with a 20 pm wavelength resolution. The SMF of the modulator is spliced to another DCF segment. The whole modulator is 7.5 cm long.

Fig. 8.6(a) shows the FBG spectrum without acoustic modulation (thick curve) and with acoustic modulation (thin curves) for a voltage range of 9 V - 16 V applied to the PZT at the resonance of $f = 10.9$ MHz. The non-modulated grating has the Bragg wavelength at $\lambda_B \sim 1065.3$ nm, a 3-dB bandwidth of 0.6 nm and a maximum reflectivity of $\sim 99.9\%$. The RLPG induces a side lobe with a strong peak at $\lambda_m = 1064.76$ nm, as indicated with the arrow in Fig. 8.6(a). Fig. 8.6(b) shows the variation of the side lobe reflectivity at λ_m for the considered voltage range. For voltages lower than 9 V, no relevant modulation is observed. The spectra in Fig. 8.6(a) also show a non-modulated reflection band which is caused by the high grating reflectivity and the influence of higher-order modes. Although the SMF is specified as being single-mode in the wavelength range of interest, the increase of the averaged reflective index to achieve the high reflectivity may induce multimode behavior along the grating length.

The effective indices of the fundamental mode LP_{01} ($n_{01} \sim 1.451$) and the higher-order mode LP_{11} ($n_{11} \sim 1.450$) are estimated from the Bragg wavelength λ_B and the side lobe peak λ_m , considering the period used in the grating inscription $\Lambda \sim 367$ nm and the equation $\lambda = 2n_{eff}\Lambda$. Here, we consider only the coupling between the modes LP_{01} - LP_{11} , however, the RLPG may also couple power to other higher-order modes with effective index close to $n_{11} \sim 1.45$ at adjacent wavelengths of λ_m . This effect is seen in Fig. 8.6(a) as a band of low reflectivity lobes overlapping on the shorter wavelength range. No modulated lobe is noticed on the right side of the grating spectrum indicating that the longitudinal strain in the core is too weak compared to the radial strain composing the RLPG. The frequency dependence f of the induced side lobe λ_m is not investigated because of the discrete behavior of the PZT resonances used in this study.

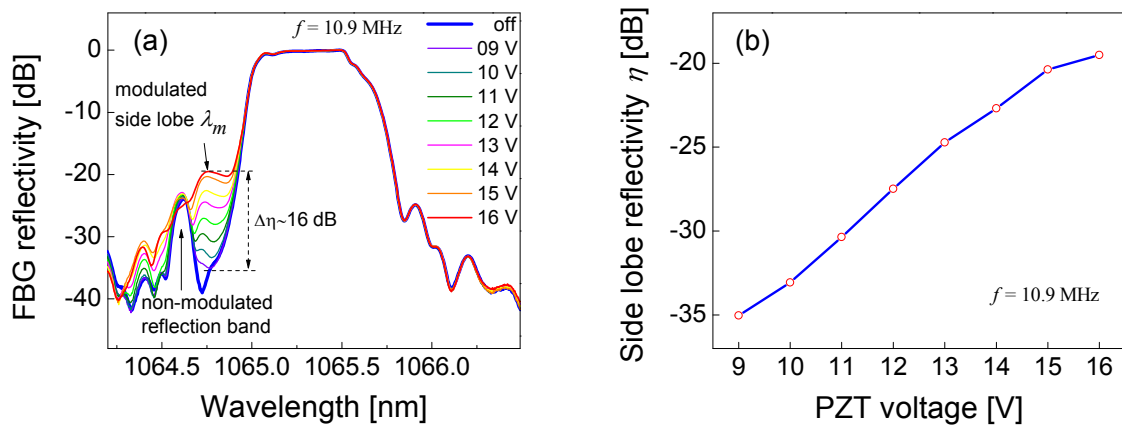


Figure 8.6: (a) FBG spectrum: without acoustic modulation (thick curve) and with acoustic modulation (thin curves) and (b) reflectivity variation of the modulated side lobe at the coupling wavelength λ_m for a 9 V - 16 V voltage range applied to the PZT at $f = 10.9$ MHz [107].

The coupling wavelength $\lambda_m = 1064.67$ nm is calculated by means of Eq. (8.1) with the modal indices n_{01} , n_{11} and the grating period Λ , which agrees well with the measured value at $\lambda_m = 1064.76$ nm. The period of the RLPG $\lambda_{LPG} \sim 1065$ μm is calculated by means of Eq. (8.2) considering the modal indices n_{01} , n_{11} , and the coupling wavelength λ_m . The RLPG period corresponds to the beat length of the modes LP_{01} - LP_{11} satisfying the phase-matching conditions in Eqs. (8.1) and (8.2) for a difference of effective indices ($n_{01} - n_{11} \sim 1 \times 10^{-3}$).

For the frequency of $f = 10.9$ MHz achieved in this experiment, the RLPG modulates a FBG at a frequency 10 times higher compared to a modulator based on flexural acoustic waves ($f \sim 1$ MHz) (considering for the calculation the same modal coupling parameters and equation $\lambda_{LPG} = [\pi a v_{ext} / f]^{1/2}$ [11]). The results show that the long period of the RLPG can couple power between modes with a very low difference of effective indices at higher frequencies. Oppositely, the increasing frequency of flexural acoustic waves considerably reduces the acoustic period, requiring a larger difference of the effective indices between the coupled modes.

A maximum side lobe reflectivity of 16 dB is achieved at the voltage of 16 V compared to the grating spectrum without modulation. The absolute side lobe reflectivity is $\sim 1\%$. An increase of the side lobe reflectivity could be obtained by the application of higher voltages to the PZT (in this study, the voltage is limited to the maximum of 16 V provided by the signal generator) or improvement of the modulator design, acoustic horn and PZT, e.g., reducing the diameter of the hole in the PZT. Moreover, the side lobe reflectivity may also be increased by the use of techniques previously discussed (e.g. cladding etched or tapered fibers, long FBGs or the used suspended-core fibers with large air holes).

In summary, acousto-optic modulation of a 1 cm long FBG at 10.9 MHz by means of an acoustically induced radial long period grating is investigated. The modulated side lobe has a reflectivity depth of 16 dB and a 3-dB bandwidth of 320 pm.

The reduction of the grating length and the modulator size indicates possibilities for compact and faster acousto-optic devices, since the acoustic wave takes a shorter time to propagate along the grating. A reduction of the grating/fiber length also prevents that low frequency acoustic noise from the environment induces instabilities in the signal output. The use of short gratings also relaxes the requirements to inscribe long gratings, which usually employs long phase masks or additional equipment to shift the grating or the laser UV beam.

The acousto-optic modulator might be used as an output coupler avoiding the heating and damage of the PZT caused by the remaining laser power transmitted through the grating and guided by the acoustic horn. In addition, the output coupler setup reduces the requirements of high reflectivity modulated side lobes, which are suitable in previous setups employing the modulator as a high reflectivity mirror in the laser cavity. It is expected that this setup can also be useful to tune the power level of the output laser by tuning the amplitude of an electrical signal applied to the PZT. Moreover, the use of standard fibers provides better mechanical stability compared to fiber taper and etching techniques.

As previously discussed in Sec. 7, an increase of the acoustic frequency f and the modulated bandwidth λ_{mFWHM} is important to shorten the pulse width of mode-locked fiber lasers. The RLPG modulates a bandwidth of $\lambda_{\text{mFWHM}} = 320$ pm indicating a broader bandwidth compared to previous studies discussed in this thesis ($\lambda_{\text{mFWHM}} = 100$ pm for the tapered fiber in Sec. 8.1.1, and $\lambda_{\text{mFWHM}} = 200$ pm for the SCF in Sec. 7.2.). It shows that the RLPG can induce a broader modulated bandwidth compared to the bandwidth induced by the longitudinal acoustic waves, since the RLPG is able to interact with many optical modes with close effective indices. In addition, the results indicate a higher modulation frequency in standard fibers compared to previous studies using flexural acoustic waves, which are limited to $f < 10$ MHz, because the acoustic wave tends to propagate on the fiber surface with the increasing frequency [11,12]. Moreover, the RLPG can couple modes with a very low difference of effective indices, which is easily obtained employing slightly multimode optical fibers. The combination of an output coupler setup with an increased frequency and bandwidth is suitable to shorten the pulse width of all-fiber mode-locked fiber lasers at the repetition rates higher than 20 MHz.

9. Conclusion - outlook

This thesis aims to investigate the interaction of acoustic waves and fiber Bragg gratings in standard and suspended-core fibers to increase the acousto-optic interaction, bandwidth and frequency. Devices operating in the frequency range from $f=200$ kHz to $f=13$ MHz are investigated to evaluate the influence of the fiber, grating and modulator design on the reflectivity modulation. The work intends to provide useful information to the design and assembly of acousto-optic devices for future applications in low frequency dynamic filters, CW and Q-switched fiber lasers ($f < 1$ MHz), and high repetition rate mode-locked fiber lasers ($f > 5$ MHz).

Initially, modulators operating at frequencies lower than $f=1.2$ MHz are investigated. In this frequency range, the frequency effect is not so relevant on the modulation efficiency, and the devices can be easily assembled by employing relatively large piezoelectric transducers (PZTs), which consequently can generate stronger acoustic waves. These devices are usually employed to modulate the reflectivity/bandwidth of the Bragg wavelength at frequencies lower than $f=600$ kHz and to induce distinguished side lobes at higher frequencies. The modulation of FBGs at this frequency range finds application in optical filters, gain equalizers, dispersion compensators and Q-switched fiber lasers.

A numerical method based on the 3D - finite element method is proposed to simulate an acousto-optic device considering a PZT and its anisotropy. The main purpose is the characterization of the PZT acoustic modes and their influence to generate acoustic waves. In particular, the study intends to evaluate the most relevant modes and resonances to excite longitudinal acoustic waves in a fiber in the considered low frequency range. In addition, experiments are performed to verify the accuracy of the simulations. A good agreement between the experimental-simulation results indicates the grating modulation takes place only at specific frequencies, which depend on the material and geometry of the PZT, acoustic horn and optical fiber. The numerical method including the PZT allows a more accurate simulation of the modulator and can assist the design of novel acousto-optic devices, since the PZT modes strongly influence on the grating modulation.

The interaction of longitudinal acoustic waves and FBGs in suspended-core fibers is numerically investigated to increase the overlap of the acoustic power and the grating in the core. The fiber core and the air hole size are increased and the strain and grating properties are

simulated by means of the finite element method and the transfer matrix method, respectively. The results show that the side lobe reflectivity increases with larger fiber cores because the increased overlap of the guided mode with the grating. However, a larger core size increases the number of supported optical modes by the fiber. On the other hand, SCFs with large air holes cause a significant reduction of the amount of silica in the fiber cross section, increasing the interaction between the acoustic wave and the grating in the core. An increased modulation efficiency of 66% compared to a SMF is obtained, which is equivalent in reducing the grating modulation index or length in as much as 75%. The results indicate new possibilities to increase the acousto-optic modulation in fibers without reducing the fiber diameter, which makes the devices more stable compared to tapering and etching techniques.

A considerable modulation of the reflectivity of FBGs inscribed in two distinct SCFs indicates experimental evidences of the increased interaction at the low frequency range. A reflectivity modulation depth of 67% is obtained for a grating inscribed in a four holes SCF. The results indicate a reduction of the grating length and the power applied to the PZT (16x lower) compared to devices employing SMFs in previous studies. In addition, the modulation of the group delay is also investigated. The grating bandwidth is increased and the spectrum envelope is adjusted to an almost Gaussian shape. Linear responses of the group delay and dispersion are obtained over a wavelength range larger than 0.7 nm.

The second SCF investigated is a high birefringence double-core suspended-core fiber (HB-SCF). A reflectivity modulation depth of 84% is achieved by increasing the air holes compared to the four holes SCF previously discussed. In addition, the acoustically induced power coupling between the orthogonal modes supported by the fiber indicates a new possibility of a multi-wavelength dynamic filter for WDM communication systems and fiber lasers. In summary, the SCFs point to a higher acousto-optic modulation compared to solid SMFs, being useful to reduce the fiber/grating length, the size and the acoustic power of the modulator.

A method to acoustically induce a dynamic phase-shift in a chirped fiber Bragg grating is experimentally demonstrated. The modulator design is also optimized by reducing the size of the PZT, of the acoustic horn and the optical fiber. The strain peak caused by the acoustic wave induces a dynamic variation of the grating period (phase-shift) decreasing the grating reflectivity at specific wavelengths. A notch depth of 32 dB is achieved, showing a considerable rejection efficiency compared to previous studies. In addition, two notches are induced in the grating spectrum by increasing the frequency, which is suitable for multi-

wavelength dynamic filters. It is expected that an increasing frequency can induce more notches in the grating spectrum, which might be limited by the grating bandwidth and the reduction of the acoustic amplitude.

A combination of a SCF with three air holes and an optimized modulator design allowed an increase of the modulation frequency up to $f = 5$ MHz for application in a mode-locked ytterbium-doped fiber laser. The laser emitted pulses with a pulse width shorter than ~ 550 ps at a repetition rate of 10.2 MHz. The results indicate that short gratings can be useful to increase the modulated bandwidth and to shorten the pulse width. However, the splice between SCF-SMF inserts considerable losses in the laser cavity reducing the overall laser efficiency. It may be solved by reducing the splice loss using transition tapered fibers. The use of SCFs in the whole laser cavity might also reduce the insertion loss, while compensating the cavity dispersion, which is also important to reduce the pulse width.

An increase of the modulation depth, bandwidth and acoustic frequency f are important parameters of an acousto-optic modulator to shorten the pulse width of mode-locked fiber lasers. However, a reduction of the PZT thickness to increase the frequency attenuates its deformations and, consequently, the acousto-optic interaction. In addition, a reduction of the PZT requires the use of small acoustic components to avoid loads and amplify the acoustic wave, which are challenge and difficult to manipulate. To overcome these drawbacks, two distinct approaches of modulators operating at 1065 nm wavelength range are investigated to increase the acousto-optic interaction, bandwidth and frequency.

The first modulator is based on a high reflectivity grating inscribed in a tapered optical fiber. A side lobe reflectivity saturation is achieved at the resonance of $f = 5.1$ MHz. The modulator also exhibits high modulation frequencies ($f = 10.8$ MHz and $f = 13$ MHz), which is suitable to shorten the pulse width at the repetition rates higher than 26 MHz. The use of short gratings also indicates a broader bandwidth (100 pm) compared to previous studies with standard fibers (3.6 pm [14]). In addition, a technique to couple the acoustic wave on the side of the optical fiber avoids the heating caused by the remaining transmitted power through the grating/acoustic horn, which can damage the PZT and limit the pump and the output laser power. However, a DC wavelength shift has been noticed with the increasing voltage, which might be caused by a rearrangement of the grating structure defined during the inscription process.

For the second modulator, a new acousto-optic interaction based on an acoustically induced radial long period grating (RLPG) and a FBG at 10.9 MHz is investigated. The

modulated band has a bandwidth of 320 pm, which is broader compared to the previous results discussed in this thesis. It indicates that the multimode coupling induced by the RLPG can modulate a broader bandwidth compared to bandwidth induced by the longitudinal acoustic waves. The use of standard fibers can also reduce the losses in the laser cavity, which is suitable to increase the laser efficiency and provide a better mechanical stability compared to fiber taper and etching techniques (no DC wavelength shift is noticed for this modulator). The output coupler setup relaxes the requirements of a high modulated reflectivity avoiding also the heating and damage of the PZT. In addition, the device indicates a higher modulation frequency compared to previous studies using flexural acoustic waves, which is useful to shorten the pulse width at the repetition rates higher than 20 MHz.

In summary, acousto-optic modulation of fiber Bragg gratings in standard and suspended-core fibers is investigated. The study aims to increase the modulation efficiency, the bandwidth and the acoustic frequency. The results indicate that the acousto-optic interaction can be increased by using a combination of high reflectivity gratings in suspended-core fibers or tapered fibers, and by reducing and optimizing the modulator design. The reduction of the fiber/grating length increases the modulated bandwidth and reduces the modulator size, which is suitable for compact and faster acousto-optic devices. Consequently, the increased interaction efficiency, bandwidth and frequency might be useful to shorten the pulse width of future mode-locked all-fiber lasers.

Bibliography

- [1] B. Y. Kim, J. N. Blake, H. E. Engan, and H. J. Shaw, "All-fiber acousto-optic frequency shifter," *Opt. Lett.* **11**, 389 (1986)
- [2] D.-R. Song, H. S. Park, B. Y. Kim, and K. Y. Song, "Acoustooptic generation and characterization of the higher order modes in a four-mode fiber for mode-division multiplexed transmission," *J. Light. Technol.* **32**, 4534–4538 (2014)
- [3] H. S. Kim, S. H. Yun, I. K. Kwang, and B. Y. Kim, "All-fiber acousto-optic tunable notch filter with electronically controllable spectral profile.," *Opt. Lett.* **22**, 1476–8 (1997)
- [4] W. F. Liu, I. M. Liu, L. W. Chung, D. W. Huang, and C. C. Yang, "Acoustic-induced switching of the reflection wavelength in a fiber Bragg grating," *Opt. Lett.* **25**, 1319 (2000)
- [5] N. H. Sun, C. C. Chou, M. Chang, C. N. Lin, C. C. Yang, Y.-W. Kiang, and W.-F. Liu, "Analysis of phase-matching conditions in flexural-wave modulated fiber Bragg grating," *J. Light. Technol.* **20**, 311–315 (2002)
- [6] W. F. Liu, P. S. J. Russell, and L. Dong, "100% efficient narrow-band acoustooptic tunable reflector using fiber Bragg grating," *J. Light. Technol.* **16**, 2006–2009 (1998)
- [7] P. S. J. Russell and W.-F. Liu, "Acousto-optic superlattice modulation in fiber Bragg gratings," *J. Opt. Soc. Am. A* **17**, 1421 (2000)
- [8] W. F. Liu, P. S. Russell, and L. Dong, "Acousto-optic superlattice modulator using a fiber Bragg grating," *Opt. Lett.* **22**, 1515–7 (1997)
- [9] C. A. F. Marques, R. A. Oliveira, A. A. P. Pohl, and R. N. Nogueira, "Tunability of the FBG group delay through acousto-optic modulation," *Opt. Fiber Technol.* **19**, 121–125 (2013)
- [10] R. E. Silva, T. Tiess, M. Becker, T. Eschrich, M. Rothhardt, M. Jäger, A. A. P. Pohl, and H. Bartelt, "Acousto-optic modulation of a fiber Bragg grating in suspended core fiber for mode-locked all-fiber lasers," *Laser Phys. Lett.* **12**, 045101 (2015)
- [11] J. N. Blake, B. Y. Kim, H. E. Engan, and H. J. Shaw, "Analysis of intermodal coupling in a two-mode fiber with periodic microbends," *Opt. Lett.* **12**, 281 (1987)
- [12] H. E. Engan, B. Y. Kim, J. N. Blake, and H. J. Shaw, "Propagation and optical interaction of guided acoustic waves in two-mode optical fibers," *J. Light. Technol.* **6**, 428–436 (1988)

- [13] C. Cuadrado-Laborde, A. Díez, M. Delgado-Pinar, J. L. Cruz, and M. V. Andrés, "Mode locking of an all-fiber laser by acousto-optic superlattice modulation," *Opt. Lett.* **34**, 1111 (2009)
- [14] I. L. Villegas, C. Cuadrado-Laborde, J. Abreu-Afonso, A. Díez, J. L. Cruz, M. A. Martínez-Gámez, and M. V. Andrés, "Mode-locked Yb-doped all-fiber laser based on in-fiber acoustooptic modulation," *Laser Phys. Lett.* **8**, 227–231 (2011)
- [15] C. Cuadrado-Laborde, A. Díez, J. L. Cruz, and M. V. Andrés, "Experimental study of an all-fiber laser actively mode-locked by standing-wave acousto-optic modulation," *Appl. Phys. B* **99**, 95–99 (2009)
- [16] G. Canat, S. Jetschke, S. Unger, L. Lombard, P. Bourdon, J. Kirchhof, V. Jolivet, A. Dolfi, and O. Vasseur, "Multifilament-core fibers for high energy pulse amplification at 15 μm with excellent beam quality," *Opt. Lett.* **33**, 2701 (2008)
- [17] A. Ancona, D. Nodop, J. Limpert, S. Nolte, and A. Tünnermann, "Microdrilling of metals with an inexpensive and compact ultra-short-pulse fiber amplified microchip laser," *Appl. Phys. A* **94**, 19–24 (2008)
- [18] Y. Yu, L. Lui, H. Tam, and W. Chung, "Fiber-laser-based wavelength-division multiplexed fiber Bragg grating sensor system," *IEEE Photonics Technol. Lett.* **13**, 702–704 (2001)
- [19] C. Hönninger, M. Plötner, B. Ortac, R. Ackermann, R. Kammel, J. Limpert, S. Nolte, and A. Tünnermann, "Femtosecond fiber laser system for medical applications," in *Proceedings of SPIE* (SPIE, 2009), Vol. 7203, p. 72030W–6
- [20] H. H. Kee, G. P. Lees, and T. P. Newson, "Narrow linewidth CW and Q-switched erbium-doped fibre loop laser," *Electron. Lett.* **34**, 1318 (1998)
- [21] J. A. Alvarez-Chavez, H. L. Offerhaus, J. Nilsson, P. W. Turner, W. A. Clarkson, and D. J. Richardson, "High-energy, high-power ytterbium-doped Q-switched fiber laser," *Opt. Lett.* **25**, 37 (2000)
- [22] I. L. Villegas, C. Cuadrado-Laborde, a. Díez, J. L. Cruz, M. a. Martínez-Gámez, and M. V. Andrés, "Yb-doped strictly all-fiber laser actively Q-switched by intermodal acousto-optic modulation," *Laser Phys.* **21**, 1650–1655 (2011)
- [23] D. Zalvidea, N. A. Russo, R. Duchowicz, M. Delgado-Pinar, A. Díez, J. L. Cruz, and M. V. Andrés, "High-repetition rate acoustic-induced Q-switched all-fiber laser," *Opt. Commun.* **244**, 315–319 (2005)
- [24] M. Delgado-Pinar, D. Zalvidea, a Díez, P. Perez-Millan, and M. Andres, "Q-switching of an all-fiber laser by acousto-optic modulation of a fiber Bragg grating.," *Opt. Express* **14**, 1106–12 (2006)
- [25] K. O. Hill and G. Meltz, "Fiber Bragg Grating Technology Fundamentals and Overview," **15**, 1263–1276 (1997)

- [26] B. E. A. Saleh and M. C. Teich, "Fundamentals of Photonics: Second Edition," John Wiley Son, Hoboken, NJ, USA (2007)
- [27] D. Gloge, "Weakly Guiding Fibers," *Appl. Opt.* **10**, 2252 (1971)
- [28] Katsunari Okamoto, *Fundamentals of Optical Waveguides*, 2nd ed. (Academic Press, 2006)
- [29] K. Saitoh and M. Koshiba, "Numerical modeling of photonic crystal fibers," *J. Light. Technol.* **23**, 3580–3590 (2005)
- [30] M. A. R. Franco, V. A. Serrao, and F. Sircilli, "Microstructured optical fiber for residual dispersion compensation over S + C + L + U wavelength bands," *IEEE Photonics Technol. Lett.* **20**, 751–753 (2008)
- [31] G. Chesini, V. A. Serrão, M. A. R. Franco, and C. M. B. Cordeiro, "Analysis and optimization of an all-fiber device based on photonic crystal fiber with integrated electrodes," *Opt. Express* **18**, 2842 (2010)
- [32] R. E. Silva, R. A. Oliveira, M. A. R. Franco, and A. A. P. Pohl, "Influência da Microestrutura em Propriedades Acusto-ópticas de Fibra de Cristal Fotônico," in *Simpósio Brasileiro de Telecomunicações. SBrT 11* (2011), pp. 2–5
- [33] Y. A. V. Espinel, M. A. R. Franco, and C. M. B. Cordeiro, "Tunable single-polarization single-mode microstructured polymer optical fiber," *J. Light. Technol.* **29**, 2372–2378 (2011)
- [34] C. M. Jewart, T. Chen, E. Lindner, J. Fiebrandt, M. Rothhardt, K. Schuster, J. Kobelke, H. Bartelt, and K. P. Chen, "Suspended-core fiber Bragg grating sensor for directional-dependent transverse stress monitoring," *Opt. Lett.* **36**, 2360 (2011)
- [35] K. Saitoh and M. Koshiba, "Full-vectorial imaginary-distance beam propagation method based on a finite element scheme: application to photonic crystal fibers," *IEEE J. Quantum Electron.* **38**, 927–933 (2002)
- [36] A. Cucinotta, S. Selleri, L. Vincetti, and M. Zoboli, "Holey fiber analysis through the finite-element method," *IEEE Photonics Technol. Lett.* **14**, 1530–1532 (2002)
- [37] M. Koshiba, *Optical Waveguide Theory by the Finite Element Method* (KTK Scientific, 1993)
- [38] K. O. K. Hill, Y. Fujii, D. C. Johnson, and B. S. Kawasaki, "Photosensitivity in optical fiber waveguides: Application to reflection filter fabrication," *Appl. Phys.* **32**, 647 (1978)
- [39] G. Meltz, W. W. Morey, and W. H. Glenn, "Formation of Bragg gratings in optical fibers by a transverse holographic method.," *Opt. Lett.* **14**, 823–5 (1989)
- [40] T. Erdogan, "Fiber grating spectra," *Light. Technol. J.* **15**, 1277–1294 (1997)

- [41] R. Kashyap, *Fiber Bragg Gratings* (Academic Press, 1999)
- [42] G. Meltz and W. W. Morey, "Bragg grating formation and germanosilicate fiber photosensitivity," *Soc. Photo-Optical Instrum. Eng. Conf. Ser.* **1516**, 185–199 (1991)
- [43] A. Othonos, "Fiber bragg gratings," *Am. Inst. Phys.* 4309–4341 (1997)
- [44] A. Yariv, "Coupled-mode theory for guided-wave optics," *IEEE J. Quantum Electron.* **9**, 919–933 (1973)
- [45] A. A. P. Pohl, R. A. Oliveira, R. E. Silva, C. A. F. Marques, P. de T. Neves, K. Cook, J. Canning, and R. N. Nogueira, "Advances and new applications using the acousto-optic effect in optical fibers," *Photonic Sensors* **3**, 1–25 (2013)
- [46] K. O. Hill and G. Meltz, "Fiber Bragg grating technology fundamentals and overview," *J. Light. Technol.* **15**, 1263–1276 (1997)
- [47] J. H. Lee, Y. M. Chang, Y.-G. Han, S.-H. Kim, H. Chung, and S. B. Lee, "Wavelength and repetition rate tunable optical pulse source using a chirped fiber Bragg grating and a nonlinear optical loop mirror," *IEEE Photonics Technol. Lett.* **17**, 34–36 (2005)
- [48] I. C. M. Littler, M. Rochette, and B. J. Eggleton, "Adjustable bandwidth dispersionless bandpass FBG optical filter," *Opt. Express* **13**, 3397 (2005)
- [49] B. Dabarsyah, C. S. Goh, S. K. Khijwania, S. Y. Set, K. Katoh, and K. Kikuchi, "Adjustable group velocity dispersion and dispersion slope compensation devices with wavelength tunability based on enhanced thermal chirping of fiber bragg gratings," *J. Light. Technol.* **25**, 2711–2718 (2007)
- [50] J. Kim, J. Bae, Y. G. Han, S. H. Kim, J. M. Jeong, and S. B. Lee, "Effectively tunable dispersion compensation based on chirped fiber Bragg gratings without central wavelength shift," *IEEE Photonics Technol. Lett.* **16**, 849–851 (2004)
- [51] C. S. Goh, S. Y. Set, and K. Kikuchi, "Design and fabrication of a tunable dispersion-slope compensating module based on strain-chirped fiber Bragg gratings," *IEEE Photonics Technol. Lett.* **16**, 524–526 (2004)
- [52] A. A. P. Pohl, K. Cook, and J. Canning, "Acoustic-induced modulation of photonic crystal fiber Bragg gratings," *2008 10th Anniv. Int. Conf. Transparent Opt. Networks* 51–54 (2008)
- [53] R. A. Oliveira, P. T. Neves, J. T. Pereira, and A. A. P. Pohl, "Numerical approach for designing a Bragg grating acousto-optic modulator using the finite element and the transfer matrix methods," *Opt. Commun.* **281**, 4899–4905 (2008)
- [54] A. A. P. Pohl, R. E. Silva, M. A. R. Franco, P. de T. Neves, and H. Bartelt, "Modelling the bandwidth behaviour of fibre Bragg gratings excited by low-frequency acoustic waves," in *2013 15th International Conference on Transparent Optical Networks (ICTON)* (IEEE, 2013), pp. 1–4

- [55] S. H. Yun, I. K. Hwang, and B. Y. Kim, "All-fiber tunable filter and laser based on two-mode fiber.," *Opt. Lett.* **21**, 27–9 (1996)
- [56] R. A. Oliveira, P. T. Neves Jr., J. T. Pereira, J. Canning, and A. A. P. Pohl, "Vibration mode analysis of a silica horn–fiber Bragg grating device," *Opt. Commun.* **283**, 1296–1302 (2010)
- [57] A. H. Meitzler, H. M. O’Bryan, and H. F. Tiersten, "Definition and measurement of radial mode coupling factors in piezoelectric ceramic materials with large variations in poisson’s ratio," *IEEE Trans. Sonics Ultrason.* **20**, 233–239 (1973)
- [58] A. Std, *IEEE Standard on Piezoelectricity* (1988), p. 79638
- [59] M. Brissaud, "Characterization of piezoceramics.," *IEEE Trans. Ultrason. Ferroelectr. Freq. Control* **38**, 603–17 (1991)
- [60] K. Van Dyke, "The piezo-electric resonator and its equivalent network," *Proc. Inst. Radio Eng.* (1928)
- [61] A. Ballato, "Modeling piezoelectric and piezomagnetic devices and structures via equivalent networks.," *IEEE Trans. Ultrason. Ferroelectr. Freq. Control* **48**, 1189–240 (2001)
- [62] H. Jaffe and D. A. Berlincourt, "Piezoelectric transducer materials," *Proc. IEEE* **53**, 1372–1386 (1965)
- [63] Ferroperm piezoceramics, "Full data matrix," <http://app04.swwwing.net/swwwing/app/cm/Browse.jsp?PAGE=1417>
- [64] R. E. Silva, M. A. R. Franco, H. Bartelt, and A. A. P. Pohl, "Numerical characterization of piezoelectric resonant transducer modes for acoustic wave excitation in optical fibers," *Meas. Sci. Technol.* **24**, 094020 (2013)
- [65] R. E. Silva, M. A. R. Franco, P. T. Neves, H. Bartelt, and A. A. P. Pohl, "Detailed analysis of the longitudinal acousto-optical resonances in a fiber Bragg modulator.," *Opt. Express* **21**, 6997–7007 (2013)
- [66] M. Becker, J. Bergmann, S. Brückner, M. Franke, E. Lindner, M. W. Rothhardt, and H. Bartelt, "Fiber Bragg grating inscription combining DUV sub-picosecond laser pulses and two-beam interferometry," *Opt. Express* **16**, 19169 (2008)
- [67] A. Hartung, S. Brueckner, and H. Bartelt, "Limits of light guidance in optical nanofibers," *Opt. Express* **18**, 3754 (2010)
- [68] M. C. Phan Huy, G. Laffont, V. Dewynter, P. Ferdinand, P. Roy, J.-L. Auguste, D. Pagnoux, W. Blanc, and B. Dussardier, "Three-hole microstructured optical fiber for efficient fiber Bragg grating refractometer," *Opt. Lett.* **32**, 2390 (2007)
- [69] S. Afshar V., S. C. Warren-Smith, and T. M. Monro, "Enhancement of fluorescence-based sensing using microstructured optical fibres," *Opt. Express* **15**, 17891 (2007)

- [70] L. Fu, B. K. Thomas, and L. Dong, "Efficient supercontinuum generations in silica suspended core fibers," *Opt. Express* **16**, 19629 (2008)
- [71] A. Hartung, A. M. Heidt, and H. Bartelt, "Pulse-preserving broadband visible supercontinuum generation in all-normal dispersion tapered suspended-core optical fibers," *Opt. Express* **19**, 12275 (2011)
- [72] C. M. Jewart, T. Chen, E. Lindner, J. Fiebrandt, M. Rothhardt, K. Schuster, J. Kobelke, H. Bartelt, and K. P. Chen, "Bending insensitivity of fiber Bragg gratings in suspended-core optical fibers.," *Opt. Lett.* **36**, 4491–3 (2011)
- [73] P. T. Neves Jr. and A. A. P. Pohl, "Time analysis of the wavelength shift in fiber Bragg gratings," *J. Light. Technol.* **25**, 3580–3588 (2007)
- [74] R. E. Silva, A. Hartung, M. Rothhardt, A. A. P. Pohl, and H. Bartelt, "Detailed numerical investigation of the interaction of longitudinal acoustic waves with fiber Bragg gratings in suspended-core fibers," *Opt. Commun.* **344**, 43–50 (2015)
- [75] T. A. T. Birks, P. S. J. Russell, and D. O. Culverhouse, "The acousto-optic effect in single-mode fiber tapers and couplers," *J. Light. Technol.* **14**, 2519–2529 (1996)
- [76] M. Becker, L. Fernandes, M. Rothhardt, S. Bruckner, K. Schuster, J. Kobelke, O. Frazao, H. Bartelt, and P. Marques, "Inscription of fiber Bragg grating arrays in pure silica suspended core fibers," *IEEE Photonics Technol. Lett.* **21**, 1453–1455 (2009)
- [77] Y. Wang, H. Bartelt, S. Brueckner, J. Kobelke, M. Rothhardt, K. Mörl, W. Ecke, and R. Willsch, "Splicing Ge-doped photonic crystal fibers using commercial fusion splicer with default discharge parameters," *Opt. Express* **16**, 7258 (2008)
- [78] C. R. Giles, "Lightwave applications of fiber Bragg gratings," *J. Light. Technol.* **15**, 1391–1404 (1997)
- [79] R. E. Silva, M. Becker, A. Hartung, M. Rothhardt, A. A. P. Pohl, and H. Bartelt, "Reflectivity and bandwidth modulation of fiber Bragg gratings in a suspended core fiber by tunable acoustic waves," *IEEE Photonics J.* **6**, 1–8 (2014)
- [80] R. Leners, P. L. François, and G. Stéphan, "Simultaneous effects of gain and loss anisotropies on the thresholds of a bipolarization fiber laser," *Opt. Lett.* **19**, 275 (1994)
- [81] J. Hernandez-Cordero, V. A. Kozlov, A. L. G. Carter, and T. F. Morse, "Fiber laser polarization tuning using a Bragg grating in a Hi-Bi fiber," *IEEE Photonics Technol. Lett.* **10**, 941–943 (1998)
- [82] Y. Liu, X. Feng, S. Yuan, G. Kai, and X. Dong, "Simultaneous four-wavelength lasing oscillations in an erbium-doped fiber laser with two high birefringence fiber Bragg gratings," *Opt. Express* **12**, 2056 (2004)
- [83] D. S. Moon, U.-C. Paek, and Y. Chung, "Polarization controlled multi-wavelength Er-doped fiber laser using fiber Bragg grating written in few-mode side-hole fiber with an elliptical core," *Opt. Express* **13**, 5574 (2005)

- [84] D.-W. Huang, W. F. Liu, and C. C. Yang, "Q -Switched all-fiber laser with an acoustically modulated fiber attenuator," *IEEE Photonics Technol. Lett.* **12**, 1153–1155 (2000)
- [85] C. A. F. Marques, R. A. Oliveira, A. A. P. Pohl, and R. N. Nogueira, "Adjustable EDFA gain equalization filter for DWDM channels based on a single LPG excited by flexural acoustic waves," *Opt. Commun.* **285**, 3770–3774 (2012)
- [86] A. M. Vengsarkar, P. J. Lemaire, J. B. Judkins, V. Bhatia, T. Erdogan, and J. E. Sipe, "Long-period fiber gratings as band-rejection filters," *J. Light. Technol.* **14**, 58–65 (1996)
- [87] S. Savin, M. J. F. Digonnet, G. S. Kino, and H. J. Shaw, "Tunable mechanically induced long-period fiber gratings," *Opt. Lett.* **25**, 710 (2000)
- [88] A. Candiani, W. Margulis, C. Sterner, M. Konstantaki, and S. Pissadakis, "Phase-shifted Bragg microstructured optical fiber gratings utilizing infiltrated ferrofluids.," *Opt. Lett.* **36**, 2548–50 (2011)
- [89] M. M. N. Hamarsheh, A. A. S. Falah, and M. R. Mokhtar, "Tunable fiber Bragg grating phase shift by simple pressure packaging," *Opt. Eng.* **54**, 016105 (2015)
- [90] N. Q. Ngo, S. Y. Li, L. N. Binh, and S. C. Tjin, "A phase-shifted linearly chirped fiber Bragg grating with tunable bandwidth," *Opt. Commun.* **260**, 438–441 (2006)
- [91] M. Becker, T. Elsmann, I. Latka, M. Rothhardt, and H. Bartelt, "Chirped phase mask interferometer for fiber bragg grating array inscription," *J. Light. Technol.* **PP**, 1–1 (2015)
- [92] E. Snitzer, "Proposed fiber cavities for optical masers," *J. Appl. Phys.* **32**, 36 (1961)
- [93] S. B. Poole, D. N. Payne, and M. E. Fermann, "Fabrication of low-loss optical fibres containing rare-earth ions," *Electron. Lett.* **21**, 737 (1985)
- [94] R. J. Mears, L. Reekie, S. B. Poole, and D. N. Payne, "Low-threshold tunable CW and Q-switched fibre laser operating at 1.55 μm ," *Electron. Lett.* **22**, 159 (1986)
- [95] F. Just, H.-R. Müller, S. Unger, J. Kirchhof, V. Reichel, and H. Bartelt, "Ytterbium-doping related stresses in preforms for high-power fiber lasers," *J. Light. Technol.* **27**, 2111–2116 (2009)
- [96] F. Mahmoud, H.-R. Müller, K. Mörl, and H. Bartelt, "Scattering loss in Nd-doped silica based optical fibers," *Opt. - Int. J. Light Electron Opt.* **113**, 421–424 (2002)
- [97] F. Just, S. Unger, J. Kirchhof, V. Reichel, and H. Bartelt, "Thermal stress anomaly in rare-earth-doped fiber materials for high-power fiber lasers codoped with aluminum and phosphorus," in *Society of Photo-Optical Instrumentation Engineers (SPIE) Conference Series* (2010), Vol. 7721, pp. 772106–772106–8

- [98] M. Becker, S. Brückner, M. Leich, E. Lindner, M. Rothhardt, S. Unger, S. Jetschke, and H. Bartelt, "Towards a monolithic fiber laser with deep UV femtosecond-induced fiber Bragg gratings," *Opt. Commun.* **284**, 5770–5773 (2011)
- [99] J. Limpert, F. Roser, D. N. D. N. Schimpf, E. Seise, T. Eidam, S. Hadrich, J. Rothhardt, C. J. Misas, A. Tunnermann, R. Fabian, and H. Steffen, "High repetition rate gigawatt peak power fiber laser systems : challenges , design , and experiment," *IEEE J. Sel. Top. Quantum Electron.* **15**, 159–169 (2009)
- [100] Y. Li, C. Lou, M. Han, and Y. Gao, "Detuning characteristics of the AM mode-locked fiber laser," *Opt. Quantum Electron.* **33**, 589–597 (2001)
- [101] R. Paschotta, J. Nilsson, A. C. Tropper, and D. C. Hanna, "Ytterbium-doped fiber amplifiers," *IEEE J. Quantum Electron.* **33**, 1049–1056 (1997)
- [102] X. Wang, C. Ehlers, and M. Neitzel, "Electro-mechanical dynamic analysis of the piezoelectric stack," *Smart Mater. Struct.* **5**, 492–500 (1996)
- [103] A. Chamorovskiy, Y. Chamorovskiy, I. Vorob'ev, and O. G. Okhotnikov, "95-Femtosecond Suspended Core Ytterbium Fiber Laser," *IEEE Photonics Technol. Lett.* **22**, 1321–1323 (2010)
- [104] R. M. André, S. O. Silva, M. Becker, K. Schuster, M. Rothardt, H. Bartelt, M. B. Marques, and O. Frazão, "Strain sensitivity enhancement in suspended core fiber tapers," *Photonic Sensors* **3**, 118–123 (2012)
- [105] C. A. Véron, "Asymmetric effects in UV-induced long-period fiber gratings," in *Bragg Gratings, Photosensitivity, and Poling in Glass Waveguides* (Optical Society of America, 2001), p. BThC17.
- [106] H. Renner, D. Johlen, and E. Brinkmeyer, "Modal Field Deformation and Transition Losses in UV Side-Written Optical Fibers," *Appl. Opt.* **39**, 933 (2000)
- [107] R. E. Silva, T. Tiess, M. Becker, T. Eschrich, M. Rothhardt, M. Jäger, A. A. P. Pohl and H. Bartelt, "All-fiber 10 MHz acousto-optic modulator of a fiber Bragg grating at 1060 nm wavelength," *Opt. Express* **20**, 25972-25978 (2015)

List of publications

Peer review journals

R. E. Silva, T. Tiess, M. Becker, T. Eschrich, M. Rothhardt, M. Jäger, A. A. P. Pohl, and H. Bartelt, "Acousto-optic modulation of a fiber Bragg grating in suspended-core fiber for mode-locked all-fiber lasers," *Laser Phys. Lett.* **12**, 045101 (2015).

R. E. Silva, A. Hartung, M. Rothhardt, A. A. P. Pohl, and H. Bartelt, "Detailed numerical investigation of the interaction of longitudinal acoustic waves with fiber Bragg gratings in suspended-core fibers," *Opt. Commun.* **344**, 43–50 (2015).

R. E. Silva, M. Becker, A. Hartung, M. Rothhardt, A. A. P. Pohl, and H. Bartelt, "Reflectivity and bandwidth modulation of fiber Bragg gratings in a suspended-core fiber by tunable acoustic waves," *IEEE Photonics J.* **6**, 1–8 (2014).

R. E. Silva, M. A. R. Franco, H. Bartelt, and A. A. P. Pohl, "Numerical characterization of piezoelectric resonant transducer modes for acoustic wave excitation in optical fibers," *Meas. Sci. Technol.* **24** 094020 (2013).

R. E. Silva, M. A. R. Franco, P. T. Neves, H. Bartelt, and A. A. P. Pohl, "Detailed analysis of the longitudinal acousto-optical resonances in a fiber Bragg modulator.," *Opt. Express* **21** 6997–7007 (2013).

R. E. Silva and A. A. P. Pohl, "Characterization of flexural acoustic waves in optical fibers using an extrinsic Fabry–Perot interferometer," *Meas. Sci. Technol.* **23** 055206 (2012).

A. A. P. Pohl, R. A. Oliveira, R. E. Silva, C. A. F. Marques, P. de T. Neves, K. Cook, J. Canning, and R. N. Nogueira, "Advances and new applications using the acousto-optic effect in optical fibers," *Photonic Sensors* **3** 1–25 (2013).

R. E. Silva, T. Tiess, M. Becker, T. Eschrich, M. Rothhardt, M. Jäger, A. A. P. Pohl, and H. Bartelt, "All-fiber 10 MHz acousto-optic modulator of a fiber Bragg grating at 1060 nm wavelength," *Opt. Express* **20**, 25972-25978 (2015).

Conference contributions

R. E. Silva, T. Tiess, M. Becker, T. Eschrich, M. Rothhardt, M. Jäger, A. A. P. Pohl, and H. Bartelt, "All-fiber laser mode-locked by the acousto-optic modulation of a fiber Bragg grating in suspended-core fiber", in 24th International Conference on Optical Fiber Sensor (OFS 24), Curitiba/Brazil, 2015.

R. E. Silva, M. Becker, M. Rothhardt, A. A. P. Pohl and H. Bartelt, "Wideband notch filter acoustically induced in a chirped fiber bragg grating", in International Microwave and Optoelectronics Conference (2015), Porto de Galinhas/Brazil, 2015.

R. E. Silva, M. Becker, M. Rothhardt, A. A. P. Pohl and H. Bartelt, "Acoustically induced increase of Bragg grating bandwidth in four holes suspended-core fiber", in Bragg Gratings, Photosensitivity, and Poling in Glass Waveguides, Barcelona/Spain, 27-31, 2014.

R. E. Silva, A. Hartung, M. Rothhardt, A. A. P. Pohl and H. Bartelt "Acousto-optic modulation of a fiber Bragg grating in four holes suspended-core fiber", in 16^o SBMO - Simpósio Brasileiro de Micro-ondas e Optoeletrônica, Curitiba/Brazil, 2014.

R. E. Silva, A. Hartung, M. Rothhardt, A. A. P. Pohl and H. Bartelt, "Simulation of acousto-optical modulation of fiber Bragg gratings in suspended-core fibers", in Workshop on Specialty Optical Fibers and their Applications, Sigtuna/Sweden, 2013.

R. E. Silva, M. A. R. Franco, H. Bartelt, and A. A. P. Pohl, "Numerical characterization of an acousto-optic ring sensor for measuring d-glucose concentrations", in Workshop on Specialty Optical Fibers and their Applications, Sigtuna/Sweden, 2013.

R. E. Silva, A. Hartung, M. Rothhardt, A. A. P. Pohl, and H. Bartelt, "Effect of the silica bridge thickness of suspended-core fiber on the acousto-optic modulation of fiber Bragg gratings", in Doctoral Students Conference on Optics, Suhl/Germany, 2013.

R. E. Silva, A. Hartung, M. Rothhardt, A. A. P. Pohl, and H. Bartelt. "Suspended-core size effect in interaction of longitudinal acoustic waves and fiber Bragg gratings", in SBMO/IEEE MTTT International Microwave and Optoelectronics Conference (IMOC), Rio de Janeiro/Brazil, 1-3, 2013.

A. A. P. Pohl, R. E. Silva, M. A. R. Franco, P. T. Neves, H. Bartelt "Modelling the bandwidth behavior of fibre Bragg grating excited by low-frequency acoustic waves" in 15th International Conference on Transparent Optical Networks, Cartagena/Spain, 1-4, 2013.

R. E. Silva and A. A. P. Pohl, "Characterization of longitudinal acoustical waves in a fiber using an extrinsic Fabry-Perot interferometer", in 22nd International Conference on Optical Fiber Sensor, Beijing/China, 84212T-1-84212T-4, 2012.

R. E. Silva and A. A. P. Pohl, "Characterization of flexural and longitudinal acoustic waves in standard and photonic crystal fibres", in 14th International Conference on Transparent Optical Networks, Coventry/England, 1-4, 2012.

R. E. Silva, M. A. R. Franco and A. A. P. Pohl "Controle dinâmico do espectro de dispersão de fibra microestruturada usando ondas acústicas" in 15º Simpósio Brasileiro de Micro-Ondas e Optoeletrônica e 10º Congresso Brasileiro de Eletromagnetismo, São Caetano do Sul/Brazil, 1-4, 2012.

ACKNOWLEDGEMENTS

I would like to thank all the people that directly or indirectly contributed for the realization of this important stage of the my life, in special to,

Prof. Hartmut Bartelt and Prof. Alexandre Pohl for the exceptional efforts, advises and friendly attention to help and support me at all times during my studies, as well, for the amazing opportunity to study and work in Germany.

My colleagues of the Leibniz Institute of Photonic Technology (IPHT), in particular, to Tobias Tiess, Martin Becker, Tina Eschrich, Tino Elsmann, Adrian Lorenz and Alexander Hartung and the Heads of the Passive and Active Fiber Optic Groups, Manfred Rothhardt and Matthias Jäger, for the discussions, material, lab assistance and facilities, which helped me to overcome the research and technological challenges to perform this work. Also, to Katrin Wondraczek, Jörg Bierlich, Jens Kobelke and Kay Schuster of the Optical Fiber Technology Group, for the fabrication and support with the suspended core fibers.

Prof. Marcos Ruggieri Franco of the Institute of Advanced Studies – IEAv/CTA and Prof. Paulo de Tarso Nevers Junior of the UTFPR-Toledo, for the friendly discussions, support and contributions for the simulations.

Prof. Ricardo Lüders, Prof. Fábio Schneider, Prof. Hypolito Kalinowski and Prof. Marcia Muller of the UTFPR-Curitiba, for the support in the scholarship process.

UTFPR/CPGEI and FSU for the infrastructure and academic-scientific qualification. All other professors, friends and colleagues of the Photonic Group at the UTFPR for further contributions.

Coordenação de Aperfeiçoamento de Pessoal de Nível Superior – CAPES and the German Academic Exchange Service (DAAD), for the financial support to this project.

My parents and close friends for the dedication and unconditional support at all times.

Ehrenwörtliche Erklärung

Ich erkläre hiermit ehrenwörtlich, dass ich die vorliegende Arbeit selbständig, ohne unzulässige Hilfe Dritter und ohne Benutzung anderer als der angegebenen Hilfsmittel und Literatur angefertigt habe. Die aus anderen Quellen direkt oder indirekt übernommenen Daten und Konzepte sind unter Angabe der Quelle gekennzeichnet.

Bei der Auswahl und Auswertung folgenden Materials haben mir die nachstehend aufgeführten Personen in der jeweils beschriebenen Weise entgeltlich/unentgeltlich geholfen:

1. Dr. Martin Becker: Herstellung von Faser-Bragg-Gittern
2. Tina Eschrich: Herstellung von getaperten Fasern
3. Tobias Tiess: Laseraufbau
4. Prof. Dr. Paulo de Tarso Neves Junior: Bereitstellung eines TMM-Algorithmus für die FBG simulation.
5. Die Koautoren der entsprechenden Publikationen mit Diskussionen und Ratschlägen

Weitere Personen waren an der inhaltlich-materiellen Erstellung der vorliegenden Arbeit nicht beteiligt. Insbesondere habe ich hierfür nicht die entgeltliche Hilfe von Vermittlungs- bzw. Beratungsdiensten (Promotionsberater oder andere Personen) in Anspruch genommen. Niemand hat von mir unmittelbar oder mittelbar geldwerte Leistungen für Arbeiten erhalten, die im Zusammenhang mit dem Inhalt der vorgelegten Dissertation stehen.

Die Arbeit wurde bisher weder im In- noch im Ausland in gleicher oder ähnlicher Form einer anderen Prüfungsbehörde vorgelegt.

Die geltende Promotionsordnung der Physikalisch-Astronomischen Fakultät ist mir bekannt.

Ich versichere ehrenwörtlich, dass ich nach bestem Wissen and Gewissen die reine Wahrheit gesagt und nichts verschwiegen habe.

Jena, 20. Juli 2015

Ricardo Ezequiel da Silva

Lebenslauf (Curriculum)

Da Silva, Ricardo Ezequiel

Born in: 30. Mai 1981 in Francisco Beltrão (Brazil)

1988 - 1995 Primary school, Escola Estadual da Cango, Francisco Beltrão, Brazil

1996 - 1999 Technician in Accounting (High school)
Colégio Estadual Mario de Andrade, Francisco Beltrão, Brazil

2006 - 2007 Technician in Electromechanics, (Professional post high school)
Centro Estadual de Educação Pedro Boaretto Neto, Cascavel, Brazil

2005 - 2009 Bachelor in Telecommunications Engineering (Eng.)
Faculdade Assis Gurgacz, Cascavel, Brazil

2010 - 2011 Master in Sciences in Electrical Engineering (M.Sc.)
Federal University of Technology - Paraná, Curitiba, Brazil

Since 2011 Doctorate in Sciences in Electrical Engineering / Technical Physics
Federal University of Technology - Paraná, Curitiba, Brazil
Friedrich-Schiller-Universität – Jena, Germany

Jena, 20. Juli 2015

Ricardo Ezequiel da Silva